UNIVERSITAT POLITÈCNICA DE VALÈNCIA

School of Aerospace Engineering and Industrial Design

LES modelling of the simplex atomization of Sustainable Aviation Fuels (SAF) through a VOF method

Master's Thesis

Master's Degree in Computational Fluid Dynamics

AUTHOR: Paredes, Joaquín

Tutor: Carreres Talens, Marcos

ACADEMIC YEAR: 2023/2024

UNIVERSITAT POLITÈCNICA DE VALÈNCIA

ETSI Aeroespacial y Diseño Industrial

UNIVERSITAT POLITÈCNICA DE VALÈNCIA

ESCUELA TÉCNICA SUPERIOR DE INGENIERÍA AEROESPACIAL Y DISEÑO INDUSTRIAL

CLEAN MOBILITY AND THERMOFLUIDS INSTITUTE

LES MODELLING OF THE SIMPLEX ATOMIZATION OF SUSTAINABLE AVIATION FUELS (SAF) THROUGH A VOF METHOD

Author: Joaquin Andres Paredes Coronel
Tutor: Marcos Carreres Talens

Máster Universitario en Mecánica de Fluidos Computacional

Valencia, June 2024

Contents

List of Figures

List of Tables

Resumen

En este trabajo se estudia, mediante dinámica de fluidos computacional, el flujo interno dentro de un atomizador tipo pressure swirl, así como el flujo bifásico (líquido − gas) de su atomización primaria para distintos combustibles, entre los cuales se encuentra un combustible sostenible de aviación (SAF). El modelo computacional simula el flujo interno desde los puertos tangenciales de la zona de flujo externo en la que se captura la atomización.

Se utilizan leyes de conservación para flujo bifásico: el modelo de mezcla con enfoque VOF junto con un esquema de reconstrucción de interfaz: IsoAdvector. La turbulencia del flujo se modela mediante los enfoques: URANS en la fase de inicialización y LES para el flujo atomizado en estado estable. Se implementa una estrategia de mallado dinámico tipo AMR, la cual refina la malla en la interfaz para mejorar la captura de la misma.

Para determinar la mejor configuración de la malla, se realizan simulaciones comparativas con distintos valores de los parámetros de mallado y se escoge la mejor combinación de los mismos en cuanto a eficiencia de coste computacional y calidad de los resultados.

Con la estrategia de mallado óptima, se realizan cuatro simulaciones distintas, cada una de las cuales simula un combustible diferente: n-heptano a temperatura ambiente, n-heptano precalentado, queroseno convencional y el combustible SAF de la familia HEFA-SPK. Cada simulación se distingue de las demás por las propiedades físicas del combustible respectivo: densidad, viscosidad y tensión superficial. La fase gaseosa, aire atmosférico inicialmente en reposo a temperatura ambiente, se mantiene sin cambios para las cuatro simulaciones.

Se describe cualitativamente la formación del flujo atomizado en forma de cono hueco y la disgregación del líquido en ligamentos y gotas de cada combustible. Además, se cuantifican las dimensiones del núcleo de aire característico de este tipo de atomizadores y el espesor de la película de combustible a lo largo de la dirección axial de inyección.

Para cuantificar la calidad de la atomización de cada combustible, se realiza un estudio estadístico de la nube de gotas capturada durante la fase estable de la simulación y se comparan los tamaños, la distribución espacial y las velocidades de ligamentos y gotas formadas a partir de cada combustible. Se compara especialmente la calidad y las características de la nube de gotas que se forma a partir del combustible SAF con respecto al queroseno convencional.

Palabras clave: atomización pressure swirl, SAF, Volume of Fluid, LES.

Abstract

In this work, the internal flow within a pressure swirl atomizer is studied using computational fluid dynamics, as well as the biphasic (liquid − gas) flow of its primary atomization for different fuels, among which is a sustainable aviation fuel (SAF). The computational model simulates the internal flow from the tangential inlet ports to an external flow zone that captures the atomization.

Conservation laws for biphasic flow are used: the mixture model with a VOF approach, along with an interface reconstruction scheme: IsoAdvector. The turbulence of the flow is modeled using URANS during the initialization stage and LES for the atomized flow in the stabilized stage. A dynamic meshing strategy, AMR, is implemented to refine the mesh at the interface to improve its capture.

To determine the best mesh configuration, comparative simulations are performed with different values of the meshing parameters, and the best combination is chosen based on computational cost efficiency and result quality.

With the optimal meshing strategy, four different simulations are conducted, each simulating a different fuel: n-heptane at ambient temperature, preheated n-heptane, conventional kerosene, and a SAF from the HEFA-SPK family. Each simulation is distinguished from the others by the physical properties of the respective fuel: density, viscosity, and surface tension. The gaseous phase, atmospheric air initially at rest at ambient temperature, remains unchanged for the four simulations.

The formation of the atomized flow in the form of a hollow cone and the disintegration of the liquid into ligaments and droplets for each fuel is described qualitatively. Additionally, the dimensions of the air core characteristic of this type of atomizer and the thickness of the fuel film along the axial direction of injection are quantified.

To quantify the quality of the atomization for each fuel, a statistical study of the droplet cloud captured during the steady phase of the simulation is conducted, comparing the sizes, spatial distribution, and velocities of the ligaments and droplets formed from each fuel. The quality and characteristics of the droplet cloud formed from SAF are especially compared with conventional kerosene.

Keywords: pressure swirl atomization, SAF, Volume of Fluid, LES.

Resum

En aquest treball s'estudia, mitjançant dinàmica de fluids computacional, el flux intern dins d'un atomitzador tipus *pressure swirl*, així com el flux bifàsic (líquid − gas) de la seua atomització primària per a diferents combustibles, entre els quals es troba un combustible sostenible d'aviació (SAF). El model computacional simula el flux intern des dels ports tangentals de la zona de flux extern en la qual es captura l'atomització.

S'utilitzen lleis de conservació per a flux bifàsic: el model de mescla amb enfocament VOF junt amb un esquema de reconstrucció d'interfície: IsoAdvector. La turbulència del flux es modela mitjançant els enfocaments: URANS en la fase d'inicialització i LES per al flux atomitzat en estat estable. S'implementa una estratègia de mallat dinàmic tipus AMR, la qual refina la malla en la interfície per a millorar la captura d'aquesta.

Per a determinar la millor configuració de la malla, es realitzen simulacions comparatives amb diferents valors dels paràmetres de mallat i es tria la millor combinació d'aquests quant a eficiència de cost computacional i qualitat dels resultats.

Amb l'estratègia de mallat òptima, es realitzen quatre simulacions diferents, cadascuna de les quals simula un combustible diferent: n-heptà a temperatura ambient, n-heptà precalentat, querosè convencional i el combustible SAF de la família HEFA-SPK. Cada simulació es distingeix de les altres per les propietats físiques del combustible respectiu: densitat, viscositat i tensió superficial. La fase gasosa, aire atmosfèric inicialment en repòs a temperatura ambient, es manté sense canvis per a les quatre simulacions.

Es descriu qualitativament la formació del flux atomitzat en forma de con buit i la disgregació del líquid en lligaments i gotes de cada combustible. A més, es quantifiquen les dimensions del nucli d'aire característic d'aquest tipus d'atomitzadors i el gruix de la pel·lícula de combustible al llarg de la direcció axial d'injecció.

Per a quantificar la qualitat de l'atomització de cada combustible, es realitza un estudi estadístic del núvol de gotes capturat durant la fase estable de la simulació i es comparen les mides, la distribució espacial i les velocitats de lligaments i gotes formades a partir de cada combustible. Es compara especialment la qualitat i les característiques del núvol de gotes que es forma a partir del combustible SAF respecte al querosè convencional.

Paraules clau: *atomització*, *pressure swirl*, SAF, *Volume of Fluid*, LES.

Acknowledgements

First and foremost, I thank God for giving me life, the opportunity, and everything necessary to train and work.

I am grateful to Marcos for his guidance and teaching, and for his honorable and integral work as a tutor and professor. His dedication and support have been fundamental in this process. To Alicia, I thank you for your teaching and your help with all the doubts that arose.

To all the professors, thank you for your dedication to the master's program, for your teaching, and for your constant effort to motivate learning. Your commitment has been an inspiration.

To my parents, I am deeply grateful because they never cease to dedicate their entire lives to their children and their preparation, for their love and their example. It is thanks to their dedication and sacrifice that I have been able to move forward.

To my family and friends, I thank you for your unconditional support, for motivating me to keep going. You have made this stage more enjoyable and pleasant with your company and affection.

To a very special friend, I thank you because providentially I have received from you the light and the strength I had always longed for. You have given me a motive and a sense that fulfills and gives coherence to everything I live, pushing me to strive with joy and peace.

Part I

Memory

Chapter 1

Introduction

1.1 Motivation

The substitution of fossil fuels with alternative energy sources is gaining momentum and is being developed with a view to reducing environmental impact. Evidence of this can be seen in all the alternative and sustainable energy sources that are being researched and implemented in industry, power generation, and transportation, which aim to have very low or zero harmful emissions for the environment. In fact, it is estimated that by 2022, 23% of the energy consumed in the European Union will come from renewable sources [1]. Now, to directly reduce greenhouse gas emissions, it is necessary to prioritize and work on the sectors that generate the most emissions. The sector with the greatest contribution to global greenhouse gas (GHG) emissions is transportation; in Spain, it was estimated that in 2021, this sector generated 29.6% of total GHG emissions [2], with CO_2 accounting for 79.7% of total GHG emissions, followed by methane (14.4%). This issue is being addressed through science and technology driven by agreements such as the decarbonization strategy proposed by the European Union, which includes, among its most relevant lines of work, the transition to renewable fuels, especially in heavy road freight transport, aviation, and shipping [3].

Due to the significant impact of the transportation and mobility sector and with the aim of making it more sustainable, manufacturers are exploring alternatives such as electric vehicles and hybrid engines. Nevertheless, compared to automobiles, airplanes require energy sources with significantly higher energy density to maintain the necessary performance during long flights. This is why high-energy-density liquid fuels are used in this sector. These fuels are ideal for a wide range of applications as they are a compact energy source and are easy to store, transport, and distribute. Additionally, there is currently a well-established global infrastructure for the production, distribution, sale, and use of liquid fuels in the maritime, terrestrial, and aviation transport sectors. Therefore, sustainable liquid fuels (that are not derived from crude oil) present the best alternative to meet this demand for sustainable mobility.

Currently, the aviation sector is increasingly utilizing sustainable fuels known as SAFs (Sustainable Aviation Fuels), produced from sustainable biomass, which could potentially reduce carbon emissions by up to 80% compared to traditional fossil fuels. These fuels can be derived from various feedstocks, including oils, greasy residues, municipal solid waste, agricultural and forestry residues, wet waste, as well as non-food crops grown on marginal lands. It is also feasible to produce them synthetically through a process that captures carbon directly from the air. Several authors agree that an SAF fuel is considered '*sustainable*' as long as its feedstocks do not compete with food crops or their production, thereby avoiding incremental use of resources such as water or deforestation of land [4]. Under these conditions, these fuels do not pose environmental challenges such as deforestation, soil productivity loss, or biodiversity reduction. Unlike fossil fuels, SAFs recycle the CO_2 absorbed by the biomass used in the feedstock during its lifecycle.

In 2008, Virgin Atlantic conducted the first test flight using biofuel, marking a milestone in the exploration of sustainable alternatives for aviation. Subsequently, between 2011 and 2015, twenty-two airlines completed over 2500 commercial passenger flights using blends of up to 50% biofuel sourced from materials such as used cooking oil, jatropha, camelina, and algae. Other airlines have become increasingly involved in the use of these fuels to the point where, by 2022, SAF production tripled, reaching 300 million liters, compared to the 100 million liters recorded in 2021 [4].

1.2 Justification

These sustainable fuels are gaining popularity and are being used on a larger scale. Although they are very similar to traditional liquid fuels, they have different values in their physical properties that affect the flow through atomizers and hence the entire subsequent combustion process that takes place in the engine. Therefore, studying the spray formation process of fuels with physical properties different from those of conventional fuels becomes important because fluid properties, mainly viscosity and surface tension, are strongly linked to atomization behavior. Studying this atomization process allows for understanding fuel efficiency and responsible fuel use. In fact, as mentioned in [5], unexpected increases in viscosity and surface tension will limit droplet breakup, resulting in larger average droplet sizes, thus increasing residence time and NO_x formation. These gases can be harmful to the environment and can have implications in terms of environmental regulations, as NO reacts with O_2 in the atmosphere to form NO_2, which is a major contributor to acid rain. Additionally, nitrogen oxides (NO_x) participate in the formation of photochemical oxidants (smog). On the other hand, if fuel properties result in very large droplets, this can lead to incomplete combustion or also result in the emission of unwanted combustion products such as carbon monoxide (CO) and unburned hydrocarbons. Furthermore, inefficient atomization can lead to higher fuel consumption, as the engine may require more fuel to achieve the desired power due to poor fuel and air mixing.

Currently, SAFs are used in jet turbine engines mixed with traditional fossil fuels (kerosene) in various proportions, with the maximum blend reaching up to 50%. Subsequently, depending on the type of SAF, blends of 20 or 10% can be found. This study does not focus on the atomization of a blend of SAFs with traditional fuel, but rather on the atomization of 100% SAF fuel. This implies that it would be beneficial to study and demonstrate that the physical and chemical processes that take place in an aeronautical engine operate correctly when using this 100% fuel. Thus, engines would not be restricted by current regulations that require it to be used in a blend of up to 50%.

The SAFs used in this study belong to the HEFA-SPK family. This type of SAF has been approved by the American Society for Testing and Materials (ASTM) for inclusion in ASTM standard D7566 since June 2011. In the production of SAFs from the HEFA family, lipid raw materials such as vegetable oils or algae oils, animal fats or waste fats such as cooking oils, are deoxygenated and then hydroprocessed to produce a pure hydrocarbon fuel blend component.

Generally, as concluded in [6], these biofuels have already been proven to perform well in terms of combustion. Therefore, studying their properties and performance in terms of atomization is a beneficial investigation that can enhance their efficiency and performance, thereby promoting their increased use and emissions reduction in the aviation sector.

In this work, computational numerical models are employed to numerically solve the equations governing the two-phase fluid dynamics of fuel injection. To date, numerous research studies have been conducted using computational numerical models of atomization in almost all types of atomizers, encompassing both primary and secondary atomization, evaporation, and reactive combustion flow. There exists a wealth of literature and validated studies that provide a solid theoretical foundation for the proper use of these numerical models to simulate and study atomization. Moreover, not only is the literature abundant, but models are continuously being improved and optimized, allowing for the implementation of highly detailed models of such flows. This, coupled with the increasing computational power available each day, gives numerical study of atomization a significant and validatable scope, leading to substantial economic savings compared to conducting a series of experimental simulations using a burner test bench. It is important to note that the atomization and combustion process in an aeronautical engine is a complex problem that cannot be fully studied using a single model employing high-fidelity tools. Therefore, this study represents a preliminary step in the analysis of this intricate phenomenon: primary atomization occurring upstream of combustion.

1.3 Previous Work and Objectives

At the research center, CMT-Clean Mobility and Thermofluids Research Institute at the Universitat Politècnica de València, the Injection group tackles various research fields including fuel and biofuel properties, injection systems, atomizer technologies, among others. To conduct these experimental investigations, the Injection team has access to laboratories and high-tech equipment at the CMT institute. These facilities offer wide ranges of operability in terms of pressures, flow rates, and temperatures, enabling experimental studies ranging from motorcycle engine injection to industrial injection and atomization processes [7]. Simultaneously with experimental studies, computational numerical modeling is conducted using both 1D models and Computational Fluid Dynamics (CFD) 3D models such as RANS, LES, and DNS, simulating and studying internal and external flow, cavitation, among other phenomena associated with fuel injection. For this computational modeling, a cluster with around 1500 processors is available for parallel computing.

The present Master's Thesis is part of the project 'Modeling Sustainable Aviation Fuel for Low Emissions: Atomization' (SAFLOW-BREAK), funded by public funds from the State Research Agency (AEI). This project, coordinated with the Barcelona Supercomputing Center (BSC), aims to evaluate through experimental and computational means the influence of using 100% SAF liquid fuels on atomization, evaporation, mixing, and combustion processes.

As mentioned earlier, this project is a broad and complex case study. In this regard, this Master's thesis takes one of the first steps with the computational numerical study of the primary atomization of this fuel. It builds upon the Master's thesis of [8]. In the latter, it was constructed in OpenFOAM a computational LES (Large Eddy Simulations) model of the two-phase flow with the VOF (Volume of Fluid) approach for internal flow and primary atomization of n-heptane in a simplex atomizer. Both the mesh topology and the interface reconstruction scheme that best capture the fuel breakup into droplets were determined.

Therefore, the computational model developed in [8] serves as the starting point for the study in this master's thesis, as it uses the same geometry for the spatial domain but extends the domain in the axial flow direction to capture the droplet formation in greater detail. The same meshing method and interface reconstruction scheme as in [8] are used, but with an optimized mesh. This means a coarse base size is used, with local refinement in areas where the flow develops at small scales, and adaptive mesh refinement (AMR) techniques are employed for a better description of the liquid-gas interface. This approach efficiently refines the mesh at each simulation step exclusively in the regions where the flow requires it. This meshing method reduces computational cost primarily by significantly decreasing the number of cells compared to meshes previously used in these simulations.

This master's thesis employs meshing methods, interface reconstruction, and physical and numerical models to conduct a parametric study of four fuels: n-heptane, conventional kerosene, HEFA-SPK type SAF at ambient temperature, and high-temperature n-heptane. These fuels differ in their physical properties (viscosity and surface tension), and the study investigates the spray development through the measurement of characteristic spray lengths and primary atomization via the statistical analysis of the properties of the generated droplets (size and velocities).

Chapter 2

Theoretical Fundamentals of Atomization

2.1 Atomization

Atomization in general terms can be defined as the transformation of a continuous flow of a liquid into a dispersed flow in the form of a cloud of droplets. This process can occur naturally in everyday situations, but it is primarily implemented in a controlled manner in numerous engineering applications when there is a need to increase the specific surface area of the atomized liquid.

It is important to recognize that, although in engineering the aim is to control the atomization process, the forces and deformations of the liquid occurring in any atomization process happen over very wide ranges of amplitudes and frequencies, most of which are not controlled by the atomization systems. This is why atomization is said to be a naturally stochastic process, from which clouds of droplets with random droplet sizes and number are produced. Figure 2.1 shows a spray and many of the forces and oscillations generated in this process, which must be studied, characterized, and correlated to achieve useful and efficient control in atomization.

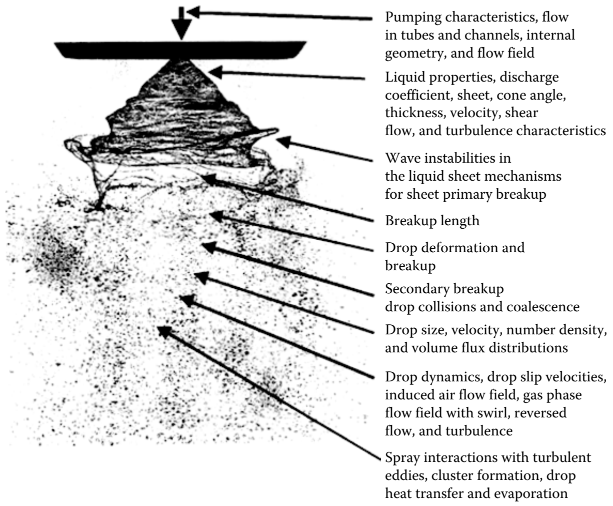

Figure 2.1: Simple spray illustrating many atomization features that need to be characterized [9].

Liquid atomization is a process with several decades of study and development, which continues to be researched, improved, and developed in many branches of industry and engineering today, allowing for increased efficiency in atomization processes. For example, atomization systems are used in spray combustion in furnaces, gas turbines, engines, and rockets, spray drying and cooling, air conditioning, industrial cleaning, crop spraying, powder metallurgy, spray painting and coating, fire protection, humidification, inhalation therapy, food preservation and cleaning, water treatment, and many other areas [10]. Each of these applications involves the design of a unique and specific atomization system, which often includes an atomization nozzle or atomizer. Figure 2.2 shows, as an example, an atomization system for sterilization and disinfection, which can use different nozzles, each providing different shapes, lengths, and average droplet sizes depending on the specific application required.

Figure 2.2: Desinfection atomization system. Tomado de [11]

2.2 Atomizers

An atomizer is the device that encounters the continuous flow of liquid just before being expelled into a gaseous atmosphere. It is primarily through this device that the flow transitions from continuous to dispersed in the form of a cloud of droplets. Generally, atomization systems use a pumping system to deliver pressure energy to the continuous flow of liquid. This pressure energy, in addition to forcing the liquid through the nozzle, also transforms into kinetic energy of the flow when it is expelled at high speed. This flow with high kinetic energy, upon encountering the gaseous atmosphere, disintegrates into ligaments and droplets. Other atomizers, besides the pumping system, have movable mechanical elements such as rotating disks or nozzles to break and disperse the continuous flow; others use airflows to accelerate the disintegration of the liquid. Moreover, recently, novel techniques in fuel atomization in gas turbines are being developed, such as plasma-assisted sprays, ultrasound, or supercritical fluids [5].

Lefebvre, in [9], provides a concise summary of the different types of atomizers that commonly use a pumping system to generate the cloud of droplets, categorizing them into three main categories: pressure atomizers, rotary atomizers, and twin fluid atomizers.

2.2.1 Pressure atomizers

In these atomizers, pressure energy is transformed into kinetic energy by expelling a liquid through a very small aperture under high pressure. The pressure drop due to the reduction in the cross-sectional area of the flow is the only form of energy that the liquid receives to disperse into droplets. They are mainly used in fuel injection. Their operating pressure ranges in a typical hydrocarbon fuel are as follows: a pressure drop of 138 kPa (20 psi) at the nozzle generates an outlet velocity of 18.6 m/s. This velocity increases proportionally to the square root of the applied pressure: so at 689 kPa (100 psi), the velocity reaches 41.5 m/s, while at 5.5 MPa (800 psi), the velocity increases to 117 m/s. Within this category, we can find different atomizers which differ only in the shape and number of conduits that carry the fluid to the outlet orifice. In this category is the pressure swirl atomizer (see Figure 2.3), also known as simplex, involved in this study.

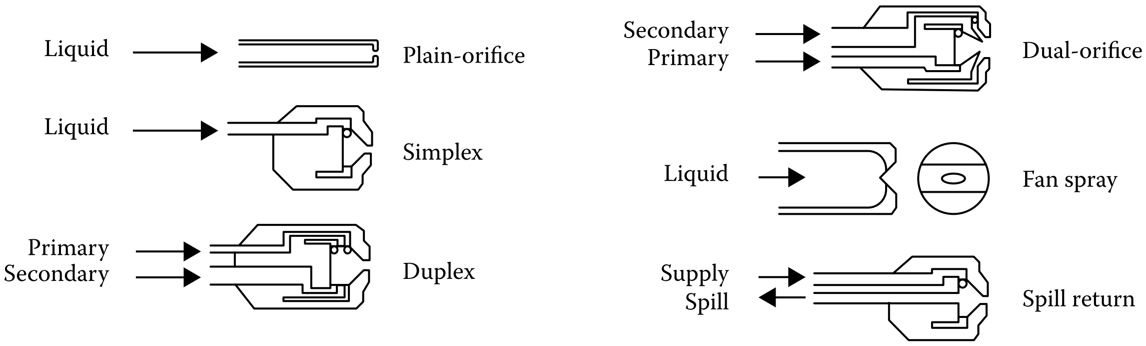

Figure 2.3: Pressure atomizers types. Adapted from [9].

2.2.2 Rotary atomizers

The rotary atomizers 2.4 are also widely used devices that feature rotating components upon which a stream of liquid impacts. In this way, the angular momentum of the rotating body is transferred to the liquid due to adhesive forces and the viscosity of the liquid. This liquid, which absorbs angular momentum, enters into a rotational flow and is dispersed at high speed from the edge of the rotating component. Here, in addition to the total pressure energy of the flow, the energy of the rotating component against which the stream impacts is used, and it disintegrates into droplets. These rotating components, which can be disks or cups, may have vanes or slots on their edge, thus allowing the formation of uniform sprays with independent variation of flow rate and rotation speed. They are especially useful for generating 360° spray patterns and can be adapted for a variety of applications due to their operational flexibility.

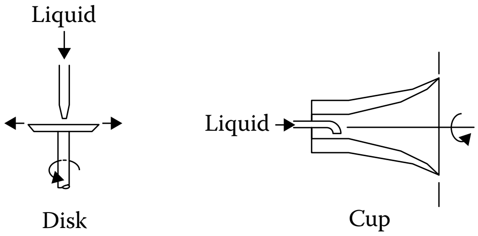

Figure 2.4: Rotary atomizers types. Adapted from [9].

2.2.3 Twin fluid atomizers

In this category, there are two types of atomizers 2.5:

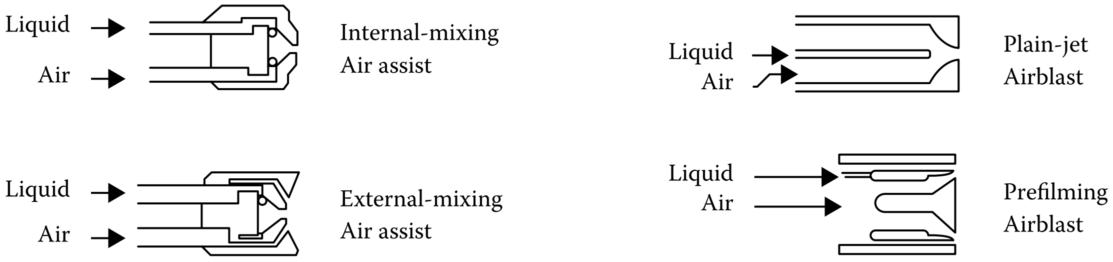

(a) (b)

Figure 2.5: Twin fluid atomizers types (a) Air-assisted atomizers (b) Airblast atomizers. Adapted from [9].

Air-Assist Atomizers

These atomizers use a high-speed jet of air or vapor (at sonic velocities) to mix and disperse the liquid. They can have internal or external mixing configurations. Although they may be less energy-efficient, they are capable of producing finer spray than standard pressure nozzles. They are useful for atomizing high-viscosity liquids and offer flexibility in varying the spray angle.

Airblast Atomizers

These devices are similar to Air-Assist Atomizers. The main difference lies in that air-blast atomizers employ large quantities of air at lower speeds, ideal for atomizing liquid fuels in continuous-flow combustion systems such as gas turbines. Their common design includes dispersing the liquid into a thin conical sheet, subsequently exposed to high-speed air streams for efficient atomization.

2.3 Basic process on atomization

When studying the causes and forces involved in atomization, it is recognized that the breakup of a liquid jet into droplets is due to the action of internal flow forces and external forces acting on the liquid flow that oppose the viscous resistance of the liquid and surface tension. These forces, which become unbalanced, give rise to pressure gradients and thus deformations in the flow, which behave as oscillations that propagate and amplify. The main internal force that causes deformations in the jet, before any external force, is the impulse of the radial velocity components of the turbulent flow expelled through a nozzle, as these velocity components, which have a different direction from the main direction in which the liquid is expelled and which cease to be confined by the walls of the nozzle, cause oscillations to begin on the free surface of the jet, which are amplified and cause the jet to disintegrate.

Before describing how external forces influence atomization, it is worth briefly mentioning the mode of liquid droplet formation in its simplest form: static drop formation. Lefebvre [9] explains how a continuous and quasi-static flow of liquid can break into droplets under the action of a single constant external force: the weight of the liquid due to gravity. This inertia of the

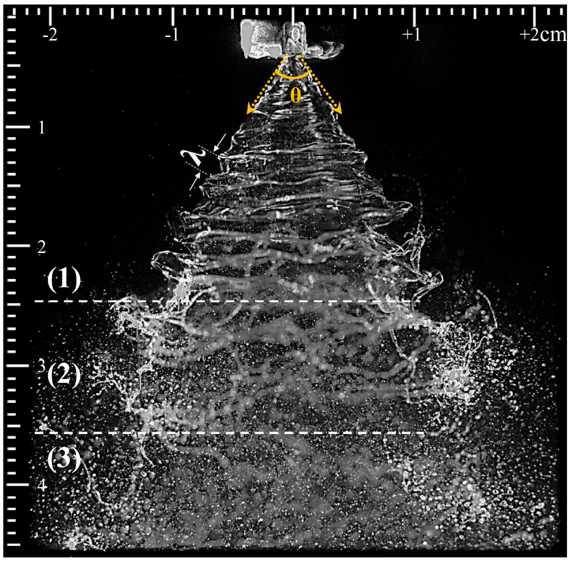

Figure 2.6: Aatomization regions: (1) Primary atomization, (2) Ligaments breakup, (3) Secondary atomization [12].

liquid due to gravity overcomes the two main forces that a liquid offers as resistance to forming droplets: viscous forces and surface tension of the liquid. The equation $D = (6d_\mathrm{o}\sigma)/(\rho_\mathrm{L}g)^{1/3}$ determines the diameter of the liquid droplet with density ρ and coefficient of surface tension σ, formed from static drop formation through a circular orifice in a horizontal plane of diameter d_o. This equation predicts droplet sizes of 3.6 mm for water and 2.6 mm for kerosene when $d_\mathrm{o} = 1$ mm, which are excessively large compared to the droplet sizes sought in any engineering atomization process. This shows that a very slow flow that does not interact with air resistance forces and does not become turbulent, although it manages to overcome surface tension and viscosity, only produces droplets of very large sizes with little or no practical utility in the context of atomization.

In Figure 2.6, the atomization regions in a simplex spray are shown. The different roles played by liquid turbulence and air friction allow distinguishing between **primary atomization** and **secondary atomization**. Primary atomization is related to the fragmentation of the jet by the action of internal forces, such as turbulence in the liquid flow, inertial effects, or those arising from the relaxation of velocity profile and surface tension. Secondary atomization always involves the action of aerodynamic forces in addition to those present in primary atomization. Aerodynamic forces promote atomization by acting directly on the jet surface and by dividing the droplets formed in primary atomization into smaller droplets.

2.3.1 Disintegration of a liquid jet

As mentioned at the beginning of this section, the disintegration of a liquid jet into ligaments and droplets is initiated due to disturbances on the free surface of the jet that can occur without the need for the effects of external aerodynamic forces, but at the same time, thanks to these forces, they are formed and amplified much faster.

A disturbance can be any fluctuation in pressure or velocity on the surface of the jet due to fluctuations of external aerodynamic forces, which generate oscillations that can become unstable and continuously amplify. Lefebvre in [9] summarizes how each atomization regime can be associated with a type of disturbance with its respective wave number. In Figure 2.7, the distinct regimes of atomization of a flat jet can be identified, which have been studied and characterized by different authors and theories. Ohnesorge's theory includes three atomization regimes for a plain orifice atomizer jet. Each of these regimes is reached as two dimensionless numbers are simultaneously increased: the Reynolds number of the liquid flow: $\mathrm{Re\,L} = (\rho \mathrm{L} U d_\mathrm{o}/\mu_\mathrm{L})$ and the Ohnesorge number: $\mathrm{Oh} = \left(\mu_\mathrm{L}/\sqrt{\rho_\mathrm{L}\sigma d_\mathrm{o}}\right)$. As the order of both numbers increases, the Rayleigh regime is first passed through, in which $\mathrm{Re\,L}$ is so low that the surrounding air flow does not influence the deformation of the jet, but only dilational deformations are considered that amplify along the length of the jet and lead to varicose breakup. In the figure, it can be seen that as $\mathrm{Re\,L}$ and Oh increase, the Sinous wave breakup regime is reached, in which the jet departs from its longitudinal axis by oscillating as sinusoidal waves due to air friction. Finally, complete atomization is reached in which, due to the high $\mathrm{Re_L}$ of the flow and the air resistance forces, the jet disintegrates into droplets as soon as it exits the nozzle.

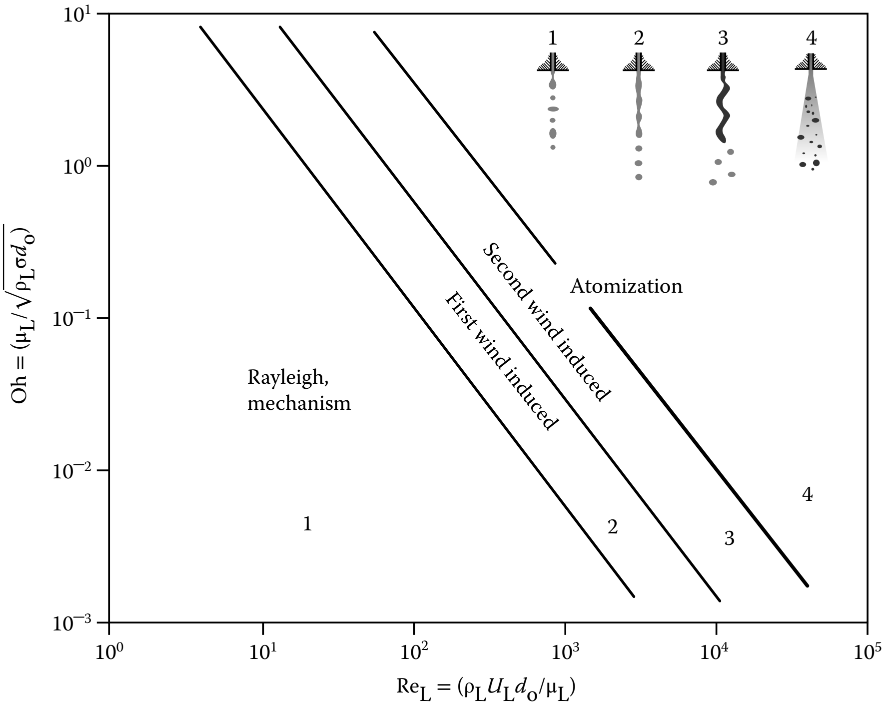

Figure 2.7: Evolution of the jet desintegration regimes [9].

The study of the disintegration of liquid jets has led to the conclusion that a jet expelled in laminar flow can maintain itself as laminar flow near the outlet orifice as long as the Reynolds number remains below a critical Reynolds number. Conversely, a jet expelled in turbulent flow remains turbulent as long as the Reynolds number stays above the critical value. However, as the jet moves away from the outlet orifice, whether in laminar or turbulent flow, the combined effect of air resistance and surface tension increases, leading to more irregularities on the surface of the jet, which ultimately cause the jet to disintegrate.

2.3.2 Liquid sheet desintegration

There are some types of atomization in which the liquid is forced to take the form of a thin film, which breaks more easily into ligaments and droplets than a cylindrical jet. There are mainly two types: flat films or conical liquid sheets. Flat films are obtained through impingement jet atomization, which involves the collision of two cylindrical jets, while conical films are formed when the liquid is expelled through an annular orifice or is forced to have an annular flow in the nozzle duct before being expelled (the latter case occurs in the simplex atomizers studied here). In all cases, since a liquid film significantly increases the surface area of the initial flow, the main force that must be overcome to maintain the flow in this form is surface tension force, as it tends to contract the surface area of the liquid. Also in all cases, the initial velocity of the flow at the start of the film is the source of momentum that keeps the flow in film form. The magnitude of this initial velocity proportionally affects the length the film reaches before breaking. The point at which the inertial forces of the film flow and the surface tension forces balance is the point where the film becomes unstable and begins to break. This point is known as the leading edge.

In the case of liquid sheets, different types of deformations occur, each associated with a type of oscillation that eventually destabilizes and disintegrates the jet. There is a vast body of literature regarding the different breakup modes of fuel films and how the maximum length and breakup are influenced by the physical properties of the surrounding gaseous medium.

2.3.3 Droplets break up

The nature of the aerodynamic flow around droplets is the reason why droplets either break in a certain way or remain unbroken. Lefebvre [9] distinguishes how droplet breakup is affected by three types of flows: stable, turbulent, and viscous. In stable flow, non-accelerated flow is distinguished from accelerated flow. In the former, the magnitude of the aerodynamic drag force must equal the magnitude of the surface tension force to reach the initial breakup condition, and it is said that the Weber number, $\rho_{\mathrm{A}} U_{\mathrm{R}}^2 D/\sigma$, reaches its critical value: Wecrit $= \frac{8}{C_{\mathrm{D}}}$, which is in turn given by a critical flow velocity $U\mathrm{R}_{\mathrm{crit}}$. In accelerated flow, there can be either steadily accelerated flow or suddenly accelerated flow, in which the critical velocity is reached in less time than in non-accelerated flow

In turbulent flow, it is assumed that instead of a critical velocity determining the onset of droplet breakup, it is the kinetic energy of the turbulent fluctuations that causes the droplet breakup. Since a greater wavelength implies greater kinetic energy of the fluctuations, turbulent velocity fluctuations with a wavelength greater than $2D$ initiate the droplet breakup. The Ohnesorge number in droplet breakup determines the proportion of the effect of viscous forces that the flow in the droplet must overcome relative to the effect of surface tension forces that oppose the deformation of the droplet's surface. When discussing droplet breakup, the Ohnesorge number is defined as $\mathrm{Oh} = \frac{\mu_{\mathrm{L}}}{(\rho_{\mathrm{L}}\sigma D)^{0.5}}$.

2.4 Pressure swirl atomization

In this section, the main characteristics of the injector used in this study are described, as well as the internal and external flow formed in it and the main parameters that quantify the quality of the generated atomization. It is important to note, as detailed in [13], that there is no single type of pressure swirl injector; this type of atomizer can also be divided into hollow cone injectors, full cone injectors, and spill return injectors. Additionally, the rotary motion of the liquid can be generated either by tangential entry ports or by swirlers, that is, helical grooves on the internal walls of the nozzle that generate a tangential velocity component. They can be further divided into convergent pressure swirl injectors and open-end pressure swirl injectors depending on whether they have a convergent swirl chamber or not.

In combustion applications, several types of simplex hollow cone atomizers have been developed, which differ primarily in the method used to impart swirl to the emitted jet. Among these are swirl chambers with tangential slots or drilled holes and swirlers with helical grooves or blades, as illustrated in Figure 2.8. The atomizer in this study is a convergent pressure swirl injector that features three tangential entry ducts to a swirl chamber and expels a hollow cone flow.

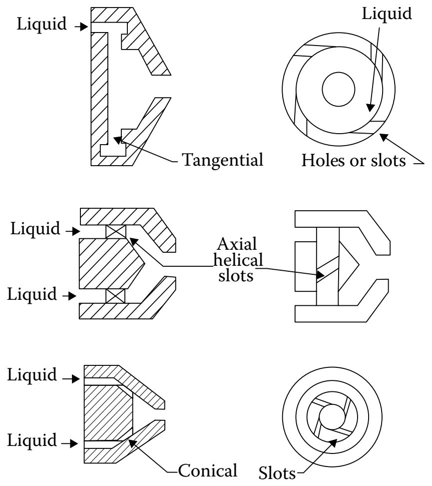

Figure 2.8: Different designs of hollow conwe atomizers. From [9]

The hollow cone flow atomizer with swirl chamber and tangential inlets is considered the simplest and most common among pressure swirl atomizers. In this atomizer, as can be seen in Figure 2.9, the liquid is introduced into the swirl chamber through tangential ducts that generate high angular velocity, thus creating a vortex with an air core. The outlet of the swirl chamber is the final orifice, and the rotating liquid flows through this orifice with axial and radial momentum to exit the atomizer in the form of a hollow conical sheet, with the actual cone angle determined by the magnitude of the tangential and axial components of the velocity at the outlet.

In practice, to achieve the developed flow of the spray where this hollow cone forms, the flow goes through several stages as pressure increases. These stages are shown in Figure 2.10 and are described below: for initial low pressures, the liquid drips from the orifice and then forms a cylindrical jet that undulates. As the flow rate and the pressure difference supplied for injection increase, a sheet begins to form that does not become conical but is narrow and breaks into large droplets. Once the necessary pressure difference is reached for the injected fuel to form the conical sheet, this sheet expands, its thickness decreases, and it soon becomes unstable and disintegrates into ligaments and then droplets, forming a well-defined hollow cone spray. These stages are shown in Figure 2.10 and are described below: at initial low pressures, the liquid drips from the orifice and then forms a cylindrical jet that wiggles. As flow rate and pressure difference supplied for injection increase, a sheet begins to form, which does not become conical

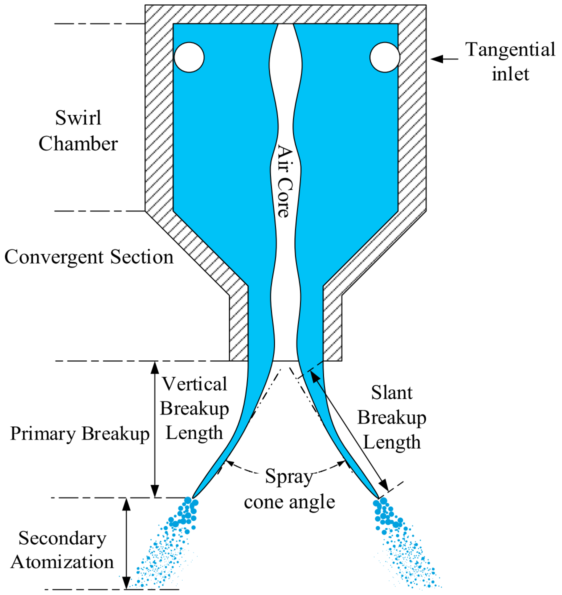

Figure 2.9: Schematic of the geometry and flow formed in a pressure swirl atomizer. Taken from [13]

but it narrows and breaks into large droplets. Once the necessary pressure difference for the injected fuel to form the conical sheet is reached, this sheet expands, its thickness decreases, and soon becomes unstable, breaking into ligaments and then droplets in the form of a well-defined hollow cone spray.

One of the main disadvantages of the simplex atomizer is that the flow rate depends directly on the square root of the injection pressure difference. Therefore, doubling the injected flow rate requires a fourfold increase in injection pressure. For low-viscosity liquids, the lowest injection pressure at which atomization can be achieved is approximately 100 kPa. This means that an increase in flow rate to about 20 times the minimum value would require an injection pressure of 40 MPa. On the other hand, if the maximum flow rate were allowed at a more acceptable injection pressure, say around 7 MPa, then at the lowest flow rate the injection pressure would be only 17.5 kPa (i.e., around 2.5 psi), and the quality of atomization would be extremely poor. This basic disadvantage of the simplex atomizer has led to the development of various wide-range atomizers, such as duplex, dual-orifice, and spill atomizers, in which maximum-to-minimum flow rate ratios greater than 20 can be achieved with injection pressures not exceeding 7 MPa.

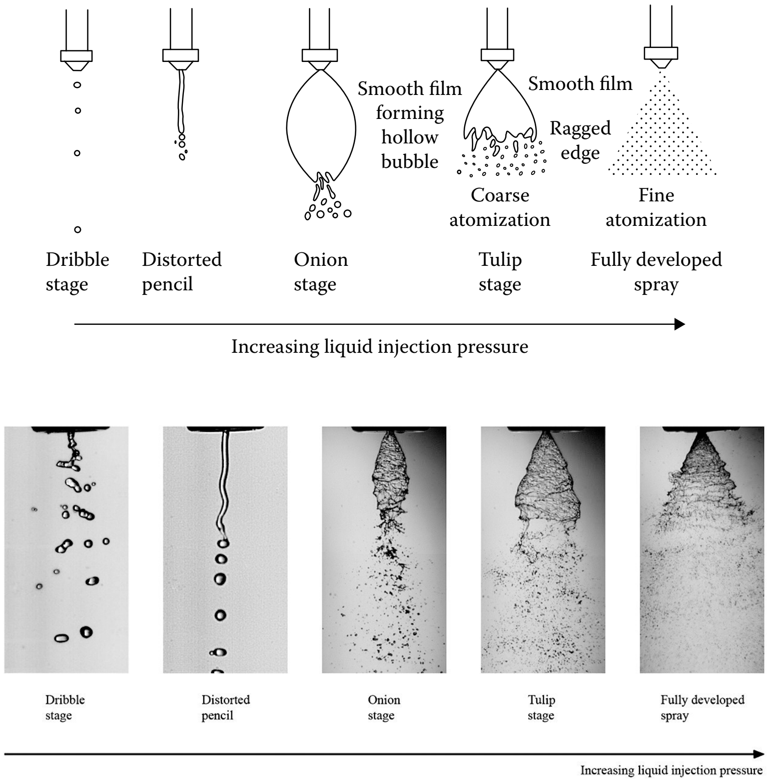

Figure 2.10: Stages in spray development with increase in liquid injection pressure. Tomado de [9].

2.4.1 Flow in pressure swirl atomizers

In other types of atomizers, the external spray flow pattern is not so much dependent on the internal flow within the atomizer but on external forces acting on the flow. In airblast atomizers, for example, the shape of the external spray and droplet size are determined by the air streams used, while in rotary atomizers, it is the shape and angular velocity of the rotating disc that are decisive. However, in pressure swirl atomizers, the characteristics of the internal flow are of paramount importance as they control the thickness and uniformity of the annular liquid film formed at the final discharge orifice, as well as the relative magnitude of the axial and tangential velocity components of this film. Therefore, it is of great practical interest to examine the interrelationships between the characteristics of the internal flow, design variables of the nozzle, and important spray characteristics such as cone angle and mean droplet size.

Despite the geometric simplicity of the simplex atomizer, the hydrodynamic processes occurring within the nozzle are highly complex. This is why in the literature on these atomizers, there are many analytical and experimental correlations that allow establishing quantitative relationships between the main dimensions of the atomizer and various flow parameters, such as the discharge coefficient and the initial spray cone angle.

Flow number

This first parameter is generally used for all types of pressure atomizers [9]. It quantifies the ability of an atomizer to increase mass flow as the square root of the supplied pressure difference for injection increases. It is said to measure the 'effective flow area' of an atomizer because it quantifies to what extent an atomizer increases mass flow when the square root of the injection pressure difference is increased.

$$\text{Flow rate} = (\text{Flow number}) \cdot (\text{Injection pressure differential})^{0.5}$$

In the aerospace sector in the United States, this number is defined independently of the density of the injected liquid since, in this sector, all atomizers generally work with the same fluid, aviation kerosene, which has a density of 765 kg/m^3.

$$\mathrm{FN_{US}} = \frac{\text{Flow rate, lb/h}}{(\text{ Injection pressure differential, psid })^{0.5}} \tag{2.1}$$

Instead, to determine a flow number in an atomizer taking into account the density of the liquid and to have units of area, this parameter is defined as:

$$\mathrm{FN} = \frac{\text{Flow rate, kg/s}}{(\text{Pressure differential, Pa})^{0.5}(\text{Liquid density, kg/m}^3)^{0.5}} \tag{2.2}$$

In pressure swirl atomizers, this flow number is mainly affected by the dimensions of the swirl chamber. A larger diameter of the swirl chamber increases centrifugal inertia due to rotational flow, which increases the diameter of the air core, restricting and decreasing the injected flow rate. On the other hand, the diameter of the orifice, as well as the diameter of the tangential inlet ports, influence the flow number proportionally.

Swirl number

The swirl number S is a dimensionless parameter that quantifies the ratio between the axial flow of angular momentum and the product of the axial flow of axial momentum and a characteristic diameter [14]. This ratio quantifies the convective transport of tangential momentum versus the convective transport of axial momentum in the axial direction, both tangential and axial momentum for the same cross-sectional area of the injector. That is, if S has values greater than unity; $S > 1$, it means that the injector is mainly transporting tangential momentum rather than axial momentum in the axial direction through the cross-sectional area at that axial position. Conversely, if $S < 1$, it means that at that axial position, the injector transports more axial momentum than tangential momentum. Mathematically, this number is written as:

$$S = \frac{2}{D}\frac{G_\theta}{G_x} = \frac{1}{R}\frac{\int_A (\rho U_\theta r)\,\vec{u}\cdot d\vec{A}}{\int_A (\rho U_x)\,\vec{u}\cdot d\vec{A}} \tag{2.3}$$

Where:

G_0 is the axial flow of tangential momentum through area A.

G_x is the axial flow of axial momentum through area A.

A is the area of a cross-section of the atomizer at a specific axial position x.

U_θ is the tangential velocity of the flow at a point on A.

U_x is the axial velocity of the flow at a point on A.

Note that in this notation, the coordinate axis x corresponds to the axial direction of the flow, unlike other descriptions where the z axis is the axis corresponding to that direction. Another version of this dimensionless parameter can be calculated for any point in the flow domain of an atomizer. This version is known as the geometric swirl number and is calculated from the tangential velocity $U_\theta = \omega r$, where ω is the angular velocity of the fluid particle with respect to the axial axis and U_x is the axial velocity:

$$S_g = \frac{\omega r}{U_x} = \frac{U_\theta}{U_x} \tag{2.4}$$

Discharge coefficient

In general, for all pressure atomizers, this discharge coefficient measures the ratio between the actual mass flow rate and the theoretical flow in the atomizer.

$$C_D = \frac{\dot{m}_\mathrm{L}}{A_\mathrm{o}(2\rho_\mathrm{L}\Delta P_\mathrm{L})^{0.5}} \tag{2.5}$$

Its value therefore lies in $0 \leq C_D \leq 1$. Where $\dot{m}$L is the actual flow exiting the atomizer and Ao$(2\rho_\mathrm{L}\Delta P_\mathrm{L})^{0.5}$ is the theoretical flow given by the area of the outlet orifice, the liquid density, and the pressure difference of the injection. This equation is also written as $\dot{m}\mathrm{L} = C_D A\mathrm{o}(2\rho_\mathrm{L}\Delta P_\mathrm{L})^{0.5}$ to calculate the actual flow from the theoretical flow and the discharge coefficient.

In pressure swirl atomizers, this coefficient is quite low due to the presence of the air core within the swirl chamber, which significantly reduces the cross-sectional area of flow outlet. By assuming a free, inviscid vortex flow with no losses due to friction within the swirl chamber, and also considering the presence of an air core, it is demonstrated that the C_D of a pressure swirl atomizer is independent of the injection pressure and instead depends on the total cross-sectional area of the tangential inlet ports, the dimensions of the swirl chamber, and the area of the outlet orifice.

There are many experimental correlations for the discharge coefficient that include the effects of viscous flow and friction losses. For example, there is the relationship obtained by Lefebvre, and its equation and evolution are shown in Figure 2.11.

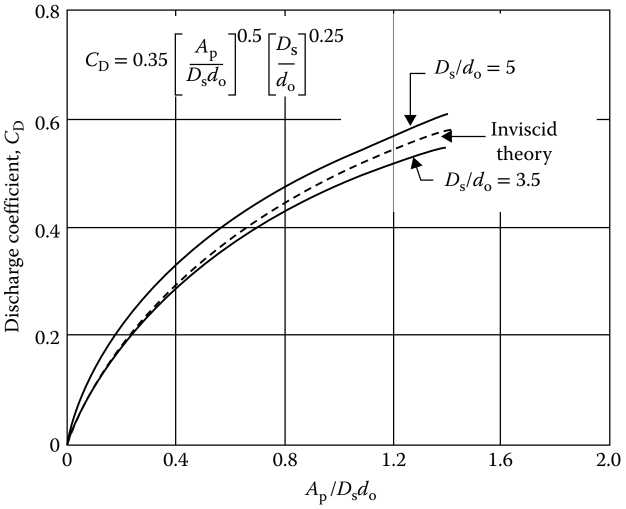

Figure 2.11: Relationship between the discharge coefficient and the geometry of the pressure swirl atomizer [9]

In pressure swirl atomizers, friction losses influence the magnitude of the discharge coefficient in two opposing ways. On one hand, friction losses increase the pressure drop in the atomizer, which decreases the value of the discharge coefficient. On the other hand, friction in the swirl chamber reduces the rotational flow and decreases the diameter of the air core, which increases the actual flow rate, thereby raising the discharge coefficient. The magnitude of these two effects primarily depends on the geometric characteristics of the atomizer. Depending on the atomizer's application, there are studies that define real intervals for the atomizer's geometric parameters to achieve high discharge coefficient values while considering the effects of friction losses.

Air core formation

As explained in [13], the air core that forms within the swirl chamber is an inherent characteristic of the flow in this type of atomizer, as this air core allows the liquid to be expelled in the form of a conical sheet. For the air core to form, the centrifugal force, that is, the centrifugal inertia of the liquid, must overcome the viscous force that keeps the liquid cohesive and generate a low-pressure region near the outlet orifice. This centrifugal force experienced by a fluid particle is proportional to the square of its tangential velocity:

$$dF_s = dm\frac{W^2}{r} \tag{2.6}$$

Due to the conservation of angular momentum, the tangential velocity is given by the tangential velocity at which the liquid enters the swirl chamber through the tangential ports and the radius at the base of the swirl chamber:

$$Wr = W_t R_{sw} \tag{2.7}$$

At the same time, it can be said that this force is proportional to the Reynolds number of the tangential inlet into the swirl chamber and also proportional to the swirl number:

$$Re_t = \frac{\rho_l W_t D_t}{\mu_l} \qquad S_n = \int VWr^2dr / \int r_0 V^2 rdr \tag{2.8}$$

Based on this Reynolds number, two values of the centrifugal force can be distinguished that indicate the state of air core formation, F_{scr1} and F_{scr2}. F_{scr1} is the value of the centrifugal force below which no air core forms and above which an unstable air core forms, and F_{scr2} is the value of the centrifugal force for which a stable air core forms. Once the air core stabilizes, as the Reynolds number increases, the radius of the air core can increase until it reaches an asymptotic behavior where it remains constant even if the Reynolds number increases.

Fuel film

The thickness of the conical sheet expelled by a pressure swirl atomizer is of great interest as it quantifies the stability of this sheet and is therefore related to the ability to form droplets from this type of flow. Lefebvre in [9] presents an expression derived from a theoretical analysis that expresses the thickness of the liquid (fuel) film as a function of the flow number (FN), the density and viscosity of the fuel, the injection pressure difference, and the geometric parameters of the atomizer. However, when comparing different theoretical equations for the thickness of the fuel film with experimental results, Lefebvre concludes that the correlations assuming inviscid flow best predict the experimental values. Several experimental studies agree on the proportional dependency between the Sauter Mean Diameter (SMD) and the thickness of the fuel film. This proportionality can be seen in the figure 2.12.

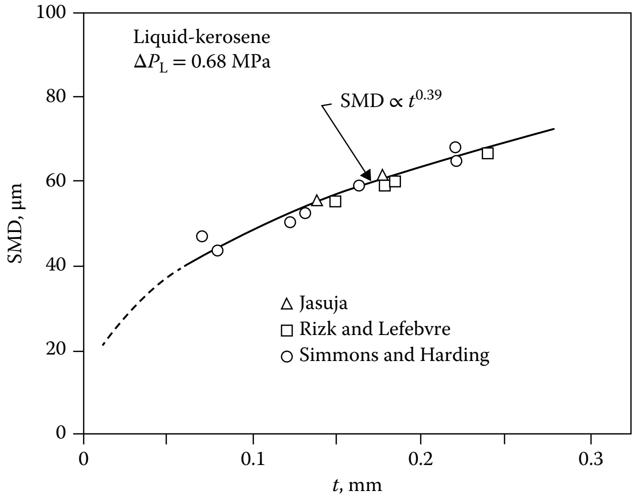

Figure 2.12: Variation of the average droplet size (SMD) as a function of the fuel film thickness [9].

Spray Penetration

La penetración de un spray puede definirse como la distancia máxima que alcanzan las partículas de líquido cuando se inyecta en aire estancado. Esta longitud está gobernada por las magnitudes relativas de dos fuerzas opuestas: la energía cinética del chorro líquido inicial y la resistencia aerodinámica del gas circundante. La velocidad inicial del chorro suele ser alta, pero a medida que avanza la atomización y aumenta el área superficial del líquido atomizado, su energía cinética se disipa gradualmente por pérdidas por fricción hacia el gas. Cuando las gotas finalmente han agotado su energía cinética, su trayectoria posterior está dictada principalmente por la gravedad y/o el movimiento del gas circundante. En general, un spray compacto y estrecho tendrá una alta penetración, mientras que un spray bien atomizado de amplio ángulo de cono, que incurre en más resistencia al aire, tenderá a tener una baja penetración. Para las boquillas simplex y de doble orificio que operan en los combustores de turbinas de gas, Lefebvre establece penetración del spray es inversamente proporcional a la raíz cúbica de la presión del gas ambiente.

Spray cone angle

The spray angles produced by pressure swirl nozzles are of particular importance in their application to combustion systems. In gas turbine combustors, the spray angle exerts a strong influence on ignition performance, flameout limits, and emissions of unburned hydrocarbons and smoke. This is because the spray angle determines the spatial distribution of droplets generated through this type of atomization. The hollow conical structure of the spray is significantly exposed to the surrounding air flow. Therefore, an increase in the spray cone angle enhances this exposure, leading to better atomization, improved fuel-air mixing, and better dispersion of fuel droplets throughout the combustion volume. Many previous studies on gas turbine combustors have shown that pressure swirl atomizers with wide spray angles are often characterized by a fairly uniform temperature distribution and relatively low soot concentrations in the exhaust gases [12].

The spray cone angle tends to decrease with a reduction in injection pressure. At the same time, its value reduces with an increase in viscosity due to greater energy losses and reduced angular momentum, consequently lowering the tangential velocity. It is also known that the spray cone angle decreases drastically as the air core vanishes. Rizk and Lefebvre [15] derived a theoretical expression to calculate the cone angle based on the atomizer's geometry, the properties of the liquid, and the injection pressure difference:

$$2\theta_{\mathrm{m}} = 6K^{-0.15}\left(\frac{\Delta P_{\mathrm{L}} d_{\mathrm{o}}^{2} \rho_{\mathrm{L}}}{\mu_{\mathrm{L}}^{2}}\right) \tag{2.9}$$

Where θ_m is the angle measured between the spray cone line and its axis of symmetry, and K is the geometric parameter of the atomizer, given by $K = \frac{A_{\mathrm{p}}}{D_{\mathrm{s}} d_{\mathrm{o}}}$. The spray cone angle tends to decrease with increasing viscosity due to greater energy losses and a reduction in the liquid's angular momentum. The viscosity of the liquid is inversely related, while the density and injection pressure are directly related to the spray cone angle. Other studies suggest that the spray cone angle tends to decrease and droplet size tends to increase with increasing ambient pressure.

Chapter 3

Computational numerical modeling

3.1 Physical Conservation models

To physically describe the flow of a fluid in a formal and detailed way, computational fluid dynamics is based on three conservation principles: the law of conservation of mass, the conservation of momentum (Newton's second law) and the conservation of energy. These principles are supported by constitutive equations, that is, equations derived from experimentation that correlate properties of the flow or fluid. Furthermore, a fluid is considered as a continuous substance made up of infinitesimal particles of fluid that, from a macroscopic point of view, make up a continuous medium.

In this field of physics two approaches can be used, the Lagrangian approach or the Eulerian approach. In this study, the Eulerian approach is used, which describes the flow (from an inertial reference system) in each spatial position of the domain at each instant of time. In each of these spatial positions, an infinitesimal volume can be studied, known as an infinitesimal control volume, in which the three conservation laws must be met: mass, momentum and energy. From this balance results a system of non-linear partial differential equations known as the Navier Stokes Equations, whose solution provides the value of the variables that describe the flow and the properties of the fluid which are described mathematically by means of scalar, vector or tensor fields according to the type of physical magnitude to which they correspond.

Computational fluid dynamics (CFD) builds on these physical-mathematical models to construct discretized models and provide numerical solutions in many research and engineering applications. The main models among these, which are also the starting point for modeling the multiphase flow in this study, are described below.

3.1.1 Reynolds Transport Theoreme

Through Reynolds Transport Theorem (RTT), conservation laws can be applied to a fixed mass of fluid, seen as a closed system m_{syst}. This theorem is based on the fact that: at time t, the mass m_{syst} occupies a control volume V, and simultaneously, due to the velocity field $\mathbf{U}(x, y, z, t)$, which causes m_{syst} to move, there are inflows and outflows through the control surface S of the control volume. Considering the above, RTT states that the rate of change of an extensive property B of m_{syst} is equivalent to the rate of change of this property within V, plus the net outward flux of this property per unit mass b. This latter assertion is made because: at time t, as can be seen in figure 3.1, the part of the mass exiting the control volume (Region II) belongs to the original system m_{syst}, and the part entering V (Region I) does not belong to m_{syst}. In this way, the rate of change of any extensive property B_{syst} of the fixed mass m_{syst} can be determined from the content of the control volume V and the fluxes existing through its surface

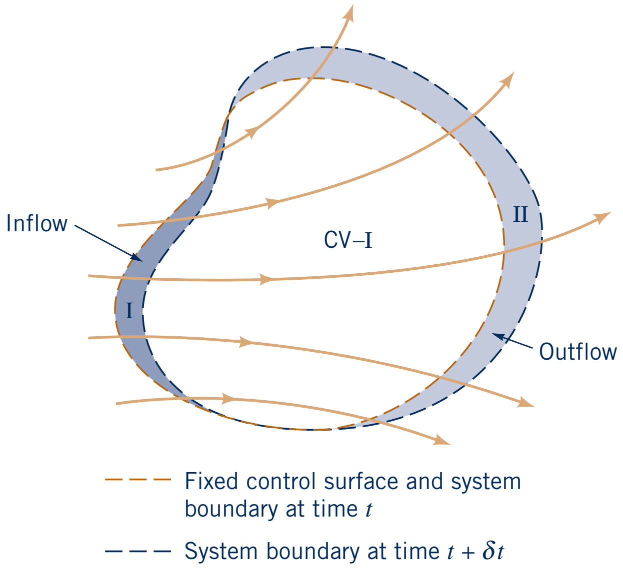

Figure 3.1: Control volume and system for flow through an arbitrary, fixed control volume. Tomado de [16]

at time t. Thanks to this theorem, conservation principles can be written for a mass of fluid m_{syst} that is contained within, and simultaneously flows through, a control volume V.

$$\frac{\mathrm{D}B_{\mathrm{sist}}}{\mathrm{D}t} = \int_{\mathrm{V}} \frac{\partial}{\partial t}(\rho b)dV + \int_{\mathrm{S}} \rho b\mathbf{U} \cdot \mathbf{n}dA \tag{3.1}$$

3.1.2 Mass Conservation

In a system with fixed mass, the law of conservation of mass states that:

$$\frac{\mathrm{D}m_{sist}}{\mathrm{D}t} = 0 \tag{3.2}$$

And through RTT, if B_{sist} is taken as $B_{sist} = m_{syst}$, then it follows that:

$$\frac{\mathrm{D}m_{sist}}{\mathrm{D}t} = \frac{\partial}{\partial t}\int_{V} \rho \mathrm{d}V + \int_{S} \rho\mathbf{U} \cdot \mathbf{n}\mathrm{d}S = 0 \tag{3.3}$$

By applying the Gauss or divergence theorem to the surface integral, we obtain an integral over V. Applying this balance to a volume V of infinitesimal size, we obtain the continuity equation in its differential form:

$$\frac{\partial \rho}{\partial t} + \nabla \cdot (\rho\mathbf{U}) = 0 \tag{3.4}$$

3.1.3 Momentum conservation

The conservation of momentum law is another way of referring to Newton's second law, which states that the total derivative of the momentum of a mass is equivalent to the resultant sum of all the forces acting on that mass:

$$\frac{\mathrm{D}(m\mathbf{U})}{\mathrm{D}t} = \sum \mathbf{f} \tag{3.5}$$

Through TTR, we have:

$$\frac{\mathrm{D}(m\mathbf{U})}{\mathrm{D}t} = \frac{\partial}{\partial t}\int_V \rho\mathbf{U}\mathrm{d}V + \int_S \rho\mathbf{U}\mathbf{U}\cdot\mathbf{n}\mathrm{d}S = \sum \mathbf{f} \tag{3.6}$$

In the same way as done in the mass conservation analysis, by employing Gauss's theorem and considering an arbitrary volume, here, we can transform the momentum conservation equation into a differential form, taking into account a differential fluid element ρdV:

$$\rho\frac{\mathrm{D}\mathbf{U}}{\mathrm{D}t}dV = \rho\frac{\partial\mathbf{U}}{\partial t} + \rho\mathbf{U}\cdot\nabla\mathbf{U} = \sum \mathbf{f} \tag{3.7}$$

The term $\sum \mathbf{f}$ in the previous equation can be expanded by considering the forces acting on the infinitesimal fluid element contained in dV, which, in general, are of two types:

- Surface forces (pressure, normal and shear stresses, surface tension, etc.);
- Body forces (gravity, centrifugal and Coriolis forces, electromagnetic forces, etc.).

All surface forces can be grouped within the stress tensor.

$$\rho\frac{\mathrm{D}\mathbf{U}}{\mathrm{D}t}dV = \rho\frac{\partial\mathbf{U}}{\partial t} + \rho\mathbf{U}\cdot\nabla\mathbf{U} = \nabla\cdot\mathbf{T} + \sum \mathbf{F}^{body\ forces} \tag{3.8}$$

Where: $\mathbf{T} \equiv (\sigma_{xx}, \tau_{xy}, \ldots, \tau_{yz}, \sigma_{zz})$

Si se descompone la componente esférica del tensor T en esfuerzos normales de presión y la componente de esfuerzos viscosos normales:

$$\sigma_{xx} = -p + \tau_{xx} \quad \sigma_{yy} = -p + \tau_{yy} \quad \sigma_{zz} = -p + \tau_{zz} \tag{3.9}$$

Then we have a more detailed equation:

$$\rho\frac{\partial\mathbf{U}}{\partial t} + \rho\mathbf{U}\cdot\nabla\mathbf{U} = -\nabla p + \nabla\cdot\tau + \sum \mathbf{F}^{body\ forces} \tag{3.10}$$

3.1.4 Energy conservation

In CFD models where solving an additional field beyond velocity or pressure is required, the principle of conservation of energy is utilized in addition to the two principles mentioned earlier. For instance, in compressible flows, where solving the density field is necessary, or in flows involving heat transfer, where solving temperature fields or heat flux fields is required. Depending on the forms of energy transformed within the flow, this conservation principle can be expressed in various ways. In this work, only two-phase, incompressible flow with immiscible phases at constant temperature is considered, hence no detailed discussion on this conservation principle is provided. This also implies that equations associated with this principle are not solved within the system of discretized equations and numerically solved.

3.2 Finite Volume Method

The partial differential equations resulting from the previous section are known as the Navier-Stokes equations for a Newtonian fluid in incompressible flow. Obtaining an analytical solution to these equations is very difficult because they describe a multiscale phenomenon in which small variations in the variables describing the flow (velocity, pressure) are distributed in all spatial directions, amplifying and mixing these disturbances at different spatiotemporal scales. This is primarily due to the nonlinear dependence that exists between the instantaneous rates of change of the flow's linear momentum. Attempting to capture all these variations and distributions of disturbances in analytical solutions would result in solutions that are extremely complex to construct.

Through numerical methods, numerical solutions to systems of partial differential equations can be obtained by using small subdomains where the linear behavior of derivatives is approximated using Taylor series (finite differences), or by numerically integrating the derivatives to perform balances within these subdomains (finite volumes), or by using shape functions that behave in the same way as the derivatives of the original equation (finite elements). Thanks to the exponential growth of algebraic computational power in computers, numerical solutions to these types of problems are feasible, useful, and enable the development and advancement of many engineering techniques.

In this study, the OpenFOAM calculation software is used, which implements the finite volume method to solve the Navier-Stokes equations. This numerical method has several advantages over other methods:

- One of the distinctive features of the finite volume method is that it aims to conserve physical quantities such as mass, momentum, and energy, as it is based on integrating equations over control volumes, which facilitates capturing and balancing the flows of these physical quantities.
- This method is more efficient than others in unstructured meshes, as it does not require main directions to define the directions in which flows or variations are calculated but rather reconstructs this information from neighboring cell information and the flows through them. This, in turn, allows working with domains with complex geometries where implementing a structured mesh may be difficult.
- The integral operators of this method allow better capturing, compared to differential operators, the flow zones where there are discontinuities or strong gradients because instead of approximating the rates of variation themselves, they sum the flows produced by the gradients. This makes this method appropriate for free surface multiphase flows.

The finite volume method requires dividing the domain into subdomains known as control volumes or cells. The conservation equation is integrated over each of these subdomains in its differential form, and a balance of the transported variables is made. Thus, if conservation is ensured within each cell, conservation is ensured throughout the entire domain. An example of discretizing a two-dimensional domain into cells is shown in Figure 3.2.

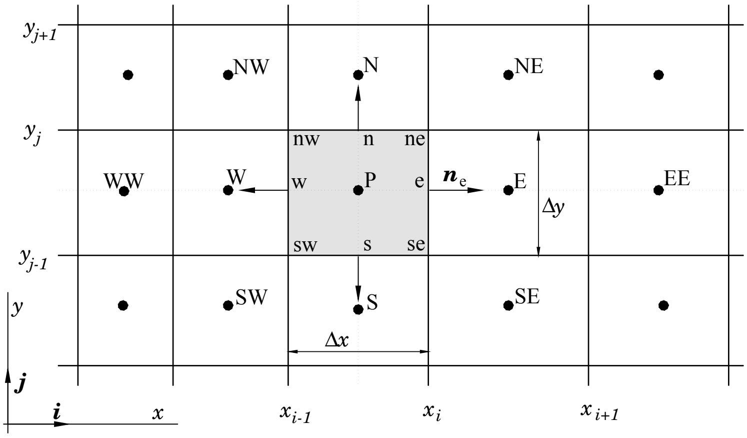

Figure 3.2: Discretization and typical notation of a two-dimensional domain in finite volumes. Taken from [17].

This method allows solving problems modeled by conservation principles written in the form of differential equations following these main steps:

1. Divide the domain into control volumes (finite volumes) or cells.
2. Integrate the conservation equations over each cell and obtain algebraic equations where the unknowns are the values of the conserved variable evaluated at the cell centers.
3. Couple the algebraic equations of all cells into a single algebraic system and solve.

The explanation of [17] regarding how step 2 is performed is summarized. This is exemplified through a basic conservation principle known as the transport of a passive scalar, which models the transport of a scalar ϕ in a two-dimensional domain as shown in Figure 3.2. This conservation principle can be written in a differential form as follows

$$\underbrace{\nabla\rho\phi\cdot\mathbf{v}}_{\text{Advection}} = \underbrace{\nabla\cdot\Gamma\nabla\phi}_{\text{Difussion}} + \underbrace{q_\phi}_{\text{Source Term}} \tag{3.11}$$

Integrating over a cell with volume V and with surface area S, and resorting to the divergence theorem, the integral form of the conservation principle is obtained, in which the three types of transport that are also present in the conservation equations of momentum flow are indicated:

$$\underbrace{\int_S \rho\phi\mathbf{v}\cdot\mathbf{n}\mathrm{d}S}_{\text{Advection}} = \underbrace{\int_S \Gamma\nabla\phi\cdot\mathbf{n}\mathrm{d}S}_{\text{Difussion}} + \underbrace{\int_V q_\phi\mathrm{d}V}_{\text{Source Term}} \tag{3.12}$$

It can be seen that in Equation 3.12, the advective and diffusive transport terms are calculated as a surface integral over the entire surface of the cell, which means that these integrals calculate the net flow of ϕ through the cell's surface. The terms $\rho\phi\mathbf{v}$ and $\Gamma\nabla\phi$ correspond, therefore, to the advective and diffusive flux terms, respectively. If denoted as f, then the net flux of either of these two terms through the cell's control surface can be written as:

$$\int_S f\ \mathrm{d}S = \sum_k \int_{S_k} f\ \mathrm{d}S \tag{3.13}$$

Where S_k is one of the faces of the cell with surface S. At this point, the two most important numerical steps of this method must be implemented: Numerical integracion and Interpolation.

3.2.1 Numerical Integration

The integrals in Equation 3.13 are approximated using different numerical interpolation schemes, among which the most common ones are: midpoint rule, Gauss quadrature, or Simpson's rule. If the midpoint rule is used, for example:

$$\int_{S_k} f \, \mathrm{d}S_k = \bar{f} S_k \approx f_k S_k$$

Where f_k is the value of f at the midpoint of the face with surface S_k, then a second-order approximation is being used. However, if Simpson's rule is used, for example, to approximate the flux of f (advective or diffusive) through the east face of the cell with centroid P (see Figure 3.2), a fourth-order error approximation is obtained [17].

$$\int_{S_e} f \, \mathrm{d}S_e \approx \frac{S_e}{6} \left(f_{ne} + 4 f_e + f_{se} \right)$$

The volume integrals that calculate the contribution of ϕ due to the source terms of the conservation principles, such as q_ϕ, can also be numerically approximated using the midpoint rule, obtaining a second-order error approximation:

$$Q_{\phi P} = \int_V q_\phi \, \mathrm{d}V = \bar{q_\phi} V_P \approx q_{\phi P} V_P$$

3.2.2 Interpolation of values at the centers of the faces

Since the goal is to construct a system of equations in terms of the values of the transported variable ϕ evaluated at the cell centers, and because the numerical integration schemes from the previous section are in terms of the values of ϕ evaluated at the faces or corners of the cells, interpolation is performed using different interpolation schemes based on the values of ϕ at the cell centers. For example, if working with the conservation equation integrated over cell P and evaluating the convective fluxes, i.e., $f = \rho \phi \mathbf{v}$, then for the east face of Figure 3.2, using the midpoint rule to approximate the integral:

$$\int_{S_e} \rho \phi \mathbf{v} \cdot \mathbf{n}_e \, \mathrm{d}S_e \approx \left(\rho \phi u \right)_e S_e = \rho_e \phi_e u_e S_e \tag{3.14}$$

The value of ϕ_e in the above equation needs to be interpolated with the values of ϕ at the cell centers. To do this, various interpolation schemes can be used, among which the most common ones are detailed below.

Upwind scheme (UDS)

This scheme is first-order accurate and approximates the value of ϕ on the east face ϕ_e from the value at the center of the upstream cell:

$$\phi_\mathrm{e} = \begin{cases} \phi_\mathrm{P} \text{ if } (\mathbf{v} \cdot \mathbf{n})_\mathrm{e} > 0; \\ \phi_\mathrm{E} \text{ if } (\mathbf{v} \cdot \mathbf{n})_\mathrm{e} < 0 \end{cases} \tag{3.15}$$

If a Taylor expansion for ϕ_e around P is used to determine the error order of this approximation, it can be observed that the leading truncation term takes the form of a diffusive flux, which results in diffusing the error in oblique flows to the mesh. This makes this scheme require very fine meshes to avoid this numerical diffusion.

Linear Interpolation (CDS)

Another very common scheme, but second-order accurate, is the centered linear interpolation scheme on the face:

$$\phi_{\mathrm{e}} = \phi_{\mathrm{E}}\lambda_{\mathrm{e}} + \phi_{\mathrm{P}}\left(1-\lambda_{\mathrm{e}}\right) \tag{3.16}$$

Donde $\lambda_{\mathrm{e}} = \frac{x_{\mathrm{e}}-x_{\mathrm{P}}}{x_{\mathrm{E}}-x_{\mathrm{P}}}$.

Using this scheme involves assuming a linear profile between points ϕ_P and ϕ_E passing through ϕ_e, which also allows approximating the gradient of ϕ that appears when diffusive fluxes are approximated:

$$\left(\frac{\partial \phi}{\partial x}\right)_{\mathrm{e}} \approx \frac{\phi_{\mathrm{E}}-\phi_{\mathrm{P}}}{x_{\mathrm{E}}-x_{\mathrm{P}}} \tag{3.17}$$

These and other interpolation schemes allow interpolating the values of the transported variable from the values at the cell centers and obtaining the linear system of equations for all cells in the domain.

3.3 Temporal integration

The temporal numerical advancement of conservation equations is implemented using numerical integration schemes. When there is a temporal derivative in a conservation principle, then regardless of the spatial discretization scheme, one always arrives at a temporal advancement equation of the form [17]:

$$\frac{\mathrm{d}\phi(t)}{\mathrm{d}t} = f(t,\phi(t)); \quad \phi\left(t_0\right) = \phi^0 \tag{3.18}$$

Where f is the set of linear or nonlinear operations resulting from using a spatial discretization scheme on a conservation equation of the variable ϕ. In the case of FVM, f corresponds to the terms of the algebraic equation of the linear system obtained by numerically integrating and interpolating the values on the faces. And, where ϕ^0 is the initial condition from which this temporal advancement of ϕ can be numerically calculated. To do this, the above equation is integrated over the time interval required to advance the solution $[t_n, t_{n+1}]$:

$$\int_{t_n}^{t_{n+1}} \frac{\mathrm{d}\phi}{\mathrm{d}t}\,\mathrm{d}t = \phi^{n+1} - \phi^n = \int_{t_n}^{t_{n+1}} f(t,\phi(t))\mathrm{d}t \tag{3.19}$$

The time interval $\Delta t = [t_n, t_{n+1}]$ defines the physical time that separates each step in the numerical solution's time advancement. For the numerical approximation to be good, Δt must be very small so that the error is reduced, as seen in Figure 3.3, as each numerical integration scheme entails an error due to the nonlinear variation of ϕ over time, which will decrease if smaller time intervals are used.

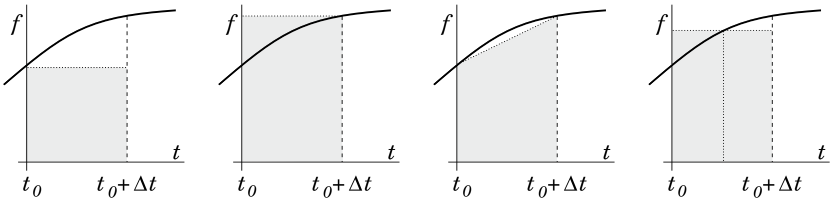

Figure 3.3: Approximation of the integral in time of equation3.19 using different schemes (from left to right: explicit Euler, implicit Euler, trapezoid rule, midpoint rule). Taken from [17].

- The first of the numerical integration schemes in Figure 3.3 (from left to right) is known as **Explicit Euler**. It starts from the initial condition and assumes that the evolution of ϕ is constant over time. Therefore, as seen in equation 3.20, the solution at time $n+1$ is directly and explicitly obtained from the previous time step n. This scheme can become unstable for problems with a strong dependence on the direction of temporal advancement based on the spatial mesh size.

$$\phi^{n+1} = \phi^n + f\left(t_n, \phi^n\right)\Delta t \tag{3.20}$$

  This scheme is first-order accurate $\mathcal{O}(\Delta t)$.

- The second temporal integration scheme is known as **Implicit Euler**, as the time advancement depends implicitly on its future value ϕ^{n+1}. This method is unconditionally stable and does not depend on the spatial mesh size to provide stable solutions.

$$\phi^{n+1} = \phi^n + f\left(t_{n+1}, \phi^{n+1}\right)\Delta t \tag{3.21}$$

  This scheme is second-order accurate but complicates the time advancement as using it transforms the equations of the linear system modeling the conservation in all cells into an implicit system that requires iterative solution algorithms.

- A third scheme, which combines the two previous ones, has good stability, and is second-order, is known as **Crank-Nicolson**

$$\phi^{n+1} = \phi^n + \frac{1}{2}\left[f\left(t_n, \phi^n\right) + f\left(t_{n+1}, \phi^{n+1}\right)\right]\Delta t \tag{3.22}$$

- A final scheme, which is used in this study, is a combination of the **Explicit Euler** scheme and the **Crank-Nicolson** scheme. Its evolution equation is written in terms of a coefficient $0 \leq \beta \leq 1$ as seen in equation 3.23. Depending on the value of β, this scheme becomes the Explicit Euler scheme ($\beta = 0$) or the second-order $\mathcal{O}(\Delta t^2)$ Crank-Nicolson scheme ($\beta = 1$).

$$\frac{\phi^{n+1} - \phi^n}{\Delta t} = \frac{\beta}{2}\left[f\left(t_n, \phi^n\right)\right] + \left(1 - \frac{\beta}{2}\right)\left[f\left(t_{n+1}, \phi^{n+1}\right)\right] \tag{3.23}$$

Any of these schemes should be chosen according to the stability and accuracy required in each case of numerical modeling.

3.4 Turbulence modelling

Turbulent fluid flow is a phenomenon that becomes very difficult to describe in detail using the mathematical and physical models known to date. Certainly, the Navier-Stokes equations, assuming the hypotheses of classical mechanics, are the ones that best describe and govern the phenomena of mass, momentum, and energy conservation in a flow. However, the nonlinear terms that appear in the total derivative of the momentum of a flow make the solutions to these equations highly complex and difficult to describe. This complexity is partly explained by the fact that the momentum contained by an initially laminar and orderly flow, when subjected to strong gradients generated by strong shear stresses, can transfer its energy in the form of deformations and fluctuations in all spatial directions, forming vortices or eddies. These deformations and fluctuations generate new gradients in their vicinity and thus redistribute their energy, forming smaller-scale fluctuations and deformations, and so on, until they reach such small scales that they can only dissipate at the molecular level in the form of heat. This phenomenon is known as turbulence. The nature of turbulent flow is related to this distribution of energy and momentum transport, which generates very changeable deformations and trajectories in a flow. Since these deformations and fluctuations occur over a very wide spectrum of frequencies and amplitudes, turbulent flow behaves more like a random process, which is easier to describe from a stochastic rather than a deterministic approach.

In this section, some treatments applied to the equations governing a flow are described in order to reduce the range of frequencies to be modeled. In this way, these approaches allow capturing some of the main deformations and fluctuations occurring in a flow within a more reduced and manageable spectrum of spatiotemporal scales. The Reynolds number is a dimensionless number that quantifies the ratio between the inertial scales and the viscous scales of a flow; the higher the ratio, the greater the difference in scales and the greater the energetic potential for the formation of turbulent flow. This transition from laminar to turbulent flow is usually associated with a specific Reynolds number for each type of flow, but the phenomenon that enables the formation of turbulent structures is the generation of vorticity in the flow. Vorticity is a vector whose magnitude quantifies the rotation of the velocity vector of a fluid particle and points in the direction of the axis of rotation.

$$\zeta = \left(\frac{\partial w}{\partial y} - \frac{\partial v}{\partial z}\right)\mathbf{i} + \left(\frac{\partial u}{\partial z} - \frac{\partial w}{\partial x}\right)\mathbf{j} + \left(\frac{\partial v}{\partial x} - \frac{\partial u}{\partial y}\right)\mathbf{k} \tag{3.24}$$

The magnitude of this vector is proportional to the cross-gradients of the velocity components. This is why, for example, in regions where the flow passes near a solid wall, due to the no-slip condition, high shear stresses are generated, and cross-gradients of the velocity components are formed. This leads to the initial rotation of the fluid layers' particles and the formation of vortices. These vortices tend to become unstable, deform, and form new vortices on smaller scales until viscous dissipation occurs when the Reynolds number is sufficiently high.

This phenomenon of energy transfer from large vortices to smaller vortices through non-viscous inertial mechanisms, until the kinetic energy of the smallest vortices is transferred as viscous dissipation in the form of heat, was introduced by Richardson in 1922 and is known as the energy cascade. This concept was further developed and quantified by Kolmogorov in 1941. In this theory, turbulent kinetic energy, which is the energy producing the formation of eddies, is correlated with the wavenumber of these eddies. This relationship is represented by the graph of the energy spectrum of a turbulent flow versus the wavenumber, which estimates the number of eddies per unit length, as shown in the figure 3.4a.

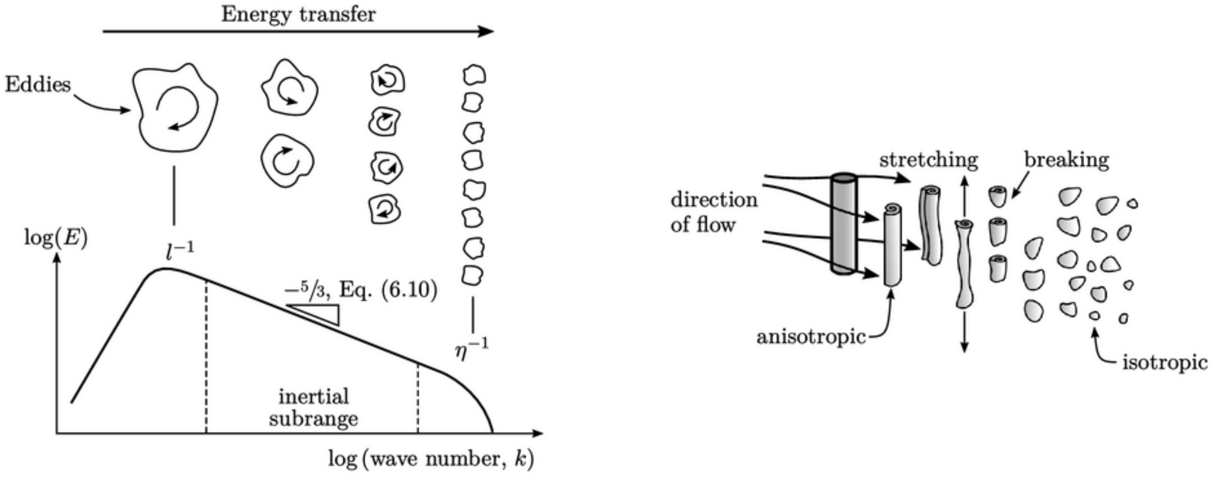

(a) (b)

Figure 3.4: (a). Graphical representation of the turbulent energy spectrum as a function of the wavenumber of all oscillations in the turbulent flow (b). Graphical representation of the formation of eddies from oscillations favored by the main flow direction.

3.4.1 Turbulent fluctuations scales

Assuming the hypotheses of classical mechanics, the Navier-Stokes equations govern this phenomenon of turbulence, and in computational fluid dynamics, these deformations and eddies in a flow can be captured through a numerical solution of the NS equations to the extent that spatial discretizations are small enough to capture the gradients that originate them. Therefore, it is important to understand what determines the size of these scales in which the turbulent flow of a specific problem develops

A flow represented by a characteristic velocity $\mathcal{U}$, a characteristic length $\mathcal{L}$, and a viscosity ν, which are such that they define a very high Reynolds number; $\mathrm{Re} = \mathcal{U}\mathcal{L}/\nu$, then this flow is a candidate to generate turbulent flow. In this turbulent flow, eddies of different sizes will form, which in turn, can each be associated with a length scale ℓ, have a characteristic velocity $u(\ell)$, and exist on a time scale $\tau(\ell) = \ell/u(\ell)$. These length, velocity, and time scales are quantified and classified within the spectrum of wavenumbers of the energy cascade curve. They are usually grouped into three main categories: the scales associated with the production of turbulent kinetic energy $\mathcal{P}(k)$, the scales associated with the inertial subrange where energy transfer occurs, and the scales associated with viscous dissipation ε [18].

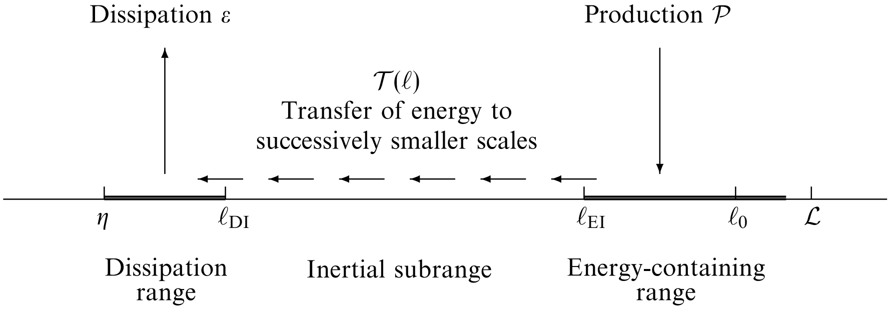

Figure 3.5: A schematic diagram of the turbulent scales in the energy cascade at very high Reynolds number. Tomado de [18].

Energy containing range scales

The eddies of a turbulent flow that form immediately from the undisturbed laminar flow are within the length scale known as the Energy Containing Range. These eddies correspond to the largest eddies of the turbulent flow, which are characterized by being of a magnitude comparable to the problem or flow's own scales (L_{ref}) and have a characteristic velocity on the order of the turbulent intensity, which is comparable to the characteristic velocity of the flow (U). Consequently, the Reynolds number that ensures the formation of these eddies is as high as the Reynolds number characteristic of the main flow, disregarding viscosity effects. Being determined by the main flow, their structure is highly anisotropic as seen in Figure 3.4b.

Inertial subrange scales

As the eddies of the energy-containing range transfer energy to generate smaller eddies through inertial mechanisms, within this range of length scales, viscous effects are also not important. Instead, the energy transfer occurs logarithmically from larger eddies to smaller ones. It is also within this range where turbulence becomes isotropic, and therefore, the energy spectrum becomes a function solely of the average rate of energy dissipation ε and the wavenumber of the eddies κ. It is in this range of scales where the energy spectrum correlates with the wavenumber of the eddies through:

$$E(\kappa) = C\varepsilon^{2/3}\kappa^{-5/3} \tag{3.25}$$

Kolmogorov scales

To define the order of magnitude of the smallest scales at which kinetic energy dissipates in a turbulent flow, a similarity analysis is conducted based on the rate of energy dissipation appearing in the energy conservation equation of a flow. This yields the proportionality between the average rate of energy dissipation in the form of heat ϵ and the velocity and length scales of the vortices that do not deform into smaller vortices but dissipate their energy in the form of heat:

$$\varepsilon \sim \nu(v/\eta)^2 \tag{3.26}$$

Energy dissipation will occur when the Reynolds number indicates that both the inertial scales and the viscous scales have a unit ratio: $v\eta/\nu \sim 1$. This, combined with the previous equation 3.26, provides the order of magnitude of the microscales of heat dissipation, known as

Kolmogorov scales:

$$\text{length:} \quad \eta \sim \left(\frac{\nu^3}{\varepsilon}\right)^{1/4} \tag{3.27}$$

$$\text{velocity:} \quad v \sim (\nu\varepsilon)^{1/4} \tag{3.28}$$

$$\text{time:} \quad \eta/v \sim \left(\frac{\nu}{\varepsilon}\right)^{1/2} \tag{3.29}$$

By correlating these scales of viscous dissipation with the Reynolds number corresponding to the larger scales (Energy Containing Range), $\mathrm{Re} = ul/\nu$, we obtain:

$$\eta \sim l\,\mathrm{Re}^{-3/4}; \quad v \sim u\,\mathrm{Re}^{-1/4}; \quad \eta/v \sim (l/u)\,\mathrm{Re}^{-1/2} \tag{3.30}$$

3.4.2 Cost of a turbulent flow simulation

Because turbulent flow develops over this wide range of scales, the amount of information required to describe such a flow in detail is enormous. In fact, in numerical simulations, one can illustrate the magnitude of the quantity by estimating the number of discrete subdivisions required in a domain to numerically describe the Kolmogorov scales. For example, consider a CFD problem in which the Reynolds number is high enough for turbulent flow to develop. We know from equation 3.30 that the largest turbulent length scales are related to the smallest ones and to the Reynolds number through:

$$\frac{l}{\eta} \sim \mathrm{Re}^{3/4} \tag{3.31}$$

Now, in a three-dimensional problem, where one aims to capture the smallest turbulent scales, one needs to work with volumetric cells of characteristic length Δ. If the problem has a reference characteristic length L, then the number of cells or subdivisions would be given by the ratio of the volumes of the cells and the total volume of the domain:

$$N_{xyz} \sim \left(\frac{L}{\Delta}\right)^3 \tag{3.32}$$

This volume ratio must be of the same order of magnitude as the ratio of the largest to the smallest turbulent scales so that all scales are captured:

$$\left(\frac{L}{\Delta}\right)^3 \sim \left(\frac{l}{\eta}\right)^3 \sim \mathrm{Re}^{9/4} \tag{3.33}$$

Then, a common Reynolds number for turbulent flow in engineering applications, even in external flow, would easily be on the order of 10^5 or lower. With this Reynolds number, the number of cells needed to capture all scales of turbulent flow is:

$$N_{xyz} \sim \mathrm{Re}^{9/4} = \left(10^5\right)^{9/4} = 10^{11.25} \tag{3.34}$$

In current automotive external aerodynamics (2022), some of the largest simulations are run with grids of 10^8 cells on 1000 processor cores. These grid sizes are clearly several orders of magnitude smaller than those required for Direct Numerical Simulation (DNS) of turbulence at the smallest scales. [19].

3.4.3 Computational approaches

Due to the high computational cost that a numerical simulation of turbulent flow may require, various approaches have been developed to treat the Navier-Stokes equations in a special way, saving calculations and reducing the computational cost of numerical models that simulate these fluid flows. These approaches allow obtaining a solution that represents the flow at least at its largest turbulent scales, resulting in a computational model that enables: estimating the main structures of a flow, making average estimates of the forces or coefficients involved in turbulent flow due to the larger scales, and making them useful for engineering designs.

Reynolds Averaged Navier Stokes Equations

One of the most well-known approaches that saves computational cost in numerical simulations is called Reynolds Averaged Navier Stokes Equations (*RANS*). In this approach, the Reynolds decomposition is utilized, where it is assumed that the velocity vector field of a flow, $\mathbf{u}$, is a random variable, and therefore its mean value, $\overline{\mathbf{U}}$, and the fluctuations around this mean value, $\mathbf{u}'$, are defined:

$$\mathbf{u}(\boldsymbol{x},t) = \overline{\mathbf{U}}(\boldsymbol{x}) + \mathbf{u}'(\boldsymbol{x},t) \tag{3.35}$$

If the mean value is defined as:

$$\overline{\mathbf{U}}\left(\boldsymbol{x}\right) = \lim_{T\to\infty} \frac{1}{T}\int_0^T \mathbf{u}\left(\boldsymbol{x},t\right) dt \tag{3.36}$$

then, $\mathbf{u}'$ represents the turbulent fluctuations, which define those eddies that form and disintegrate in the cascade of turbulent kinetic energy:

$$\mathbf{u}'(\boldsymbol{x},t) = \mathbf{u}(\boldsymbol{x},t) - \overline{\mathbf{U}}(\boldsymbol{x}) \tag{3.37}$$

Introducing this decomposition into the conservation equations of a viscous and incompressible flow and averaging them over time leads to the equations known as Reynolds Averaged Navier Stokes (RANS) equations. In [20], the result of introducing this decomposition into the continuity equation and the momentum conservation equation for this type of flow is shown.

Introducing Reynolds decomposition into continuity equation gives:

$$\nabla\cdot\mathbf{u} = 0 \quad \to \quad \nabla\cdot\overline{\mathbf{U}} + \nabla\cdot\mathbf{u}' = 0 \tag{3.38}$$

Averaging in time:

$$\nabla\cdot\overline{\mathbf{U}} = 0; \quad \nabla\cdot\mathbf{u}' = 0 \tag{3.39}$$

Now, if the Reynolds decomposition is introduced into the momentum conservation equation and averaged over time, then along with the results obtained for the continuity equation 3.39, the x component of this momentum equation becomes:

$$\begin{aligned}&\overline{U}\frac{\partial\overline{U}}{\partial x} + \overline{V}\frac{\partial\overline{U}}{\partial y} + \overline{W}\frac{\partial\overline{U}}{\partial z} + \frac{\partial\overline{u'u'}}{\partial x} + \frac{\partial\overline{u'v'}}{\partial y} + \frac{\partial\overline{u'w'}}{\partial z}\\ &= -\nabla\bar{p} + \frac{1}{\mathrm{Re}}\nabla^2\overline{U}\end{aligned} \tag{3.40}$$

Using Einstein's notation makes possible to include te three components x, y y z in one single equation:

$$\frac{\partial}{\partial x_j}\left(\overline{U}_i\overline{U}_j\right) = -\frac{\partial \bar{p}}{\partial x_i} - \frac{\partial}{\partial x_j}\tau_{ij} + \frac{1}{Re}\frac{\partial^2 \overline{U}_i}{\partial x_j \partial x_j} \tag{3.41}$$

Where τ_{ij} is the term containing all the mean products of the turbulent fluctuations:

$$\tau_{ij} = \overline{u_i u_j} - \bar{u}_i \bar{u}_j = \overline{u_i' u_j'} \tag{3.42}$$

This term is known as the Reynolds stress tensor because, by being added as an additional term on the right-hand side of the momentum conservation equation, it acts as a source term for the mean flow component, $\overline{\mathbf{U}}$. Physically, this implies that the mean flow components, $\overline{U}i$, are not independent of the turbulent fluctuations represented by the Reynolds stress tensor, τij [20]. Therefore, this mean component of a turbulent flow, $\overline{\mathbf{U}}$, cannot be obtained unless τ_{ij} is solved for or unless models for τ_{ij} are constructed in terms of $\overline{\mathbf{U}}$. Mathematically, this also means that in the system of equations for the mean flow components, there are more unknowns than equations, known as the closure problem of the Navier-Stokes equations.

The models proposed to express the turbulent fluctuations, τ_{ij}, in terms of the mean components, $\overline{U}_i$, are known as **closure models**. These models are included alongside the RANS equations to obtain a useful approximation of $\overline{\mathbf{U}}$. Each closure model is used according to the nature of the flow being approximated, as each of them has been constructed for the convenience of a specific type of flow [20].

One of the earliest closure models, known as the **Eddy viscosity model**, attempts to approximate the Reynolds stresses as if they behaved like a diffusive term, which diffuses the momentum of the turbulent flow proportionally to a turbulent viscosity, ν_t:

$$-\overline{u_i' u_j'} = \nu_\mathrm{t}\left(\frac{\partial \overline{U}_i}{\partial x_j} + \frac{\partial \overline{U}_j}{\partial x_i}\right) - \frac{2}{3}\delta_{ij}k \tag{3.43}$$

Where:

$$k = \frac{1}{2}\overline{u_i' u_i'} = \frac{1}{2}\left(\overline{u_x' u_x'} + \overline{u_y' u_y'} + \overline{u_z' u_z'}\right) \tag{3.44}$$

is the turbulent kinetic energy of the turbulent flow fluctuations, which is transmitted and distributed from large eddies to form smaller eddies within the scale of the inertial subrange.

In the simplest of cases, ν_t can be assumed to be a constant, but this approximation yields very inaccurate results. A more advanced model for flows near a solid wall, known as the **mixing length models**, is obtained by approximating ν_t using the Prandtl relationship:

$$\nu_t = \left|\frac{\partial \bar{U}}{\partial y}\right| \ell_m^2 \tag{3.45}$$

These two types of **eddy viscosity models** are still too crude to accurately model turbulent kinetic energy, k, and its dissipation, ε. Besides their simplicity and limited effectiveness, these approaches are theoretically incorrect as they disregard the anisotropy of the Reynolds stress tensor.

A second type of RANS models are the **two-equation models**, which, although they maintain the assumption of turbulent viscosity from Equation 3.43, are more comprehensive and sophisticated as they estimate ν_t as the product of a velocity and a length that characterize the turbulence of the flow:

$$\nu_T = u^*(\vec{x}, t)\ell(\vec{x}, t) \tag{3.46}$$

The first and most well-known of the two-equation models is the famous $\mathbf{k}-\varepsilon$ method, in which, in addition to using the assumption of turbulent viscosity, two conservation equations are constructed: one for the turbulent kinetic energy k associated with the characteristic velocity scale of the turbulent flow, and another for the dissipation of this energy irreversibly into internal energy, ε, associated with the length scale:

$$\nu_T = C_\mu \frac{k^2}{\varepsilon} \tag{3.47}$$

$$\begin{gathered}\frac{\partial(\rho k)}{\partial t} + \frac{\partial\left(\rho \overline{U}_j k\right)}{\partial x_j} = \frac{\partial}{\partial x_j}\left(\mu \frac{\partial k}{\partial x_j}\right) - \frac{\partial}{\partial x_j}\left(\frac{\rho}{2}\overline{u'_j u'_i u'_i} + \overline{p' u'_j}\right) - \\ \rho \overline{u'_i u'_j} \frac{\partial \bar{u}_i}{\partial x_j} - \mu \overline{\frac{\partial u'_i}{\partial x_k} \frac{\partial u'_i}{\partial x_k}}.\end{gathered} \tag{3.48}$$

$$\frac{\partial(\rho\varepsilon)}{\partial t} + \frac{\partial\left(\rho u_j \varepsilon\right)}{\partial x_j} = C_{\varepsilon 1} P_k \frac{\varepsilon}{k} - \rho C_{\varepsilon 2} \frac{\varepsilon^2}{k} + \frac{\partial}{\partial x_j}\left(\frac{\mu_{\mathrm{t}}}{\sigma_\varepsilon} \frac{\partial \varepsilon}{\partial x_j}\right) \tag{3.49}$$

These last three equations, along with the Navier-Stokes equations, are feasible to implement in a computational numerical code and solve for many engineering problems, obtaining values for the mean flow components that can be used to calculate average values of other important engineering parameters such as average drag and lift forces or average drag coefficients, etc. The use of these models is not appropriate for cases where adverse pressure gradients cause flow separation at some point on the walls. In these cases, it has been found that this model does not represent the mean flow component well unless appropriate wall functions are used [21].

Another two-equation model known as $k-\omega$ also uses a transport equation for turbulent kinetic energy k somewhat different from that of the $k-\varepsilon$ model and a second transport equation for an inverse time scale: ω. In this model, we have that:

$$\omega = \frac{\varepsilon}{C_\mu \cdot k}; \quad \nu_t = \frac{k}{\omega}. \tag{3.50}$$

Unlike the $k-\varepsilon$ model, the $k-\omega$ model is suitable for use in boundary layers with significant pressure gradients, although it is not effective in accurately representing free-flow phenomena far from the walls. There is also another additional model, the $k-\omega$ SST (Shear-Stress Transport) model by Menter, which improves upon these two previous models by combining the advantages of the $k-\varepsilon$ model for modeling free flows and those of the $k-\omega$ model for modeling boundary layer flows. This provides a better prediction of a wide range of turbulent flows, especially in regions with adverse pressure gradients and boundary layer separation.

This approach works well for pseudo-steady problems in which the temporal mean component provides the most valuable information in an engineering problem. For non-steady problems, other approaches are used.

Unesteady Reynolds Averaged Navier Stokes Equations

To solve problems in which turbulent flow is non-stationary, two different methodologies are usually employed: using a local spatially averaged component or using an ensemble-averaged component. In both cases, this type of component does not make the temporal derivative of the averaged Navier-Stokes equations disappear. An ensemble average is defined as:

$$\overline{\mathbf{U}}\left(\boldsymbol{x},t\right)=\lim_{N\to\infty}\frac{1}{N}\sum_{1}^{N}\mathbf{u}^{n}\left(\boldsymbol{x},t\right)dt \tag{3.51}$$

Where $\mathbf{u}^n$ is a sample of the value of $\mathbf{u}$ taken in the nth experiment conducted under the same conditions. With this definition of ensemble average, a new Reynolds decomposition is defined:

$$\mathbf{u}(\boldsymbol{x},t)=\overline{\mathbf{U}}(\boldsymbol{x},t)+\mathbf{u}'(\boldsymbol{x},t) \tag{3.52}$$

Note that unlike the RANS approach, here the average component of the flow does depend on time and calculates a local average component of the flow. By introducing this Reynolds decomposition into the Navier-Stokes equations, the same models as in RANS are obtained but now including the temporal derivative, which allows advancing the solution in time in a non-stationary problem.

Large Eddy Simulations

The second most widely used approach to reduce the computational cost of a direct numerical simulation of the Navier-Stokes equations is known as Large Eddy Simulations (LES). In this approach, unlike the RANS approach, some of the turbulent flow fluctuations belonging to the subinertial range scales are numerically resolved. The goal is to resolve the larger scales, i.e., those with smaller wave numbers and therefore those that contain greater turbulent kinetic energy among all scales of the energy cascade. Since the transfer of energy between these larger scales occurs without dissipation, i.e., only through inertial mechanisms, then most of the transport of the variables conserved in a flow occurs in them. If these scales are resolved, then most of the transport of the conservative flow variables is correctly modeled, as the smaller scales contribute weakly to this type of transport [17].

Unlike the Direct Numerical Simulations (DNS) approach, in which all turbulent scales, including the smallest dissipative fluctuations of the energy cascade, are numerically resolved, in LES, these fluctuations are not resolved but instead modeled, as explained later and as illustrated in Figure 3.6.

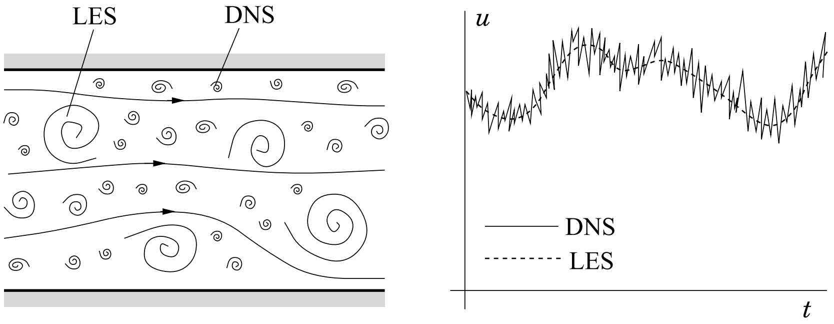

Figure 3.6: Schematic representation of the turbulent motion in a flow and the fluctuations captured by two different approaches (LES) and (DNS). Tomado de [17].

At each instant of a numerical simulation with the LES approach, the turbulent scales are computed through a local spatial average, which is obtained by applying a low-pass spatial filter that captures fluctuations with lower wave numbers. Just as in RANS, a temporal average was used to define the temporal average component, here in LES, spatial filtering is used to define a local spatial average component, which captures the largest turbulent fluctuations of the flow. This can be seen in the filtering of velocity [17]:

$$\bar{u}_i\left(x_i, t\right) = \int_{\Omega} G\left(x_i, x_i', \Delta\right) u_i\left(x_i', t\right) dx_i' \tag{3.53}$$

Where G is the kernel that defines the filter, which is represented by a Gaussian, a box filter (local average), and a cutoff frequency [17]. And where: Δ, is the length scale associated with the size of the filter used. Note that this local spatial average component does depend on time, as it is not averaging over time but over space, then, the bar accent over thar variables does not mean a temporal average as in RANS but a local spatial average. When using this filtering operation on the Navier-Stokes equations in incompressible flow, the continuity equation and momentum conservation equation remain as:

$$\frac{\partial\left(\bar{u}_i\right)}{\partial x_i} = 0 \tag{3.54}$$

$$\frac{\partial\left(\rho \bar{u}_i\right)}{\partial t} + \frac{\partial\left(\rho \overline{u_i u_j}\right)}{\partial x_j} = -\frac{\partial \bar{p}}{\partial x_i} + \frac{\partial}{\partial x_j}\left[\mu\left(\frac{\partial \bar{u}_i}{\partial x_j} + \frac{\partial \bar{u}_j}{\partial x_i}\right)\right] \tag{3.55}$$

In the momentum equation, the term containing $\overline{u_i u_j}$ can be observed, which is difficult to model, and furthermore, due to the definition of the filter, we have that:

$$\overline{u_i u_j} \neq \bar{u}_i \bar{u}_j \tag{3.56}$$

So, in the LES approach, similarly to the RANS approach, models are proposed for $\overline{u_i u_j}$ in terms of the components resolved by this approach, the filtered components: $\bar{u}\bar{u}_j$. This model calculates the difference between these two terms:

$$\tau_{ij}^{\mathrm{s}} = -\rho\left(\overline{u_i u_j} - \bar{u}_i \bar{u}_j\right) \tag{3.57}$$

Introducing this term in the momentum equation gives:

$$\frac{\partial\left(\rho \bar{u}_i\right)}{\partial t} + \frac{\partial\left(\rho \bar{u}_i \bar{u}_j\right)}{\partial x_j} = \frac{\partial \tau_{ij}^{\mathrm{s}}}{\partial x_j} - \frac{\partial \bar{p}}{\partial x_i} + \frac{\partial}{\partial x_j}\left[\mu\left(\frac{\partial \bar{u}_i}{\partial x_j} + \frac{\partial \bar{u}_j}{\partial x_i}\right)\right] \tag{3.58}$$

If it is ensured that the mesh size of the simulation h satisfies $\Delta \geq h$, then the smaller scales are being filtered out and the larger scales that are above the mesh size are being resolved. Then, the scales that are not resolved exert a volumetric force on the scales that are resolved, and this force is included in the momentum conservation in the term containing τ_{ij}^{s}. This is why τ_{ij}^{s} is known as the subgrid-scale Reynolds stress. To model τ_{ij}^{s}, various approximations can be used, but the oldest and most common one is known as the **Smagorinsky model**, which again uses the hypothesis of turbulent viscosity:

$$\tau_{ij}^{\mathrm{s}} - \frac{1}{3}\tau_{kk}^{\mathrm{s}}\delta_{ij} = \mu_{\mathrm{t}}\left(\frac{\partial \bar{u}_i}{\partial x_j} + \frac{\partial \bar{u}_j}{\partial x_i}\right) = 2\mu_{\mathrm{t}}\bar{S}_{ij} \tag{3.59}$$

where μ_{t} is the eddy viscosity and $\bar{S}_{ij}$ is the strain rate of the large scale or resolved field. Turbulent viscosity is given by:

$$\mu_{\mathrm{t}} = C_{\mathrm{S}}^2 \rho \Delta^2 |\bar{S}| \tag{3.60}$$

where C_{S} is a model parameter to be determined, Δ is the filter length scale, and $|\bar{S}| = \left(\bar{S}ij\bar{S}ij\right)^{1/2}$.

3.4.4 Mesh quality in LES simulations

LES models separate resolved turbulent scales from modeled scales using a filter associated with the cell size of the mesh. Therefore, it may happen that in a simulation, LES models are used with the Navier-Stokes equations filtered over a mesh, but this mesh has cell sizes that only allow very few of the larger turbulent scales to be resolved. In this case, even though mathematically filtered equations are being used, the mesh is not suitable for resolving the larger turbulence scales. As CFD techniques have begun to implement LES models, reliable quality assessment methods are required to ensure good resolution of the large turbulent scales and obtain accurate LES predictions. Several authors have attempted to establish quality indices based on numerical accuracy and models to assess the reliability of a specific LES simulation. In the present work, as in [8], simple algebraic criteria proposed by [22] are used.

Mesh quality index based on turbulent resolution (IQ_k)

This criterion was first conceptually described by [23], in which it is proposed to define a tolerance for the proportion of resolved turbulence with respect to the total turbulence of the problem. That is, it should be defined what proportion of the total turbulence of the problem k_{tot} is modeled by the SGS vs a tolerance ϵ_M: For example, if $\epsilon_M = 0.2$, then this means that 80% of the turbulence should be resolved by the filtered equations and the mesh, and the remaining 20% should be modeled by the SGS models. Since turbulence can occur at different scales in each flow region, the proportion given by ϵ_M must be fulfilled throughout the domain, and therefore, if there is a variable mesh size $h(x)$, then $\epsilon_M(x)$. In [22], it is proposed that $IQ_k(x) = 1 - \epsilon_M(x)$ can be calculated to determine the proportion of turbulence resolved by the model in terms of turbulent kinetic energy.

$$IQ_k(x) = \frac{k_{res}(x)}{k_{tot}(x)} = \frac{k_{res}(x)}{k_{res}(x) + k_{sgs}(x)} \tag{3.61}$$

Wher:

$$k_{res} = \frac{1}{2}\tilde{u}'_{RMS} \cdot \tilde{u}'_{RMS} = \frac{1}{2}\left(\tilde{u}'^2_{x,RMS} + \tilde{u}'^2_{y,RMS} + \tilde{u}'^2_{z,RMS}\right) \tag{3.62}$$

And $\tilde{u}'_{RMS} = \sqrt{\langle \tilde{u}\tilde{u} \rangle - \langle \tilde{u} \rangle^2}$ is calculated in terms of the resolved instantaneous velocity vector $\widetilde{u}$ and its time-averaged value noted $\langle \tilde{u} \rangle$, and where:

$$k_{sgs} = \frac{1}{(C_m \Delta_e)^2} \nu_{sgs}^2 \tag{3.63}$$

is the kinetic energy of the turbulent fluctuations modeled by the SGS and is directly related to the square of the viscosity of the SGS models: ν_{sgs}, Δ_e is the filter width, equal to the characteristic length of the grid cell and:

$$C_m = \sqrt{\frac{2}{3}} \cdot \frac{A}{\pi \cdot K_0^{2/3}}, \tag{3.64}$$

Is a constant where the coefficient $K_0 = 1.4$ corresponds to an infinite inertial spectrum for a Homogeneous Isotropic Turbulence for which the constant A is evaluated as $A = 0.44$ in the Eddy-Damped Quasi-Normal Markovian (EDQNM) theory [22]. In [18] t is stated that a good LES simulation is one in which at least 80% of the turbulent kinetic energy is resolved. Therefore, an index $IQ_k(x) \geq 0.8$ indicates that the larger turbulent scales are being resolved with good fidelity.

Mesh quality index based on viscosity (IQ_ν)

In this criterion, the contribution of the mixture viscosity ν, the viscosity calculated by the SGS ν_{SGS}, and the numerical viscosity ν_{num} are evaluated:

$$IQ_\nu = \frac{1}{1 + \alpha_\nu \cdot \left(\frac{\nu_{sgs} + \nu + \nu_{\text{num}}}{\nu} \right)^n} \tag{3.65}$$

Where:

- α_ν and n are two calibrated constants obtained from DNS simulations [24], with values $\alpha_\nu = 0.05$ and $n = 0.53$.
- ν is the molecular viscosity of the mixture representation of a two phase flow (liquid - gas), obtained from the viscosities of gas (ν_g) and liquid (ν_l), weighted by their volumetric fraction (α), this last quantity is explained conceptually in section 3.5.3.

$$\nu = \alpha_l \cdot \nu_l + \alpha_g \cdot \nu_g = \alpha_l \cdot \nu_l + (1 - \alpha_l) \cdot \nu_g \tag{3.66}$$

- ν_{num} is the numerical viscosity, which is assumed to be equal to the SGS viscosity ($\nu_{\text{num}} = \nu_{SGS}$).

For this criterion, the range that ensures good LES mesh quality is $0.5 < IQ_\nu < 1$ [8].

3.4.5 Turbulet boundary layer and wall treatments

As mentioned earlier, a solid wall in contact with a flow is a significant source of vorticity and therefore promotes the formation of turbulent flows. This production of vorticity and turbulent fluctuations is mainly due to the high shear stresses generated in the areas near the walls, which in turn lead to significant velocity gradients. This region of the flow, close to the walls where this occurs, is known as the boundary layer, and when these shear stresses and velocity gradients generate turbulent flow, this region is referred to as the turbulent boundary layer.

In a computational simulation aiming to accurately and effectively model the turbulent behavior of flow in the near-wall region, it's crucial to approximate the velocity field well in this area. This is because calculating the shear stresses that promote turbulent fluctuations requires computing the velocity gradient normal to the wall.

$$\tau = -\mu \frac{\partial u}{\partial y} \tag{3.67}$$

Law of the wall

In 1930, Theodore von Kármán developed a theory that correlates the mean velocity parallel to the wall of a turbulent flow with the distance from the flow to the wall. This means that this model allows for modeling the mean velocity profile in the near-wall region. This theoretical law is very useful in computational models where numerically modeling this velocity profile is complicated, such as in the $k - \epsilon$ model in the RANS approach or simply in cases where the spatial discretization of the domain into cells is not fine enough to capture velocity gradients.

This theory applies to fully developed turbulent flow near a straight wall; therefore, its use for estimating velocity profiles normal to the wall is appropriate as long as the flow is represented by such a flow. This law uses the dimensionless quantities u^+ and y^+, where:

$$u^+ \equiv \frac{\langle U \rangle}{u_\tau}; \quad y^+ = \frac{y u_\tau}{\nu}; \quad u_\tau = \sqrt{\frac{\tau_w}{\rho}}. \tag{3.68}$$

The term τ_w represents the wall shear stress, which is determined by both the flow properties and those of the wall. This law allows for distinguishing each zone of turbulent boundary layer formation. It is known that in a developed turbulent boundary layer, several zones can be identified where the flow exhibits different behaviors, and momentum transport phenomena and velocity profile variation occur differently. This can be observed in Figure 3.7, and each of these zones is approximated by the law of the wall, which can be constructed as a piecewise function, as shown in Figure 3.8.

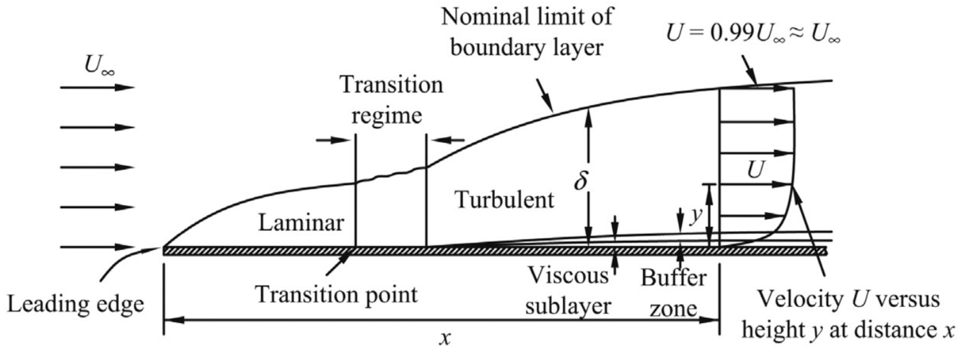

Figure 3.7: Schematic representation of the grow of the turbulent boundary layer along a flat plate. Tomado de [25].

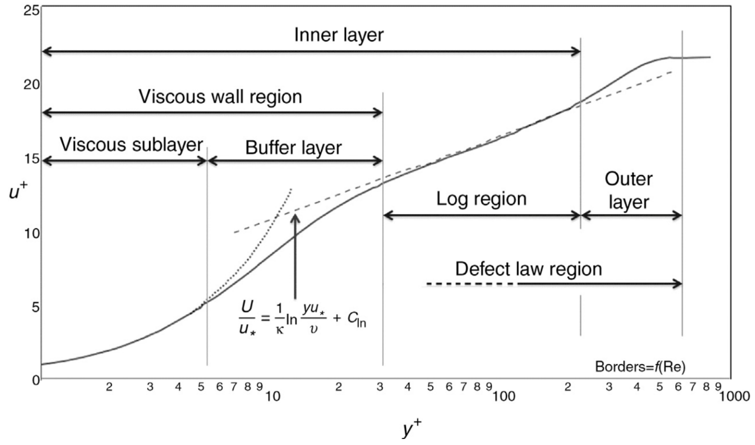

Figure 3.8: Subdivisions of the Near-Wall Region Curve. Tomado de [25].

The first subdivision closest to the wall within the boundary layer zone is known as the **viscous sublayer**. Here, the fluid viscosity dominates the flow behavior, resulting in an inevitably laminar flow since it is static at the wall, and the velocity increases linearly from zero at the wall to a maximum velocity. The velocity gradient is high, and strong friction occurs between fluid particles and the wall. Turbulence is minimal or absent in this region. This initial part of the velocity profile is approximated by the law of the wall as in the equation 3.69.

$$u^+ = y^+ \tag{3.69}$$

The next zone closest to the wall, after the viscous sublayer, is known as the **buffer layer**. This zone serves as a transition region where viscous effects are still significant, but turbulence begins to dominate the flow behavior. As the fluid velocity increases rapidly to a significant fraction of the free stream velocity, turbulence starts to develop and increases in intensity. This zone is well modeled by the wall function developed by Spalding as shown in the Figure 3.9.

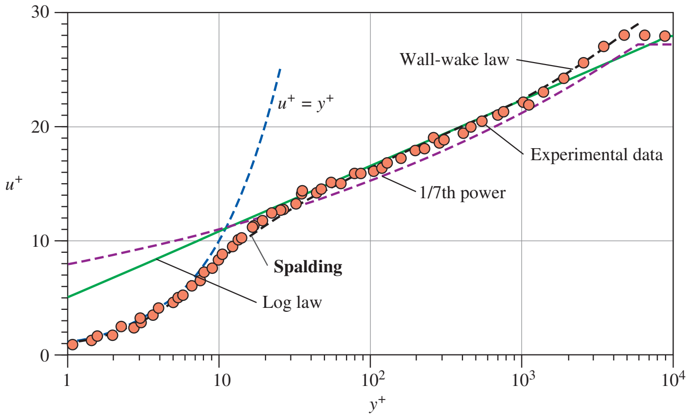

Figure 3.9: Wall functions representation. Tomado de [26].

The next zone after the buffer layer is known as the logarithmic layer. In this region, the fluid velocity increases logarithmically with respect to the distance from the wall until it stabilizes and approaches the characteristic logarithmic velocity profile of turbulent flow. Turbulence is prominent in this zone, and turbulent eddies develop and detach from the solid wall. Here, viscous effects no longer dominate the flow behavior, and turbulence becomes the primary driving force.

Wall functions

The computational effort required to calculate the velocity profile near the wall in a turbulent boundary layer can be substantially reduced if the first computational point can be located within the logarithmic range instead of in the viscous sublayer. We need the velocity gradient at the wall to compute the wall shear stress, but it cannot be accurately obtained from higher-order polynomials, as in the case of laminar flow. However, from the logarithmic law and some other assumptions, it is possible to derive a relationship between the wall shear stress and the velocity at a point in the logarithmic region of the profile. This is what wall functions accomplish.

En practical CFD applications, where the spatial points of the computational domain remain close to the wall within the viscous sublayer at all times, this is referred to as 'low Re wall treatment'. This treatment is more computationally expensive because it requires the mesh to be structured into very thin layers near the wall with a growing rate that captures these high gradients. In simulations where the first discrete points of the domain closest to the wall fall within the logarithmic range, wall functions are used to estimate the velocity profile normal to the wall and the wall shear stresses. This approach is known as 'high Re wall functions' [17].

The wall functions, in addition to assuming that the velocity profile behaves logarithmically, make two additional assumptions about the flow in that region.

- It is assumed that the flow is in local equilibrium, which means that turbulence production and dissipation are nearly equal.
- The total shear stress (i.e., the sum of the viscous and turbulent contributions) is constant between the wall and the first computational point and is equal to the wall shear stress τ_{wall}.

The presence of flow separation, stagnation zones, and reattachment zones inevitably leads to a large variation in wall shear stress, with places where it practically becomes zero. The assumptions upon which wall functions are based may not hold, or computational points may locally fall outside the viscous sublayer. Therefore, many researchers have attempted to develop more general versions of wall boundary conditions for turbulent flows.

These wall functions are used in computational models where it is convenient to save computational cost and avoid boundary layer structures in the mesh that attempt to numerically solve the velocity profile of the boundary layer. To use them, it is always advisable to first calculate the value of y^+ for all the cell centroids that are adjacent to the solid walls of the computational domain. This way, it can be determined whether the mesh to be used has its first discrete nodes in the viscous sublayer, the buffer layer, or the logarithmic layer. Thus, if these nodes closest to the walls have y^+ values such that they are in the viscous sublayer, then this means that the mesh near the wall is fine enough to numerically approximate the velocity profile. Conversely, if for these same points $y^+ \geq 30$, then it is preferable to use wall functions [17].

3.5 Multiphase flow modelling

Multiphase flow is discussed when there is flow of more than one phase, which coexist and interact within the same flow domain. A phase is one of the forms in which matter coexists and flows within a multiphase flow. A phase flows in a *continuous* form when it occupies a continuously connected region in space, or in a *dispersed* form when it occupies several regions disconnected from each other within the same domain. This type of flow occurs in many everyday situations and in numerous engineering applications, leading to various classifications and descriptions of multiphase flows. For instance, multiphase flows can be classified based on the state of the coexisting substances, such as solid-liquid flow, liquid-gas flow, gas-solid flow, etc. They can also be classified by the number of substances coexisting in the same flow domain: single-phase flow, two-phase flow, etc. Another common approach is to classify them according to the type of phase interaction: continuous phases or dispersed phases.

In computational numerical modeling, multiphase flow models are classified based on the type of interacting phases and the behavior of the interface between the phases. The two main types of models are the Euler-Euler models and the Euler-Lagrange models.

3.5.1 Euler Lagrange Models

Euler-Lagrange models are used in flows where it is necessary to track the position of each fluid particle of the interface or the position of each particle constituting one of the phases present in the flow. When one phase is dispersed and behaves like a collection of particles moving and affecting the flow of a continuous phase, the flow of this particle collection can be described by kinematically and dynamically tracking each individual particle. This involves describing the particle dynamics by following its trajectory. The equations of motion for each particle must be coupled with the Eulerian equations of the continuous phase through source or sink terms in the conservation principles [27]. In this way, the coupled interaction of the particles with the continuous phase flow can be described by adequately depicting the acceleration and movement of each particle to show how this affects the flow and vice versa

On the other hand, a Lagrangian tracking of the interface means that the interface is explicitly tracked on a fixed mesh by marking the interface with a set of connected particles of negligible mass. By assigning a sufficient number of markers on the interface, these markers move according to the local advection velocity field. During the calculation, the positions or Lagrangian coordinates of each marker can be obtained by numerical integration from some initial position.

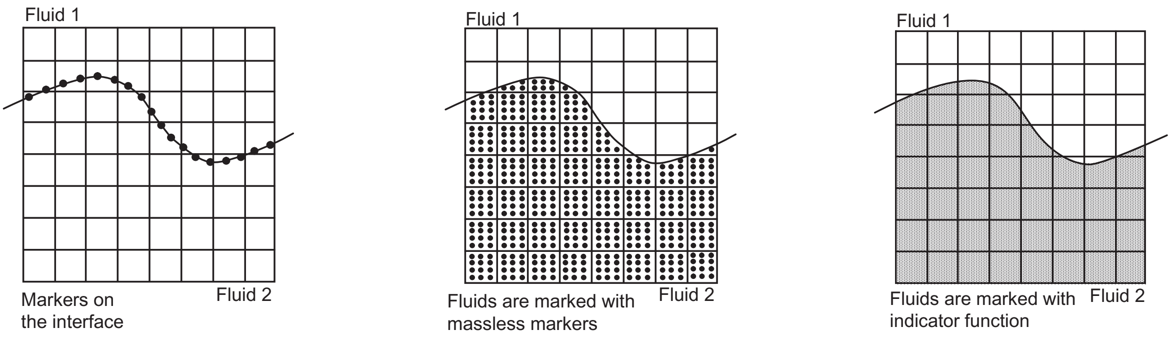

(a) (b) (c)

Figure 3.10: Different methods of representing the behaviour of immiscible fluid separated by an interface. Tomado de [27].

3.5.2 Euler Euler Models

This type of model is implemented in flows where the phases are continuous and it is easier to describe the continuum using the Eulerian approach. Thus, the conservation principles of mass and momentum for a phase k can be written using effective equations that describe the conservation of the averaged components of the fields. In this way, the conservation principles can be expressed in terms of the local volume fraction and the products of averages [27]:

Mass conservation

$$\frac{\partial\left(\alpha^k\rho^k\right)}{\partial t}+\nabla\cdot\left(\alpha^k\rho^k\mathbf{U}^k\right)=\Gamma'^k \tag{3.70}$$

In this continuity equation, the scalar α^k corresponds to the scalar field of the volume fraction of phase k:

$$\alpha^k(x,y,z,t)=\frac{V^k(x,y,z,t)}{V(x,y,z,t)} \tag{3.71}$$

which is the ratio of the fractional volume V_k of the k-th phase in a small arbitrary region to the total volume V of the region in question. The term Γ'^k ensures that the total derivative is not equal to zero, as it corresponds to the source or sink term of phase k due to possible mass transfer of k caused by the presence of the interface. The magnitude of this mass transfer, Γ'^k, depends on the velocity difference between phase k and the interface, as well as the gradient of the volume fraction of phase k.

Momentum conservation

Momentum conservation equation for phase k is:

$$\begin{aligned}\frac{\partial\left(\alpha^k\rho^k\mathbf{U}^k\right)}{\partial t}+\nabla\cdot\left(\alpha^k\rho^k\mathbf{U}^k\times\mathbf{U}^k\right)&=-\alpha^k\nabla p^k-p^k\nabla\alpha^k\\&+\nabla\cdot\left(\alpha^k\tau^k\right)-\nabla\cdot\left(\alpha^k\boldsymbol{\tau}^{k\prime\prime}\right)+\alpha^k\sum\mathbf{F}^{k,\text{ body forces}}+\Omega'^k\end{aligned}\tag{3.72}$$

In this equation, in addition to the momentum sources due to surface forces and body forces, there is an additional term (Ω'^k), which contains the momentum sources or sinks due to the presence and movement of the interface. Its magnitude is also a function of the velocity difference between phase k and the interface. It also incorporates stresses due to drag and pressure forces across the interface.

When equations 3.70 and 3.72 are used in the modeling of multiphase flow, it is said that the *multifluid model* is being employed, which involves applying conservation principles to each of the phases individually. This increases computational cost since it solves all fields for each of the phases.

Mixture models

These models aim to reduce the cost and number of calculations of the *multifluid model* and simplify the problem by considering the multiphase flow phases as a single phase: the mixture. Conservation principles are applied to this new and single phase throughout the domain, and interface terms described in Section 3.5.2 are included. These mixture models can be divided into two branches: mixture models for flows where the phases are miscible (resulting in a diffuse interface) and mixture models for immiscible phase flows, where models allowing for capturing the interface position are implemented, known as Interface Capturing Models (ICM). In this latter branch, there are different types of models, each using a different method to capture the interface.

Considering a flow of N phases, each conservation equation for the mixture arises from summing the N equations 3.70 of the conservation principle for each phase into a single conservation equation for the mixture. This is done separately for both the mass conservation equation and the momentum conservation equation 3.72. If these equations are combined in this manner, assuming Newtonian fluids and considering that this sum of equations nullifies the term $\Gamma'^k \equiv \sum_l$ and that $\sum_{k=1}^{N}\alpha^k = 1$, then the mass conservation equation for the mixture becomes:

$$\frac{\partial\rho^m}{\partial t}+\nabla\cdot\left(\rho^m\mathbf{U}^m\right)=0\tag{3.73}$$

Combinig the momentum conservation equations in a single equation for the mixture gives:

$$\begin{aligned}\frac{\partial\left(\rho^m\mathbf{U}^m\right)}{\partial t}+\nabla\cdot\left(\rho^m\mathbf{U}^m\times\mathbf{U}^m\right)=&-\nabla p+\nabla\cdot\left[\mu^m\left(\nabla\mathbf{U}^m\right)+\left(\nabla\mathbf{U}^m\right)\right.\\&\left.-\frac{2}{3}\mu^m\nabla\cdot\mathbf{U}^m\delta\right]-\nabla\cdot\boldsymbol{\tau}^{m\prime\prime}+\rho^m\mathbf{g}+\mathbf{F}_\sigma\\&-\nabla\cdot\sum_{k=1}^{N}\left(\alpha^k\rho^k\mathbf{U}^{dr,k}\times\mathbf{U}^{dr,k}\right)\end{aligned}\tag{3.74}$$

The properties of the mixture are evaluated as a weighted average of the properties of each of the phases, where α^k acts as the weighting factor.

$$\rho^m=\sum_{k=1}^{N}\alpha^k\rho^k,\quad \mu^m=\sum_{k=1}^{N}\alpha^k\mu^k\tag{3.75}$$

and the velocity field as:

$$\mathbf{U}^m=\frac{\sum_{k=1}^{N}\alpha^k\rho^k\mathbf{U}^k}{\sum_{k=1}^{N}\alpha^k\rho^k}\tag{3.76}$$

To complete this model, an equation is required to solve for the field α^k of each phase. This equation is obtained by using the mass conservation equation relative to each phase, solving $N-1$ conservation equations of the form:

$$\frac{\partial\left(\rho^k\alpha^k\right)}{\partial t}+\nabla\cdot\left(\rho^k\alpha^k\mathbf{U^k}\right)=\sum_{l=1}^{N}\left(\dot{m}_{lk}-\dot{m}_{kl}\right)\tag{3.77}$$

The model is closed by calculating the volume fraction of the remaining phase N with: $\sum_{k=1}^{N}\alpha^k=1$.

This model allows the phases to move with their own velocity field, thus there exists a relative velocity of each phase with respect to the mixture: $\mathbf{U}^{\mathrm{dr},k}$. Therefore, it is assumed that phase equilibrium is reached at small spatial scales. The drift or slip velocity $\mathbf{U}^{\mathrm{dr},k}$ is estimated using experimental correlations for each particular case.

3.5.3 The Volume of fluid approach

To model the two-phase flow in this study, the Volume of Fluid (VOF) approach is used. This approach originates from the mixture model, is adapted for two-phase flow, and incorporates an Interface Capturing Model (ICM) to capture the interface. The VOF method is suitable for modeling free surface flows, i.e., two-phase flows of immiscible liquid-gas phases with density ratios of up to $\rho^l/\rho^g\approx 1000$, where the liquid surface moves 'freely' within the gas atmosphere. These interfacial flows are mainly governed by hydrodynamic transport, as the gas and liquid phases are isothermal, incompressible, and undergo no phase change.

Given that incompressible and immiscible liquid-gas two-phase flow is being modeled, the equations of the mixture model are as follows:

Mass conservation equation:

$$\frac{\partial\rho^m}{\partial t}+\frac{\partial\left(\rho^m u^m\right)}{\partial x}+\frac{\partial\left(\rho^m v^m\right)}{\partial y}+\frac{\partial\left(\rho^m w^m\right)}{\partial z}=0\tag{3.78}$$

Momentum conservation equation, x component

$$\begin{aligned}\frac{\partial\left(\rho^m u^m\right)}{\partial t}&+\frac{\partial\left(\rho^m u^m u^m\right)}{\partial x}+\frac{\partial\left(\rho^m v^m u^m\right)}{\partial y}+\frac{\partial\left(\rho^m w^m u^m\right)}{\partial z}\\&=\frac{\partial}{\partial x}\left[\left(\mu^m+\mu_T^m\right)\frac{\partial u^m}{\partial x}\right]+\frac{\partial}{\partial y}\left[\left(\mu^m+\mu_T^m\right)\frac{\partial u^m}{\partial y}\right]\\&+\frac{\partial}{\partial z}\left[\left(\mu^m+\mu_T^m\right)\frac{\partial u^m}{\partial z}\right]+S_{u^m}\end{aligned}\tag{3.79}$$

Momentum conservation equation, y component

$$\begin{aligned}\frac{\partial\left(\rho^m v^m\right)}{\partial t}&+\frac{\partial\left(\rho^m u^m v^m\right)}{\partial x}+\frac{\partial\left(\rho^m v^m v^m\right)}{\partial y}+\frac{\partial\left(\rho^m w^m v^m\right)}{\partial z}\\&=\frac{\partial}{\partial x}\left[\left(\mu^m+\mu_T^m\right)\frac{\partial v^m}{\partial x}\right]+\frac{\partial}{\partial y}\left[\left(\mu^m+\mu_T^m\right)\frac{\partial v^m}{\partial y}\right]\\&+\frac{\partial}{\partial z}\left[\left(\mu^m+\mu_T^m\right)\frac{\partial v^m}{\partial z}\right]+S_{v^m}\end{aligned}\tag{3.80}$$

Momentum conservation equation, z component

$$\begin{aligned}\frac{\partial\left(\rho^m w^m\right)}{\partial t}&+\frac{\partial\left(\rho^m u^m w^m\right)}{\partial x}+\frac{\partial\left(\rho^m v^m w^m\right)}{\partial y}+\frac{\partial\left(\rho^m w^m w^m\right)}{\partial z}\\&=\frac{\partial}{\partial x}\left[\left(\mu^m+\mu_T^m\right)\frac{\partial w^m}{\partial x}\right]+\frac{\partial}{\partial y}\left[\left(\mu^m+\mu_T^m\right)\frac{\partial w^m}{\partial y}\right]\\&+\frac{\partial}{\partial z}\left[\left(\mu^m+\mu_T^m\right)\frac{\partial w^m}{\partial z}\right]+S_{w^m}\end{aligned}\tag{3.81}$$

Where the source terms in the momentum equation $S_{u_i{}^m}$ include the effects of buoyancy forces and surface tension forces:

$$\begin{aligned}S_{u^m}=&-\frac{\partial p''}{\partial x}+\frac{\partial}{\partial x}\left[\left(\mu^m+\mu_T^m\right)\frac{\partial u^m}{\partial x}\right]+\frac{\partial}{\partial y}\left[\left(\mu^m+\mu_T^m\right)\frac{\partial v^m}{\partial x}\right]\\&+\frac{\partial}{\partial z}\left[\left(\mu^m+\mu_T^m\right)\frac{\partial w^m}{\partial x}\right]+\left(\rho^m-\rho^{ref}\right)g_x+F_{\sigma,x}\\S_{v^m}=&-\frac{\partial p''}{\partial y}+\frac{\partial}{\partial x}\left[\left(\mu^m+\mu_T^m\right)\frac{\partial u^m}{\partial y}\right]+\frac{\partial}{\partial y}\left[\left(\mu^m+\mu_T^m\right)\frac{\partial v^m}{\partial y}\right]\\&+\frac{\partial}{\partial z}\left[\left(\mu^m+\mu_T^m\right)\frac{\partial w^m}{\partial y}\right]+\left(\rho^m-\rho^{ref}\right)g_y+F_{\sigma,y}\\S_{w^m}=&-\frac{\partial p''}{\partial z}+\frac{\partial}{\partial x}\left[\left(\mu^m+\mu_T^m\right)\frac{\partial u^m}{\partial z}\right]+\frac{\partial}{\partial y}\left[\left(\mu^m+\mu_T^m\right)\frac{\partial v^m}{\partial z}\right]\\&+\frac{\partial}{\partial z}\left[\left(\mu^m+\mu_T^m\right)\frac{\partial w^m}{\partial z}\right]+\left(\rho^m-\rho^{ref}\right)g_z+F_{\sigma,z}\end{aligned}\tag{3.82}$$

And $p\prime\prime$ is the modified average pressure, defined as:

$$p''=p+\frac{2}{3}\rho^m k^m+\frac{2}{3}\left(\mu^m+\mu_T^m\right)\nabla\cdot\mathbf{U}^m-\rho^{ref}g_i x_i\tag{3.83}$$

The VOF method, being a liquid-gas two-phase flow, includes within the mixture model the weighted equations that allow the evaluation of the mixture properties using only the volume fraction of the liquid, since that of the gas can be obtained from: $\alpha^l = 1 - \alpha^g$. Thus, the properties of the mixture are evaluated as:

$$\begin{aligned} \rho^m &= (1-\alpha^l)\rho^g + \alpha^l \rho^l \\ \mu^m &= (1-\alpha^l)\mu^g + \alpha^l \mu^l \end{aligned} \tag{3.84}$$

Since it is a two-phase mixture model, only one advection equation of the volume fraction field of one of the phases, that of the liquid, needs to be solved:

$$\frac{\partial \alpha^l}{\partial t} + \mathbf{u}^m \cdot \nabla \alpha^l = 0 \tag{3.85}$$

wich acn be expanded as:

$$\frac{\partial \alpha^l}{\partial t} + \frac{\partial \left(u^m \alpha^l\right)}{\partial x} + \frac{\partial \left(v^m \alpha^l\right)}{\partial y} + \frac{\partial \left(w^m \alpha^l\right)}{\partial z} = \alpha^l \left[\frac{\partial u^m}{\partial x} + \frac{\partial v^m}{\partial y} + \frac{\partial w^m}{\partial z}\right] \tag{3.86}$$

The form of this transport equation automatically ensures mass conservation in the model.

It should be noted that the main drawback of the VOF method is the lack of sharpness in the representation of the interface between the two study fluids. Therefore, if no additional interface capturing method is used, cells containing a portion of both fluids simultaneously will not have a sharp surface separating the volume fractions; instead, the entire cell will be filled with a uniform mixture of the two phases. Additionally, interface reconstruction is relevant for defining the normal vector used to calculate surface tension forces in the momentum conservation equation. These forces, according to the model known as Continuum Surface Force (CSF), can be calculated as:

$$\mathbf{F}_\sigma = \sigma\kappa\nabla\chi = \sigma\kappa\mathbf{n}_{\text{int}} \quad \rightarrow \quad F_{\sigma,x} = \sigma\kappa\frac{\partial \alpha}{\partial x} \quad F_{\sigma,y} = \sigma\kappa\frac{\partial \alpha}{\partial y} \quad F_{\sigma,z} = \sigma\kappa\frac{\partial \alpha}{\partial z} \tag{3.87}$$

Where:

- κ is the curvature of the surface defining the interface and it can be calculated as:

$$\kappa = -\nabla \cdot \widehat{\mathbf{n}}_{\text{int}} \quad \rightarrow \quad \kappa = \frac{1}{|\mathbf{n}_{\text{int}}|}\left[\left(\frac{\mathbf{n}_{\text{int}}}{|\mathbf{n}_{\text{int}}|} \cdot \nabla\right)|\mathbf{n}_{\text{int}}| - (\nabla \cdot \mathbf{n}_{\text{int}})\right] \tag{3.88}$$

- $\mathbf{n}_{\text{int}}$ is the normal vector to the surface defining the interface and is calculated as:

$$\mathbf{n}_{\text{int}} = \nabla \alpha \tag{3.89}$$

Therefore, to implement this model of surface tension forces, a geometric ICM is required that allows for the calculation of the normal vector to the interface surface and calculates the advective fluxes of α in the transport equation 3.85. In this way, by accurately estimating these fluxes in the cells where the interface is located, the shape of the interface can be predicted accurately, and therefore equations 3.89, 3.88, and 3.87 will have greater accuracy. It is also important that these numerical schemes approximating these fluxes are as least diffusive as possible.

3.5.4 Interface reconstruction scheme: isoAdvector

An important tool of the computational model used in this study is the numerical scheme employed for interface reconstruction. As mentioned earlier, dealing with a two-phase flow with a sharp interface, that is, with a clear and distinguishable interface (which in theory can be defined as a surface), it is required that the numerical scheme be capable of modeling as closely as possible the advancement of this interface while advancing the global solution. To achieve this, the movement of a surface is sought to be modeled through advective transport, minimizing numerical diffusion to the maximum extent possible.

In [28], an appropriate numerical scheme to solve this problem, known as the interface advection problem, is detailed. This scheme allows for the advancement of the surface defining the sharp interface at each step of the solution from a prescribed velocity field. This section summarizes the derivation and algorithm that define this interface reconstruction method.

Considering that this method is defined within the Eulerian VOF (Volume of Fluid) approach, the interface can be mathematically defined as a surface $\mathcal{S}$ that moves within the general flow domain: $\mathcal{D} \in \mathbb{R}^3$. This surface separates the two immiscible and incompressible fluids A and B, which respectively occupy the regions $\mathcal{A}$ and $\mathcal{B}$, such that $\mathcal{A} \cap \mathcal{B} = \mathcal{S}$ and $\mathcal{A} \cup \mathcal{B} = \mathcal{D}$.

This surface $\mathcal{S}$ is defined as the set of points where the density field of the mixture $\rho(\mathbf{x}, t)$ is discontinuous, as this field takes the value ρ_A in $\mathcal{A}$ or the value ρ_B in $\mathcal{B}$, and at the interface, it is immaterial. Thus, if the field $\rho(\mathbf{x}, t)$ is what defines $\mathcal{S}$, then advancing $\mathcal{S}$ requires advancing the solution of the continuity equation 3.73, which can be written in its integral form as:

$$\frac{\mathrm{d}}{\mathrm{d}t} \int_{\mathcal{V}} \rho(\mathbf{x}, t) \mathrm{d}V = - \int_{\partial \mathcal{V}} \rho(\mathbf{x}, t) \mathbf{u}(\mathbf{x}, t) \cdot \mathrm{d}\mathbf{S} \tag{3.90}$$

Where $\mathcal{V} \in \mathcal{D}$ is an arbitrary stationary volume, $\partial\mathcal{V}$ is its boundary, and $\mathrm{d}\mathbf{S}$ is the normal vector pointing outward from its surface.

To make the problem independent of ρ_A and ρ_B, a dimensionless phase indicator is used:

$$H(\mathbf{x}, t) \equiv \frac{\rho(\mathbf{x}, t) - \rho_B}{\rho_A - \rho_B} \tag{3.91}$$

such that: $H = 1$ for all $\mathbf{x} \in \mathcal{A}(t)$ and $H = 0$ for all $\mathbf{x} \in \mathcal{B}(t)$. If the domain is discretized into finite volumes, i.e., into a large number N_C of cells $\mathcal{C}_i$, with $i = 1, 2, \ldots, N_C$, then if two cells $\mathcal{C}_i$ and $\mathcal{C}_j$ are adjacent, this means they share boundaries on an internal face $\partial\mathcal{C}_i \cap \partial\mathcal{C}_j$, or if cell $\mathcal{C}_i$ touches the boundary of $\mathcal{D}$, then one or more faces of this cell are boundary cells. If all these faces of cell $\mathcal{C}_i$ are denoted as $\mathcal{F}_j$ with $j = 1, 2, \ldots, N_F$, where N_F is the number of faces of the cell, then Equation 3.90 can be written as:

$$\frac{\mathrm{d}}{\mathrm{d}t} \int_{\mathcal{C}_i} H(\mathbf{x}, t) \mathrm{d}V = - \sum_{j \in B_i} s_{ij} \int_{\mathcal{F}_j} H(\mathbf{x}, t) \mathbf{u}(\mathbf{x}, t) \cdot \mathrm{d}\mathbf{S} \tag{3.92}$$

Now, with $H(\mathbf{x}, t)$, the volumetric fraction field of fluid A can be written,

$$\alpha_i(t) \equiv \frac{1}{V_i} \int_{\mathcal{C}_i} H(\mathbf{x}, t) \mathrm{d}V \tag{3.93}$$

Introduciendo a α en la ecuación 3.91 e integrando en el intervalo $[t, t + \Delta t]$ se obtiene una ecuación que permite evaluar a $\alpha_i\,(t + \Delta t)$, es decir que permite avanzar la solución del campo de fracción volumétrica:

$$\alpha_i(t + \Delta t) = \alpha_i(t) - \frac{1}{V_i} \sum_{j \in B_i} s_{ij} \int_t^{t+\Delta t} \int_{\mathcal{F}_j} H(\mathbf{x}, \tau)\mathbf{u}(\mathbf{x}, \tau) \cdot \mathrm{d}\mathbf{S}\mathrm{d}\tau \tag{3.94}$$

Introducing α into Equation 3.94 and integrating over the interval $[t, t + \Delta t]$ yields an equation that allows evaluating $\alpha_i\,(t + \Delta t)$, meaning it allows advancing the solution of the volumetric fraction field.

$$\Delta V_j(t, \Delta t) \equiv \int_t^{t+\Delta t} \int_{\mathcal{F}_j} H(\mathbf{x}, \tau)\mathbf{u}(\mathbf{x}, \tau) \cdot \mathrm{d}\mathbf{S}\mathrm{d}\tau$$

So, if this term can be calculated, then the interface could be advanced at each time step. The issue is that this integral cannot be evaluated analytically, so one must leverage all the information from the numerical simulation available at time t to numerically approximate $\Delta V_j(t, \Delta t)$. To achieve this, the field of velocity averaged over the cell volume is utilized:

$$\mathbf{u}_i(t) \equiv \frac{1}{V_i} \int_{\mathcal{C}_i} \mathbf{u}(\mathbf{x}, t)\mathrm{d}V$$

and the convective flows through the cell faces:

$$\phi_j(t) \equiv \int_{\mathcal{F}_j} \mathbf{u}(\mathbf{x}, t) \cdot \mathrm{d}\mathbf{S}$$

The isoAdvector concept

There are two main concepts presented by Roenby [28], each of which describes the functioning of this interface reconstruction method. Each of these concepts is associated with one of the two numerical operations necessary to advance the interface during a timestep

Interface reconstruction step: The first of these concepts corresponds to how the algorithm constructs the part of the interface contained within a cell at time t. This surface is defined as an isosurface of the volumetric fraction field α. In other words, it's a surface within the cell $\mathcal{C}_i$ where all its points correspond to the same value of the field α.

This isosurface is constructed using the list of points that belong to the edges of cell $\mathcal{C}_i$ with a specific α value. In Figure 3.11, you can see a representation of this isosurface for a random cell $\mathcal{C}_i$ at a random α value. Note that constructing this isosurface requires a subgrid model that provides the α field values at the cell edges. This subgrid model interpolates the α field values at the cell vertices from the cell centers. From these interpolated values at the cell corners, the α values on the edges are determined, thus constructing this isosurface within cell $\mathcal{C}_i$. This part of the interface is a surface that will serve as a starting point to advance the interface over the interval Δt.

Note how this isosurface represented in Figure 3.11 divides the cell into two volumes, separating fluid A from fluid B. The subgrid model of the α field must ensure that the portion of the cell volume corresponding to fluid A remains adjacent to neighboring cells where $\alpha = 1$, and that the portion of the volume corresponding to fluid B remains adjacent to neighboring cells where $\alpha = 0$. This way, a sharp interface is constructed from the cells where $0 < \alpha < 1$. It should be noted that this way of reconstructing the interface within a cell only allows capturing interface structures with a radius of curvature greater than the cell size.

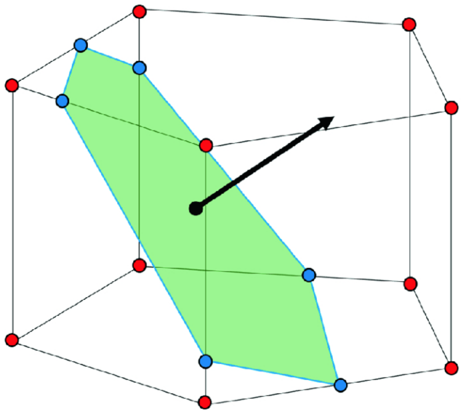

Figure 3.11: Isosurface defined for the same α isovalue using the subgrid model. Taken from [28]

An inconvenience of this method is that the surface defining the interface throughout the domain at a given time t (constructed from all internal isosurfaces of each cell) turns out to be discontinuous. This occurs because the isosurface constructed within a cell is made from a specific α isovalue for that cell. That is, this isovalue of α used for one cell, is not necessarily the same value used in an adjacent cell. In fact, for each cell, this value is chosen so that the volumes of fluid A and fluid B within the cell correspond to the value given by α_i at the cell's centroid. Therefore, it's possible that two contiguous cells have different α_i values at their centroids and, consequently, the isosurfaces dividing the cells into two volumes proportional to the value of α_i do not share edges. This leads to discontinuities in the surface defining the interface throughout the domain.

Interface advection step: The second concept associated with the second step of this interface reconstruction method is the way in which the term $\Delta V_j(t, \Delta t)$ is calculated. In this step, two numerical approximations are made to evaluate the double integral of $\Delta V_j(t, \Delta t)$:

- The first approximation consists of considering that the field $\mathbf{u}(\mathbf{x}, t)$ is constant during the interval $[t, t + \Delta t]$, meaning that $\mathbf{u}(\mathbf{x}, \tau) \approx \mathbf{u}(\mathbf{x}, t)$ throughout the interval.
- The second approximation involves changing the integrand:

  $$\mathbf{u}(\mathbf{x}, t) \cdot \mathrm{d}\mathbf{S}$$

  to another integrand:

  $$\mathbf{u}(\mathbf{x}, t) \cdot \mathrm{d}\mathbf{S} \approx \frac{\phi_j(t)}{|\mathbf{S}_j|} \mathrm{d}S \tag{3.95}$$

  Thus, the field $\mathbf{u}(\mathbf{x}, t)$ can be taken out of the integrals. This approximation can be interpreted physically as the fact that: a differential advective flux through face j: $\mathbf{u}(\mathbf{x}, t) \cdot \mathrm{d}\mathbf{S}$ can be approximated as the total advective flux $\phi_j(t)$ of face j divided by the norm of vector $\mathbf{S}_j$, and this ratio multiplied by $\mathrm{d}S \equiv \mathrm{d}|\mathbf{S}|$.

Then $\Delta V_j(t, \Delta t)$ remains as:

$$\Delta V_j(t, \Delta t) \approx \frac{\phi_j(t)}{|\mathbf{S}_j|} \int_t^{t+\Delta t} \int_{\mathcal{F}_j} H(\mathbf{x}, \tau) \mathrm{d}S \; \mathrm{d}\tau \tag{3.96}$$

Furthermore, the integral in $\mathcal{F}_j$ from previous equation, represents the surface portion of the face j that is submerged in fluid A

$$A_j(\tau) \equiv \int_{\mathcal{F}_j} H(\mathbf{x},\tau)\mathrm{d}S = \int_{\mathcal{F}_j \cap \mathcal{A}(\tau)} \mathrm{d}S \tag{3.97}$$

therefore:

$$\Delta V_j(t,\Delta t) \approx \frac{\phi_j(t)}{|\mathbf{S}_j|} \int_t^{t+\Delta t} A_j(\tau)\ \mathrm{d}\tau \tag{3.98}$$

It should be noted that equation 3.98 ceases to be an approximation and becomes an exact value when the velocity field is constant in time and space. Therefore, if one has a spatial discretization small enough compared to the velocity gradients and a small time step, then the error of this approximation is negligible.

Another approximation made by this method is that, since $A_j(\tau)$ can become a discontinuous function in $\tau \in [t, t+\Delta t]$, $A_j(\tau)$ is not properly used to calculate $\Delta V_j(t,\Delta t)$. Instead, to calculate the integral over Δt, the starting point is taken as the isosurface of the upwind cell at face j, and it is advanced using velocity information from neighboring cells during the time interval.

IsoAdvector's algorithm

Note that this method ultimately achieves numerical schemes that allow for the calculation of advective fluxes that transport the volumetric fraction field in the cells where the interface is located. In other words, these numerical schemes capture and advance the interface sharply. The steps this method takes at each time step of the global solution are:

- Step 1. For each face j, initialize ΔV_j with the upwind cell volume fraction, $\Delta V_j = \alpha_{\text{upwind }(j)}\phi_j\Delta t$.
- Step 2. Identify all cells containing the interface, i.e., cells with $\epsilon < \alpha_i(t) < 1-\epsilon$, where ϵ is a user-specified tolerance.
- Step 3. For each cell with a portion of the interface i, do the following:
    - Locate its isosurface within the cell with the alpha isovalue cutting the cell at the correct volumetric fractions, $\alpha_i(t)$ and $1-\alpha_i(t)$
    - Use velocity field data to estimate the isosurface movement during the time interval $[t, t+\Delta t]$
    - For each downstream face j of the cell with a portion of the interface i, use the isosurface and its movement to calculate the face-interface intersection line during the time interval $[t, t+\Delta t]$
    - For each downstream face j of the cell with a portion of the interface i, use the movement of its face-interface intersection line to calculate $\Delta V_j(t,\Delta t)$ from the time integral in Equation 3.98
- Step 4. For each cell, calculate $\alpha_i(t+\Delta t)$ by inserting the ΔV_j's of its faces into Equation 3.94.
- Step 5. For cells with $\alpha_i(t+\Delta t) < 0$ or $\alpha_i(t+\Delta t) > 1$, adjust the ΔV_j's of their faces using a redistribution procedure and recalculate $\alpha_i(t+\Delta t)$ by inserting corrected ΔV_j's into 3.94. This step also includes an optional clipping of any cell value $\alpha_i < 0$ or $\alpha_i > 1$ to ensure strict bounding before proceeding to the next time step.

3.6 Computational tools

In this section, the two main software tools that enabled this study are described. The first one is the CFD software used for simulations, and the second one is the software that facilitated most of the post-processing work.

3.6.1 OpenFOAM

The numerical computation software used in this study is OpenFOAM®. This software consists of a library of dictionaries built in C and C++ that allow for the numerical resolution of various types of continuum mechanics problems, such as fluid flow, single-phase or multiphase, heat transfer, as well as problems related to acoustic phenomena or mechanics of deformable solid bodies like structures. It was developed primarily by OpenCFD Ltd since 2004 [29] and is an open-access, open-source software that is continuously updated and improved.

The quality assurance in OpenFOAM® software is carried out through rigorous testing covering different levels of code evaluation. This includes hundreds of daily unit tests, a battery of medium-sized tests conducted weekly, and large-scale industry tests before each new version release. These tests are designed to evaluate crucial aspects such as regression behavior, memory usage, code performance, and scalability, thus ensuring the reliability and efficiency of the software.

As software that numerically solves physical problems in continuum mechanics, OpenFOAM® has two types of tools for discretizing these problems. Firstly, there are utilities, which are responsible for pre-processing the problem. This involves defining and structuring the problem in the discrete numerical domain. Utilities also handle post-processing, which means collecting and organizing the data obtained from the numerical solution. Secondly, there are solvers, which solve the discretized equations.

In this study, OpenFOAM® software is used to solve fluid flow problems. To solve such problems, OpenFOAM® employs the finite volume method (FVM) described earlier in Section 3.2. Configuring a specific case or problem to be solved using OpenFOAM® involves constructing a directory, within which three main directories must be defined (see Figure 3.12). The first of these main directories, the *0* directory, contains dictionaries defining the fields involved in describing the problem as well as their initial and boundary conditions. The second, *constant*, must first contain a set of dictionaries defining the values of the physical constants present in the problem and must also contain a subdirectory called *polymesh* within which all dictionaries and information defining the spatial domain discretization are located. The third main directory defining the case is the *system* directory. Within this third directory, all dictionaries that call and execute the OpenFOAM® applications required to numerically solve and store the information and data constituting the solution to the problem are selected. Within this third directory, there must always be at least three dictionaries defining the calculation and solution methodology of the problem:

- *ControlDict*: This file contains global control parameters for the simulation, such as the total simulation time, time step, boundary conditions, and other execution options.
- *fvSchemes*: Specifies the numerical schemes used to discretize different terms in the conservation equations applied in each of the discrete domains, such as advection, diffusion, and other differential operators.

- *fvSolution*: Contains the configuration of the numerical solvers that OpenFOAM will use to solve the discretized equations of the problem. It includes the selection of the solver, convergence-related parameters, and case-specific adjustments.

In addition to these files, this study includes files that define how the mesh is constructed: *blockMeshDict*, *snappyHexMeshDict*, *meshQualityDict*, and *surfaceFeaturesDict*. It also includes files that define the phases of the two-phase flow in the initial state: *setFieldsDict*, and the file that allows mapping a solution at a specific time to a new similar domain: *mapFieldsDict*.

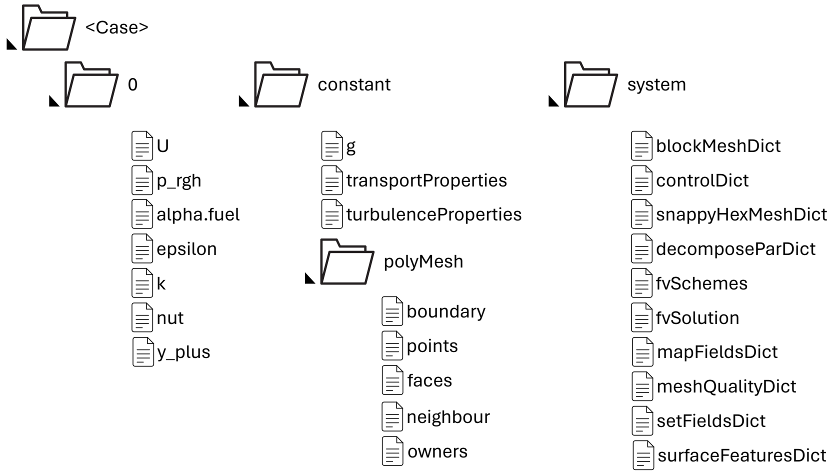

Figure 3.12: Files used to configure and set the case of study within the typical OpenFOAM® directories structure.

Once a case is defined in OpenFOAM®, and once the problem-solving process is initiated, OpenFOAM® will create new directories within the same general directory that defines the case. Each of these new directories contains the numerical solution of each of the fields being solved. If it is a non-steady-state problem, for which the fields within a time interval are to be solved, then the user can control the frequency at which a new directory with instantaneous solutions is generated and stored. If it is a steady-state problem, OpenFOAM® will solve the problem and can store these solutions until the user determines that a steady state has been reached.

3.6.2 Paraview

ParaView is a free and open-source 3D visualization and post-processing software for computational simulations that allows handling large datasets on both laptops and supercomputers. It is a project of the software company Kitware, which started in 2002 and has since then, in collaboration with other companies and scientific research institutions, continuously improved and released new versions twice a year. It has a graphical user interface and, being built in Python, has the ability to be customized to the user's convenience and automate many of its functions.

In the case of numerical simulations, ParaView allows for qualitative visualization of both the mesh used and scalar and vector fields on it. Additionally, it features a type of tool called *filters*, which enable the display of variables or streamlines and flow orientation over points, lines, surfaces, or volumes of interest. Moreover, these filters can be combined with each other to extract or calculate new variables from the data imported from the simulation. The latter can also be achieved by introducing user-defined equations to calculate new fields from the already imported ones. Among many other functions, ParaView also allows for the extraction and export of quantitative data in different formats, as well as generating XY dependency curves between flow variable values.

Chapter 4

Reference case study

4.1 Precedents

As mentioned in the introductory chapter, the study of this Master's Thesis is based on a functional computational model constructed by Alicia Muñoz Agulló [8]. This model uses a VOF (Volume of Fluid) approach within a LES (Large Eddy Simulations) frame models to simulate the biphasic flow of the primary atomization of n-heptane in a simplex atomizer and determines the best interface reconstruction scheme for these simulations. Both the study in [8] and this work are motivated by joint work with the French research center Complexe de Recherche Interprofessionnel en Aérothermochimie (CORIA), where multiple experiments were conducted using the CORIA Rouen Spray Burner with a pressure swirl type fuel injector. Tomography and laser techniques were used as optical diagnostic techniques for the formed flame and the fuel spray at the atomizer outlet. In [8], the spatial domain was modeled in CAD, using the injector geometry obtained through a combination of three different visualization techniques based on micrography.

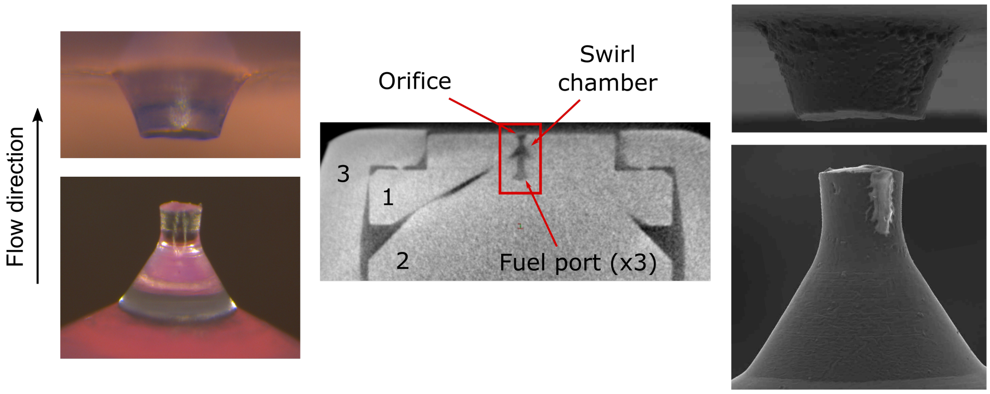

Figure 4.1: Images of a silicone model of the CORIA Rouen Spray Burner. Taken from [8].

As can be seen in Figure 4.1, this atomizer features a convergent swirl chamber and a throat just before the outlet orifice. The fuel enters the swirl chamber through three tangential inlet ports. The geometry of these features of the atomizer is shown in Figure 4.2, and their dimensions are provided in Table 4.1.

The computational model from [8] serves as an appropriate starting point for the parametric study of this Master's Thesis, as it determined both the mesh topology and the interface reconstruction scheme that best capture the fuel disintegration into droplets compared to previous

D_0 [μm]	D_{throat} [μm]	D_{swirl} [μm]	h_{swirl} [μm]	R_0 [μm]	R_t [μm]	Ψ_{throat} [°]	Ψ_{swirl} [°]	ϕ_{port} [°]
300	165	780	620	310	190	6	60	30

Table 4.1: Dimensions of the internal geometry of the CORIA Rouen Spray Burner.

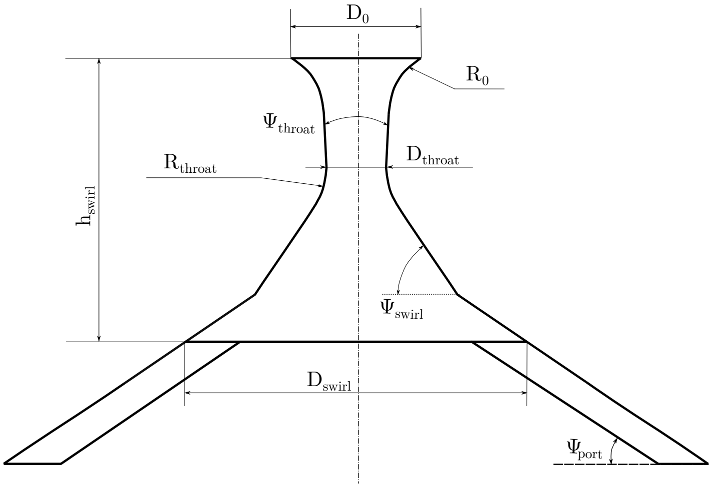

Figure 4.2: Diagram of the geometry and internal dimensions of the CORIA Rouen Spray Burner. Taken from [8].

studies. In Figure 4.3, three-dimensional contours representing the spray interface are shown based on an isovalue of the volume fraction field $\alpha_{\text{fuel}} = 0.5$. Each contour was obtained using different numerical interface reconstruction algorithms. Figures 4.3 and 4.4 illustrate how the IsoAdvector scheme achieves the most accurate and reliable capture of ligament and droplet formation from the liquid film when compared with photographs and experimental data.

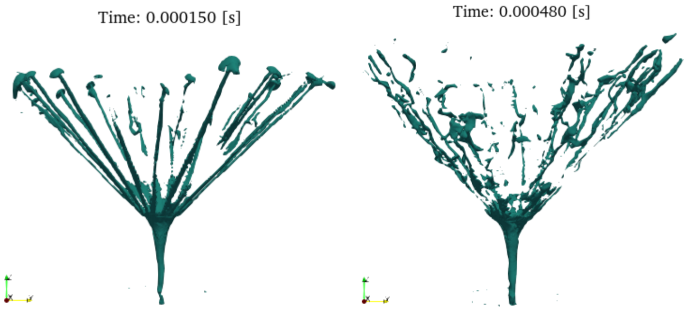

(a) 6M MULES

(b) 20M MULES

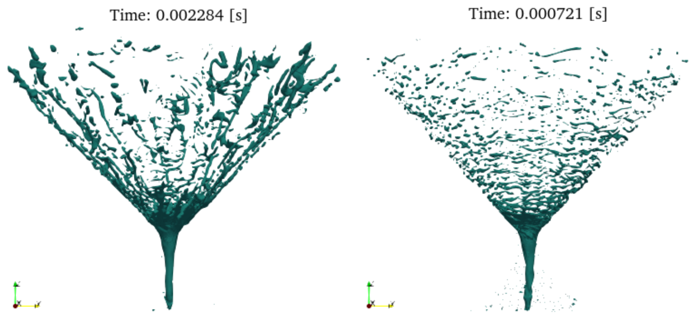

(c) 20M PLIC

(d) 20M isoAdvector

Figure 4.3: Interface representation with different interface reconstruction schemes used by [8].

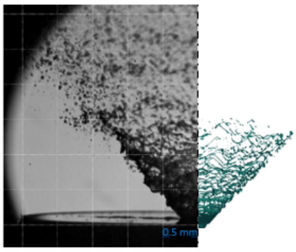

Figure 4.4: Comparison of the isosurface of the volume fraction of liquid $\alpha_{\mathrm{fuel}} = 0.5$ with experimental results [8].

The IsoAdvector interface reconstruction scheme allowed for capturing the formation of the air core and the oscillations of the free surface of the flow in this air core, which, upstream, will produce the unstable oscillations that propagate in the fuel film to break into ligaments and droplets. In Figure 4.5, contours of the volume fraction field for different simulations are shown. Each contour corresponds to an interface reconstruction scheme and is represented on a plane parallel to the symmetry axis of the hollow cone. These contours illustrate how the IsoAdvector scheme captures the air core with good definition, although it should be noted that the depth reached by this air core is more dependent on the mesh refinement than on the reconstruction scheme [8]. The oscillations on the free surface of the annular flow right at the outlet orifice, as captured, can be seen in more detail in Figure 4.6, where it is evident that they are much better captured by the IsoAdvector scheme.

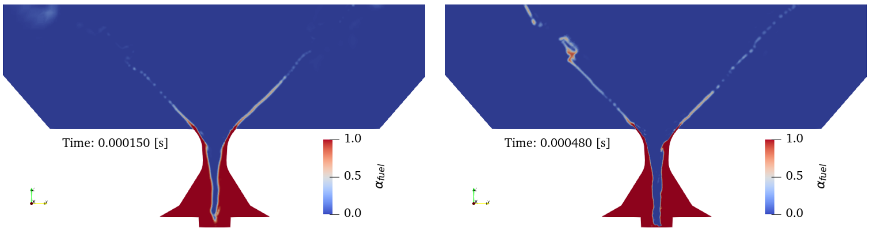

(a) 6M MULES (b) 20M MULES

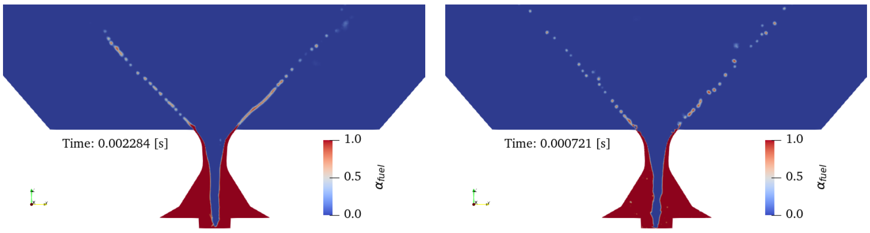

(c) 20M PLIC (d) 20M isoAdvector

Figure 4.5: Volume fraction field in the axisymmetric midplane captured with different interface reconstruction schemes used by [8].

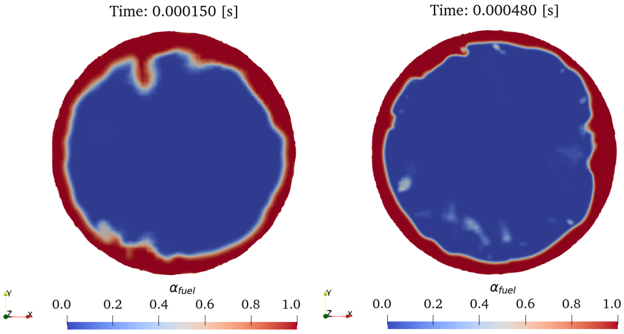

(a) 6M MULES (b) 20M MULES

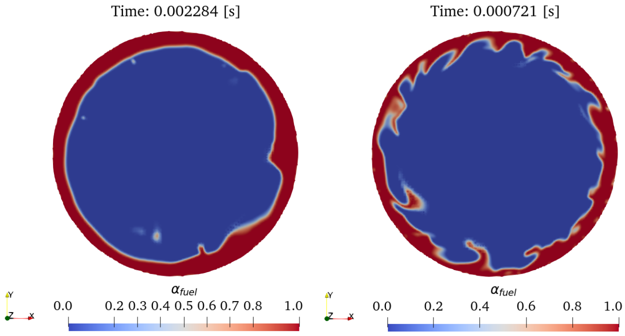

(c) 20M PLIC (d) 20M isoAdvector

Figure 4.6: Volume fraction field in the plane of the atomizer exit orifice captured with different interface reconstruction schemes. Taken from [8].

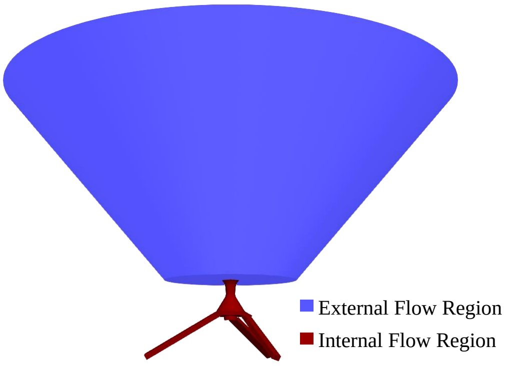

Figure 4.7: Regions of the computational domain in which the atomization of the present study occurs

4.2 Case configuration

In this section, a detailed description is provided on how the functional computational model constructed in [8] was used to conduct the mesh sensitivity study and the parametric study of this Master's Thesis. For this purpose, the strategies used in [8] that are employed in this study are outlined, as well as those that were adapted for the mesh sensitivity study 5 and the parametric study 6 described later.

4.2.1 Computational domain

The computational spatial domain of this study uses the internal geometry of the injector described in Figure 4.2 and Table 4.1, but also includes an external region where the atomization occurs. The three-dimensional model of the domain was constructed using CAD software, and from this CAD model, the discretized domain in finite volumes will be built using the meshing strategy described later. As described in [8] and shown in Figure 4.7, the spatial domain consists of two main regions: the internal flow region defined by the internal geometry of the injector's internal walls and the external flow region where the injector expels the liquid and atomization takes place.

La región del flujo interno, está compuesta por las distintas cavidades y conductos por los que pasa el combustible antes de ser expulsado a la atmósfera gaseosa. Las dimensiones que definen esta región están recopiladas en al tabla 4.1 y a continuación se describen la función de cada una de las características geométricas de esta región, la cuales se pueden ver en la figura 4.8. The internal flow region consists of the various cavities and ducts through which the fuel passes before being expelled into the gaseous atmosphere. The dimensions defining this region are compiled in Table 4.1, and the function of each geometric feature in this region is described below. These features can be seen in Figure 4.8.

1. Fuel injection channels. These consist of three prismatic bodies, each with a length of $L_{\text{slot}} = 1.5$ mm, attached to the lower part of the swirl chamber at an angle of $\phi = 40°$. Their cross-section corresponds to the liquid inlet area of the atomizer, with dimensions of $81 \times 139 \mu m$.

2. Cylinder. Located at the bottom of the atomizer, it stabilizes the air core formed during normal operation. This air core reaches the lower surface of the cylinder once a turbulent regime is established due to a sufficiently high Reynolds number.

3. Swirl chamber. This is a truncated cone designed to increase the tangential velocity of the liquid entering through the injection channels.

4. Spin chamber. This is a convergent section that further increases the tangential velocity of the injected fuel, generating an overpressure on the outer part of the atomizer. This results in the formation of a hollow cone-shaped fuel film and a central air core.

5. Throat and outlet section. These parts constitute the final section of the atomizer and lead to the outlet orifice through which the fuel film is discharged.

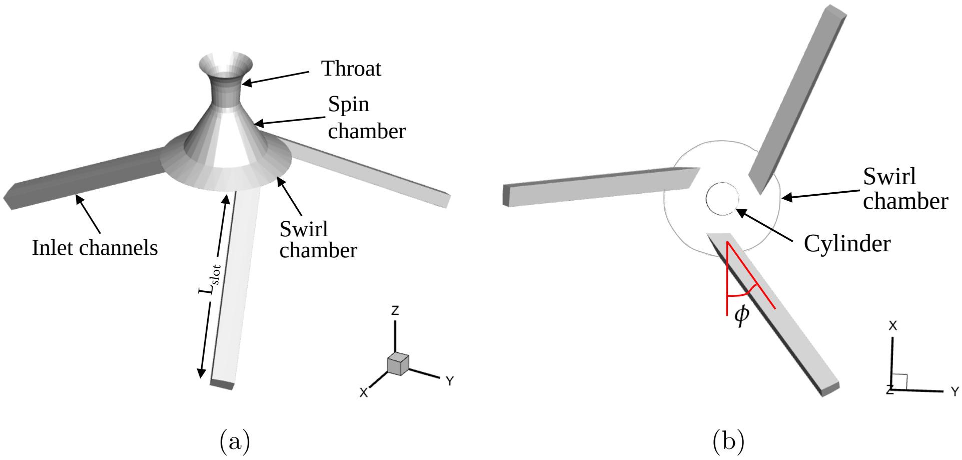

Figure 4.8: Regions through which the flow passes within the internal geometry of the CORIA Rouen Spray Burner. Adapted from [8].

The external flow region is modeled as a truncated cone, which intersects superficially with the internal region at the outlet orifice plane ($z = 0$) of the internal flow region. Its dimensions have been chosen to avoid boundary condition effects in regions of interest and to allow reliable comparison with experimental data. These dimensions are shown in Figure 4.9. The height of the truncated cone in the axial direction is 3.3 mm because the plane at 3 mm from the outlet orifice in the axial direction z is the first zone where experimental results are reliable. To prevent this zone from being affected by the outlet boundary condition, the length is extended by 10% of the 3 mm length, which is approximately 0.3 mm. The radius of the lower circle of the truncated cone is 1.15 mm, chosen so that the fuel film exiting the atomizer is always farther from the boundary surface than from the axial axis. Therefore, a distance of 1 mm from the outlet orifice radius, which is 0.15 mm, was selected.

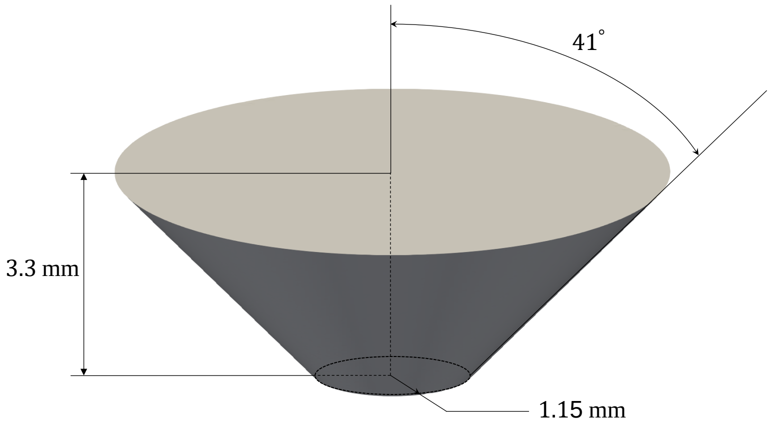

Figure 4.9: Dimensions defining the truncated cone of the external flow region.

The angle of the truncated cone is maintained as in [8]: at a value of 82°, which helps save computational cost by restricting the domain to an air region with a shape similar to the conical sheet of the spray. This value represents the maximum cone angle that the flow exiting this injector can reach.

4.2.2 Initial and boundary conditions

For this study, boundary conditions are applied to three types of boundaries: wall boundaries, outlet boundaries, and inlet boundaries. The boundary conditions for each unknown field are defined on these three types of boundaries, thereby fully defining the physical and mathematical model to be solved. Figure 4.10 shows the distribution of boundary types throughout the computational spatial domain, and they are described as follows:

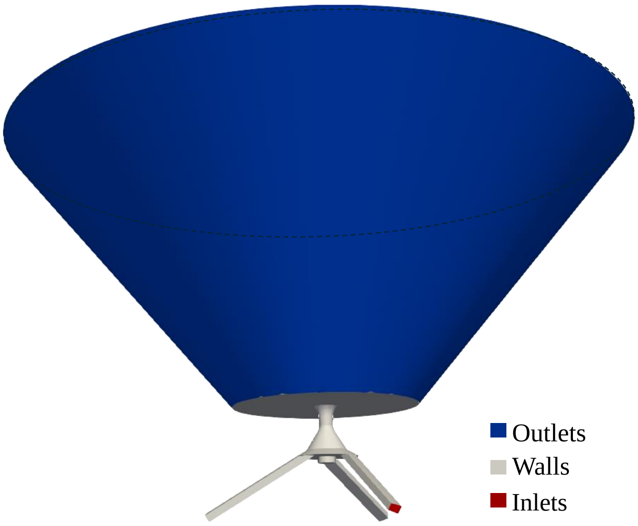

Figure 4.10: Types of borders on which specific boundary conditions are defined.

- **Inlets**: This type of boundary encompasses the three rectangular surfaces corresponding to the fuel inlet section into the computational domain, located at the lower ends of the three tangential inlet ports. At this type of boundary, a Dirichlet condition is defined for the velocity field and for the density and volume fraction fields, as a constant mass flow rate is specified with a uniform velocity profile in the normal direction to these faces. A zero-gradient condition is defined for the pressure field. The value of this total mass flow rate in the three tangential ducts is 0.28 g/s, as it corresponds to the experimental burner at CORIA Rouen Spray Burner [30]. The boundary conditions for the turbulence models on these and other surfaces are described later.

- **Wall**: This boundary type includes all surfaces defining the internal walls of the injector, the surfaces shaded in gray in Figure 4.10, and the circular surface contained in the plane where the internal and external flow regions intersect. This circular surface corresponds to the wall of the combustion chamber where the injector performs atomization and fuel burning. For all these surfaces modeling smooth solid surfaces, Dirichlet conditions are defined for the velocity field using the no-slip condition, allowing the development of the boundary layer. A zero Neumann condition is imposed for pressure, which, together with the Dirichlet condition, prevents any mass flow through these surfaces.
- **Outlet**: This boundary type includes the conical surface and the circle of the larger diameter of the truncated cone containing the external flow region. Crossed conditions of pressure and velocity are defined on these boundaries: Dirichlet for pressure, taking the total pressure value as constant, allowing the total pressure to adjust to the dynamic pressure given by the velocity. A zero Neumann condition is defined for velocity. Additionally, a non-return condition is defined for the liquid volume fraction field on these surfaces.

On the other hand, as described in [8], the initial conditions for the turbulent kinetic energy k and the dissipation rate (ε) used by the URANS $k-\varepsilon$ turbulence model, necessary for the characterization of turbulence, are also specified in the corresponding simulation files of OpenFOAM.

Subsequently, in the LES simulations, a new variable, the turbulent viscosity (v_t), is incorporated. These initial values of turbulent kinetic energy and dissipation rate are obtained from the rest of the boundary conditions. A turbulent intensity estimated at 5% of the mean flow velocity and a turbulent scale length of $l = 0.038 \cdot D_0$ are taken as the starting point, where D_0 is the characteristic diameter of the outlet orifice.

Additionally, it is worth noting the use of wall functions for the turbulent variables k, ε, and v_t as boundary conditions applied to the walls of the domain. The use of the wall functions *kqRWallFunction*, *epsilonWallFunction*, and *nutWallFunction* is related to the y^+ requirements, as discussed in Section 3.4.5.

Initial conditions are defined over the volumetric region comprising the entire flow domain (internal flow region and external flow region), except for the cell faces corresponding to the outer boundaries of the domain. This region is called the *InternalField* within the case constructed in OpenFOAM, and it defines the field values to establish the initial conditions for the simulations. All fields have uniform values throughout this region except for the volume fraction field, which is defined through a list where all points belonging to the internal region have a fuel volume fraction of $\alpha^{fuel} = 1$, meaning the injector at time $t = 0$ is already filled with liquid fuel, and the points belonging to the external region have $\alpha^{fuel} = 0$, indicating that at $t = 0$ the external region is filled with air.

From the initial conditions, the temporal advancement of the simulations employs the URANS turbulence approach to expedite the calculation of the transient period until the formation of the conical fuel film. Subsequently, the results of these URANS simulations are converted into initial fields for simulations using the LES turbulence approach. This process is carried out using a tool in OpenFOAM known as mapFields.

4.2.3 Meshing strategy

The mesh structure and type used in this study have been studied in the work of [8]. Therefore, in this subsection, only a brief description is provided of the types of geometries used for the finite volumes, the refinement zones in the domain, and the zones requiring special treatment of the boundary layer. The mesh used in this study must be refined enough to meet a series of main objectives:

- Resolve 80% of turbulent fluctuations in all zones of the domain, as it is an LES-type simulation.
- Accurately capture the breakup of the conical fuel sheet into ligaments and droplets.
- Achieve a sharp interface for the two present phases: air and fuel.
- Model shear stresses and velocity gradients where y^+ is very high for cells near solid walls.

For mesh construction, the OpenFOAM meshing tool *snappyHexMesh* was used, which initially creates a mesh of hexahedral elements throughout the domain and then cuts them to fit the curved surfaces of the domain. Therefore, the mesh may contain tetrahedral, prismatic, or polygonal elements.

It should also be noted that, for this study, a dynamic meshing method is used, meaning that the mesh is modified at each time step. Therefore, in each time step of the simulation, the same elements or faces are not present in certain zones of the domain, which increases computational cost but allows for better capture of liquid breakup or disintegration into droplets or ligaments. Specifically, the adaptive meshing method, Adaptive Mesh Refinement (AMR), is used based on the value of the fuel volume fraction α^{fuel} at each cell center. Thus, cells with volume fraction values between $0.3 \leq \alpha^{fuel} \leq 0.7$ (those likely to contain part of the interface) will be refined into smaller cells, so that in the next time step, the advancement of the interface can be more accurately captured in new cells of higher resolution.

For the entire domain, an initial base mesh size is defined, from which refinements will be made according to the refinement level in the OpenFOAM software. The *snappyHexMesh* tool allows the refinement level to be defined for each zone. The refinement regions to capture both the evolution of the conical film and the boundary layer on solid walls are described below:

- The main area where refinements are made is the region of the external flow domain, within this truncated cone certain zones are refined:
    - A volume defined by a conical shell is refined, within which the conical film of fuel is formed and the breakup into ligaments and droplets occurs. A two-dimensional representation in a section view of this area can be seen in figure 4.11, and is identified as Region D. This region has high refinement with respect to Region A and the cells within it can reach an even higher refinement when the dynamic meshing method requires it.

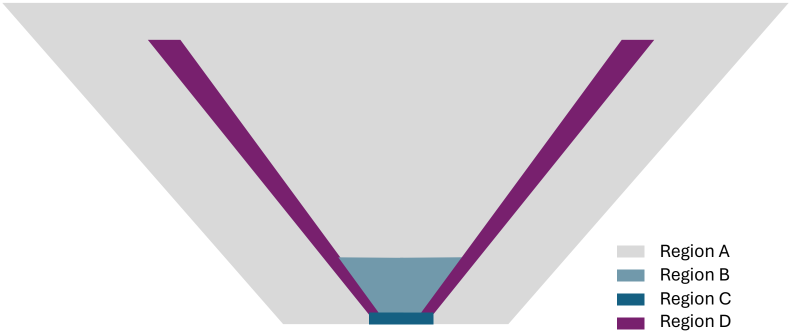

Figure 4.11: Different refinement zones in the external flow region

  - A second refinement zone is defined, identified as Region B in Figure 4.11. This zone occupies a volume of a truncated cone but is contained within Region D. Its purpose is to refine the mesh to capture the depression that helps form the air core. It is refined to higher levels from the base mesh size.
  - A third refinement zone corresponds to the connection zone between the internal flow and the external flow. This region is identified as Region C in Figure 4.11, and its purpose is to refine the area where the fuel film detaches from the walls of the outlet orifice and is expelled outward.
  - The zone where the spray does not interact with the air is identified as Region A in Figure 4.11. This zone has no refinement but has the base size defined for the simulation.

- Another refinement zone consists of the swirl chamber. In this area, it is known that the boundary layer can grow up to 25 μm away from the wall [8]. Therefore, a region close to the wall is also refined here, as shown in Figure 4.12a.

- Finally, another refinement region is the inlet ports; the rectangular section channels through which the fuel enters the swirl chamber. In these channels, it is known that the boundary layer grows up to 15 μm away from the wall [8]. Therefore, a refinement is made in the region within 15 μm from the wall, as seen in Figure 4.12b.

The different levels of refinement applied in each of these zones are detailed in Chapter 5, where a Mesh Sensitivity Analysis is performed.

4.2.4 Properties of working fluids

In this study, a baseline or reference case is first simulated using a theoretical fuel, n-heptane. This theoretical fuel is also used for the simulations that allow the mesh sensitivity study to be performed. Once the best mesh is selected based on this sensitivity study, simulations with the chosen mesh will be conducted for different fuels to perform the parametric study in Chapter 6

The computational model for this reference case consists of an incompressible liquid injected into an incompressible air atmosphere at high speed. Therefore, in the two-phase flow, two immiscible phases coexist: a gaseous phase, composed of air ($77\% N_2$ and $23\% O_2$); and a liquid

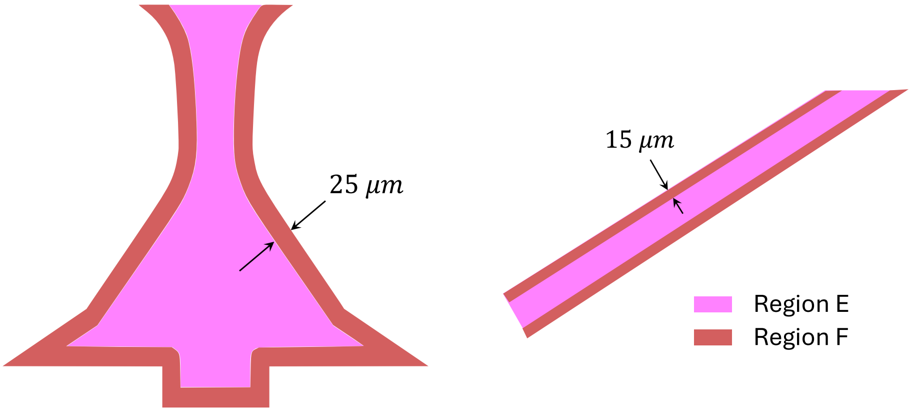

(a) (b)

Figure 4.12: (a). Longitudinal section view of the swirl chamber showing the regions with different mesh refinement in two dimensions (b). Longitudinal section view of the tangential fuel inlet ports also showing the mesh refinement zones.

phase, corresponding to the fuel n-Heptane (C_7H_{16}). The physical properties of both phases required for this hydrodynamic study, which correspond to their thermodynamic state at a temperature of 298 K, are summarized in Table 4.2.

Property	Air	n-Heptane
Operating Temperature [K]	298	298
Density $\left[\mathrm{kg/m^3}\right]$	1.185	681.7
Kinematic Viscosity $\left[\mathrm{m^2/s}\right]$	$1.568 \cdot 10^{-5}$	$5.671 \cdot 10^{-7}$
Surface Tension [N/m]	–	0.0197

Table 4.2: Air ($77\% N_2$ and $23\% O_2$) and liquid fuel (C_7H_{16}) physical properties for the reference case.

4.2.5 Turbulence modelling

In this study, two approaches are used in turbulence modeling: URANS and LES. The process is initiated with simulations using closure models in the URANS approach to establish initial conditions and achieve a stable simulation where the spray flow forms a conical sheet. This transition phase of the simulation does not have physical validity, as the URANS model is used to advance the simulation in time. However, this helps to significantly reduce computation time due to the lower computational demand of the URANS model compared to the LES approach. Once this stable simulation with the formed conical sheet is achieved, the LES approach is implemented to address the specific turbulent scales of the problem. As also explained in [8], the $k-\varepsilon$ model, specifically the RNGkEpsilon submodel from OpenFOAM, suitable for incompressible flows, is used for the URANS simulations. For the LES simulations, the SGS WALE model is employed, which adjusts the turbulent viscosity in the boundary layer. Regarding wall treatment, the URANS simulations required wall laws due to less refinement of the cells near the wall, resulting in $y+ > 5$ values. However, with the switch to LES and the use of higher refinement, these wall laws were no longer necessary.

4.2.6 Numerical schemes

To numerically solve the partial differential equations that constitute the computational model of this study, numerical integration schemes (temporal and spatial), interpolation schemes, and derivative approximation schemes are used. These schemes are required by the finite volume method and the temporal advancement of the equations, as already described in sections 3.2 and 3.3. These schemes determine the accuracy and stability of the simulation and, therefore, also its computational cost.

In OpenFOAM, these numerical schemes are chosen for each type of term resulting from numerical integration and the finite volume discretization of the various conservation equations. The selection of these schemes is made in the *fvSchemes* file contained in the *system* directory. This file classifies each type of term present in the discretized conservation equations resulting from applying the FVM method and temporal integration.

In OpenFOAM, the temporal integration schemes can be chosen for each conservation equation and are identified in the *fvSchemes* file as *ddtSchemes*. The discretization through the FVM involves two types of numerical integration: volume integrals over each cell or surface intrgrals over each face, each one depending on the nature of the corresponding term of a conservation equation: advective or diffusive fluxes, or to source or sink terms. In OpenFOAM, these numerical integration schemes over faces or cells can be chosen by the user. By default, OpenFOAM will perform this integration using Gaussian points. This numerical integration of terms results in discretized conservation equations in terms of values at cell faces or cell corners. The schemes that are typically chosen with greater freedom by the user are the interpolation schemes for values at cell centers from values on the faces. Below is a list of all types of terms that may appear in a conservation equation and for which OpenFOAM allows the user the freedom to choose their respective integration or interpolation schemes [31].:

- *ddtScheme*: allows choosing the scheme for temporally integrating first or second temporal derivatives, e.g., $\partial\boldsymbol{\Psi}/\partial t, \partial^2\boldsymbol{\Psi}/\partial^2 t$
- *gradSchemes*: allows choosing both the numerical integration scheme and the interpolation scheme for terms with gradients $\nabla\Psi$
- *divSchemes*: allows choosing both the numerical integration scheme and the interpolation scheme for terms with divergence of fields $\nabla\cdot\Psi$
- *laplacianSchemes*: allows choosing both the numerical integration scheme and the interpolation scheme for terms with Laplacians $\nabla\cdot\Gamma\nabla\Psi$, with diffusivity Γ
- *snGradSchemes*: allows choosing both the numerical integration scheme and the interpolation scheme for terms that calculate gradients normal to the surfaces defining the faces.
- *interpolationSchemes*: allows choosing a default interpolation scheme for those terms where no scheme is specified.

In this study, the temporal integration scheme for all conservation equations is an implicit scheme, backward Euler, except for the α^{fuel} advection equation. For this equation, a scheme available in OpenFOAM described in section 3.3, the Blended Crank-Nicolson scheme, is chosen. This is because this computational model, after being tested with various schemes for the α_{fuel} equation, diverges when using a second-order temporal integration scheme ($\mathcal{O}(\Delta t^2)$). Therefore, the coefficient β of the Blended Crank-Nicolson scheme from equation 3.23 is utilized. A value of $\beta = 0.9$ is used so that a pseudo second-order scheme is employed.

The numerical integration schemes over the cell for each of the terms and the interpolation schemes that work best for this model have been determined in [8] and are summarized in Table 4.3.

Terms	Numerical integration	Interpolation
divSchemes		
α^{fuel}	Gauss	vanLeer01
others	Gauss	linear
gradSchemes	Gauss	linear
snGradSchemes	Gauss	limited corrected
laplacianSchemes	Gauss	limited linear corrected

Table 4.3: Numerical schemes for the FVM method selected in OpenFOAM for this study.

Secondly, the interpolation scheme for the divergence terms in the alpha equation, which define the advective fluxes, is chosen to be *vanLeer01* instead of linear. This scheme, in addition to being second-order and linear, also bounds the alpha value between 0 and 1. In general, all integration and interpolation schemes are second-order accurate, and along with the temporal integration schemes, which are also second-order, this makes the overall computational model globally second-order accurate [8].

4.2.7 Linear Solvers

Once the algebraic systems of linear equations are constructed using the finite volume method and temporal integration, it is necessary to choose the solution algorithms for these systems. Despite being linear equations, the large number of cells in a typical fluid flow problem results in matrices of very large sizes, on the order of 10^6 to 10^{10} elements. This makes it computationally infeasible to solve them using matrix inversion.

In OpenFOAM, the type of iterative solution algorithm for these systems of equations can be chosen in the *fvSolution* file. For this study, Muñoz [8] determined the most efficient algorithms for solving the systems of equations for the respective fields in this model. These algorithms are listed in Table 4.4 for each field solved in this model.

Variable	Solver	Smoother	Preconditioner
α_{fuel}	smoothSolver	symGaussSeidel	–
Presión	PBiCGStab	–	DIC
Velocidad	smoothSolver	GaussSeidel	–
k, ε	smoothSolver	GaussSeidel	–
ν_t	GAMG	GaussSeidel	–

Table 4.4: Iterative solvers selected in OpenFOAM for this study.

Each of these methods decomposes the original system of equations $Ax = b$ such that it takes the form $x^{k+1} = Tx^k + d$. Thus, the unknown vector x in each iteration can be recalculated using a matrix T and a vector d. This matrix T is constructed from a preconditioning matrix: $T = M(M^{-1} - A)$, and it is said that a preconditioned system is used when the matrix M is much simpler to operate than the matrix A. These methods iterate until reaching a user-defined tolerance limit: $\epsilon = |x^{k+1} - x^k|$ or a maximum number of iterations. In OpenFOAM, various preconditioned iterative methods can be chosen, but within OpenFOAM terminology, a distinction is made between preconditioners for conjugate gradient methods and preconditioners for smoothed iterative methods. Thus, smoothed methods require specifying the type of smoother, and preconditioned conjugate gradient methods require specifying the type of preconditioner.

Finally, in the simulations carried out for the mesh sensitivity study and the parametric study, the Courant number is limited to be less than 0.4 due to the multiphase nature of the problem, to ensure the correct advection of the interface [8].

4.3 Simulation strategies

In order to save computational costs during the transient part of the simulation, in wich the spray is formed and it reachs a stabilized state, a step by step strategy was used for this simulation. Each stage of the simulation has its own numerichal schemes and turbulence closure model as described in section 4.2.5. These different stages are described below.

1. Initialization: This stage is further subdivided into three sub-stages.
    - Sub-stage 1: The simulation is launched in a smaller domain, with first-order schemes, using URANS turbulence models, and without adaptive meshing (No AMR).
    - Sub-stage 2: Once the spray has formed, the domain is extended, and AMR meshing is applied (AMR 1st order).
    - Sub-stage 3: Finally, the schemes are changed to second-order for the simulation. This stage consumes the most computation hours (AMR 2nd order).
2. Temporal study window: Once atomization has stabilized in second-order, the average fields are reset, and data is collected every microsecond. (Data window)

4.4 Post-processing Algorithms in Paraview

Paraview and its post-processing and data extraction tools were used to quantify essential characteristics of atomization.

Droplets detection algorithm

In [8], it is explained how an algorithm was built, consisting of a combination of filters, to calculate data about the droplets and ligaments formed in the atomization simulations of this study. This algorithm allows for the calculation, for an instant of the simulation, of the number of structures considered droplets or ligaments separated from the fluid body coming from the inlet ports and that have not separated into another liquid volume

In this study, a droplet or ligament is defined as an individual structure formed by contiguous cells for which the value of the liquid volume fraction at its centroid is greater than or equal to a threshold: $\alpha^i_{fuel} \geq \gamma$. Each of these structures corresponds to a ligament or a droplet separated from the intact liquid core. This intact core corresponds to the volume defined by all contiguous cells that satisfy $\alpha^i_{fuel} \geq \gamma$ and that have not separated from the liquid volume coming from the inlet ports. This set of droplets and ligaments can be defined and identified through the combination of ParaView filters described by [8]. In this way, data can be extracted from ParaView and processed in a Python script developed and described by [8], allowing for the calculation of the components of the structure's velocity, its volume, and the position of its centroid.

Once the data for each instant has been extracted, the volume of each ligament or droplet is calculated first by means of a weighted sum based on the volumetric fraction of each cell belonging to the structure.

$$V_{\text{drop}} = \sum_{i=0}^{\text{nCells }-1} V_i \cdot \alpha_{fuel,i} \tag{4.1}$$

From this volume, it is possible to calculate the coordinates of the volumetric centroid of the structure defining a ligament or a droplet.

$$\bar{x}_{\text{drop}} = \frac{1}{V_{\text{drop}}} \sum_{i=0}^{\text{nCells}-1} x_i \cdot V_i \cdot \alpha_{fuel,i} \tag{4.2}$$

Similarly, the other two coordinates, $\bar{y}drop$ and $\bar{z}\text{drop}$, are calculated. The magnitude of the velocity components of the structure is also calculated using weighting.

$$u_{\text{drop}} = \frac{1}{V_{\text{drop}}} \sum_{i=0}^{\text{nCells}-1} u_i \cdot V_i \cdot \alpha_{fuel,i} \tag{4.3}$$

The components v_{drop} and w_{drop} are calculated in a similar manner. To calculate a size of the structure related to a spherical shape, the equation for the volume of a sphere is used, where the volumetric volume V_{drop} is introduced, and the volumetric diameter D_V is solved for.

$$V_{\text{drop}} = \frac{4}{3}\pi {R_V}^3 \quad \rightarrow \quad D_V = \sqrt[3]{\frac{6}{\pi} \cdot V_{\text{drop}}} \tag{4.4}$$

To calculate the tangential velocity of the structures $U_{\theta,\text{drop}}$, the rectangular components of the droplet velocity u_{drop} and v_{drop} are used (the axial component w_{drop} does not contribute to the tangential velocity). This tangential velocity is calculated as the sum of the components of u_{drop} and v_{drop} in the tangential direction θ, as shown in Equation 4.6. But first, the angle defining the radial direction of the droplet must be calculated.

$$r_{\text{drop}} = \sqrt{x_{\text{drop}}^2 + y_{\text{drop}}^2}; \quad \alpha = \arctan\left(\frac{y_{\text{drop}}}{x_{\text{drop}}}\right) \tag{4.5}$$

$$U_{\theta,\text{ drop}} = \sin(\alpha) \cdot u_{\text{drop}} + \cos(\alpha) \cdot v_{\text{drop}} \tag{4.6}$$

And the droplet's radial velocity component:

$$U_{r,\text{ drop}} = -\cos(\alpha) \cdot u_{\text{drop}} + \sin(\alpha) \cdot v_{\text{drop}} \tag{4.7}$$

All these equations above allow calculating, for each instant, the variables defining the size and velocity of the droplets resulting from atomization at a given time t.

Mean thickness computing

In this Master's Thesis, Paraview and its macro tool were also utilized to program and automate the extraction of time-averaged and space-averaged values of characteristic lengths of the spray in a steady state. This spray develops as a film with a hollow cone shape. Therefore, it is of interest to determine the diameter of the air core entering the atomizer, the thickness of the fuel film from the atomizer throat, and also its evolution in the external flow.

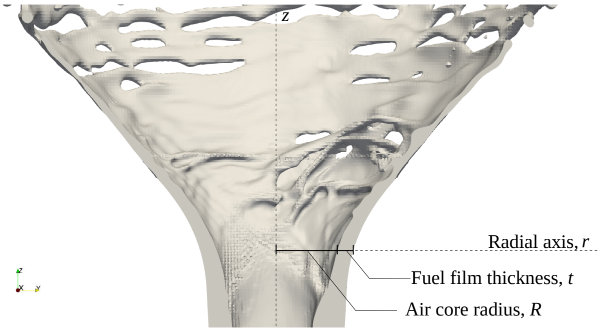

Figure 4.13: Axisymmectric section view of the hollow cone spray for the visualizaztion of the aircore radius R and the fuel film thickness measurements in the internal flow region for a specific axial position and a specifc radial axis r.

For various axial positions along the atomizer, taking advantage of the axial symmetry of the flow shape (both inside the swirl chamber and outside it), the radius of the air core R is obtained using radial lines that track the values of the α_{fuel} field and determine where the interface is by locating the points where $\alpha_{fuel} = 0.5$. Figure 4.13 illustrates a representation of the radius of the air core R and the thickness of the fuel film t that are intended to be measured and averaged at different axial positions along the atomizer. At each instant $p \in \{1, 2, \dots, 140\}\,\mu$s and for each axial position $k \in \{k_1, k_2, \dots, k_{N_k}\}\,\mu$m, the spatial average of the radius of the air core and the thickness of the fuel film was obtained:

$$\overline{R}^{p,k} = \left(\frac{1}{N_j}\right)\sum_{j=1}^{N_j} R_j^{p,k}, \quad \overline{t}^{p,k} = \left(\frac{1}{N_j}\right)\sum_{j=1}^{N_j} t_j^{p,k} \tag{4.8}$$

Where N_j is the number of radial lines used at a given axial position to obtain N_j values for the spatial average, and N_k is the number of axial positions at which these average values are desired. The standard deviations of these spatial averages are:

$$\sigma_R^{p,k} = \left(\frac{1}{N_j}\right)\sum_{j=1}^{N_j} \left(R_j^{p,k} - \overline{R}^{p,k}\right)^2, \quad \sigma_t^{p,k} = \left(\frac{1}{N_j}\right)\sum_{j=1}^{N_j} \left(t_j^{p,k} - \overline{t}^{p,k}\right)^2 \tag{4.9}$$

Additionally, the aim is to obtain a temporal average for each axial position k based on these spatial averages calculated at each instant within the time interval of 140 microseconds.

$$\overline{\overline{R}}^{k} = \left(\frac{1}{N_p}\right)\sum_{p=1}^{N_p} \overline{R}^{p,k}, \quad \overline{\overline{t}}^{k} = \left(\frac{1}{N_p}\right)\sum_{p=1}^{N_p} \overline{t}^{p,k} \tag{4.10}$$

The standard deviations of these temporal averages are:

$$\sigma_R^{k} = \left(\frac{1}{N_p}\right)\sum_{p=1}^{N_p} \left(\overline{R}^{p,k} - \overline{\overline{R}}^{k}\right)^2, \quad \sigma_t^{k} = \left(\frac{1}{N_p}\right)\sum_{p=1}^{N_p} \left(\overline{t}^{p,k} - \overline{\overline{t}}^{k}\right)^2 \tag{4.11}$$

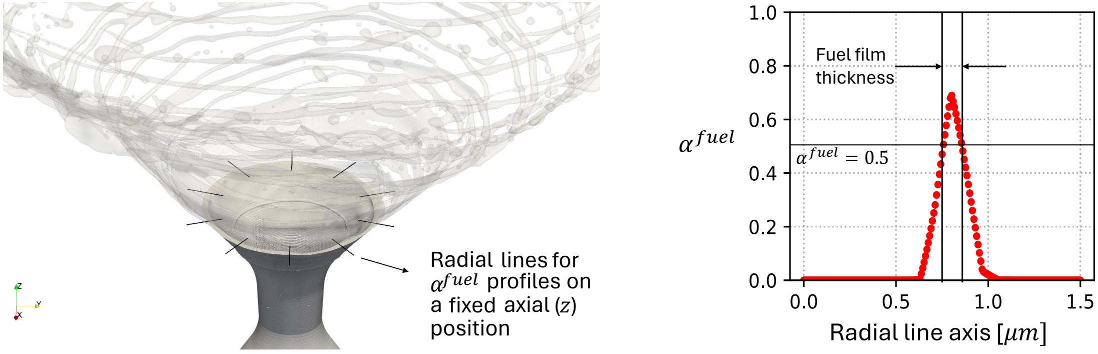

(a) (b)

Figure 4.14: (a). Visual representation of the definition of *PlotOverLine* filters in Paraview to obtain α^{fuel} profiles and calculate spatial thicknesses (b). Profile of α^{fuel} vs x obtained using the data extracted through the *PlotOverLine* filter in Paraview. The characteristic thickness is calculated from this profile.

At a general level, a tool was built to automate this post-processing, so it can be executed simply by launching a Python-built macro from Paraview to extract the data, and a Python script that processes the exported data. This post-processing tool allows the user to choose the number of spatial samples taken for spatial averaging, the number of axial positions along the atomizer, and the number of time instants to be included in the calculation of the averages.

A Python program was developed (which functions as a Paraview macro), allowing the calling and execution of Paraview's respective filters via code to construct profiles of the volumetric fraction field along radial lines to calculate the value of these thicknesses (see Figure 4.14b). These profiles are exported as CSV files, and from these, data is extracted to define the lengths of the air core and spray film thickness. The general macro built in Python is launched in Paraview, thus automating the entire data extraction process for the final temporal averaging. This macro is capable of (for each microsecond of the 140 μs) exporting the volumetric fraction profiles for the same axial position and storing them within the same folder, then creating another folder for the next axial position and saving the volumetric fraction profiles there. All these folders of axial positions are saved in a single folder corresponding to that instant of the simulation (see Figure 4.15). And so on for each of the 140 μs until the entire averaging window is traversed.

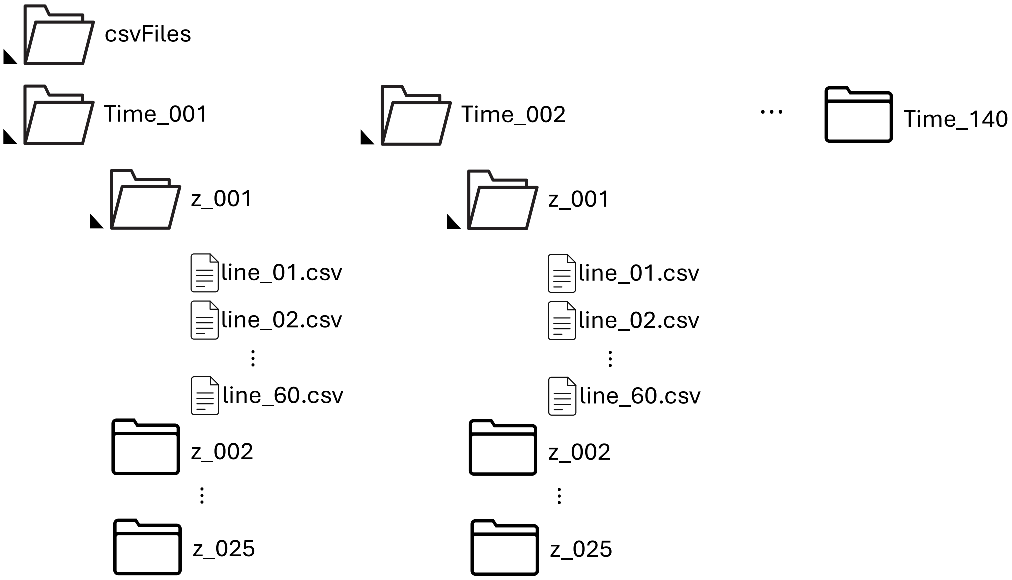

Figure 4.15: Directory organization for storing data for the average thickness calculation performed by the macro in Paraview.

Then, a second Python code is built, which traverses these folders where the data is stored and calculates the values of the air core radius and fuel film thickness, averaging both spatially and temporally.

Chapter 5

Mesh sensitivity analysis

In this section, the results of three simulations of the reference case described in Chapter 4 are presented, each performed with a different meshing strategy. The main objective of this mesh sensitivity study is to reduce the computational cost of the simulations by decreasing the number of cells used in the mesh without losing the necessary resolution to carry out LES simulations. We start with a fine mesh (**Mesh 1**), which was determined to be optimal in the study by [8]. However, this mesh is very costly for conducting the parametric study of this master's thesis; therefore, two new meshes are generated from it: one mesh with the same structure but with a larger base size (**Mesh 2**) and a third mesh (**Mesh 3+AMR**) with the same base size as Mesh 2 but with adaptive, rather than local, refinement: Adaptive Mesh Refinement. In this way, we aim to use coarser meshes with fewer cells that reduce computational cost without compromising the quality of the results.

The results of these simulations with different refinements are studied and compared to determine which refinement is most appropriate for the subsequent parametric study described in Chapter 6. As described in the meshing strategy section 4.2.3, for these atomization simulations, it is advisable to use specific refinement regions to capture the physical distribution of the spray in the domain. Therefore, the meshing strategies do not imply using different refinement zones between meshes; instead, some parameters are varied which, although they do not change the typology or shape of the mesh, cause the different meshes to have higher or lower resolution depending on the cell size in each refinement zone. The parameters that were varied between the different meshes are:

- Base size: Different base cell sizes were used for the different meshes. This base size is defined in the *blockMesh* dictionary of OpenFOAM, indicating the size of the hexahedral cells that make up the base mesh from which the meshing tool, *snappyHexMesh*, refines cells to smaller sizes in user-defined regions. This base size defines level 0 of refinement in OpenFOAM, meaning that refinements to higher levels will be made from this element size as shown in Figure 5.1.

- Regions refinement level: Different refinement levels are defined for volumes of different regions, which are distinguished in Figures 4.11 and 4.12. These levels are defined with respect to the base size as explained in the previous item.

- Boundary layer region refinement level: In flow areas where solid walls are present, such as inlet ports and the swirl chamber, the refinement level is defined to capture the physics of the boundary layer in these regions.

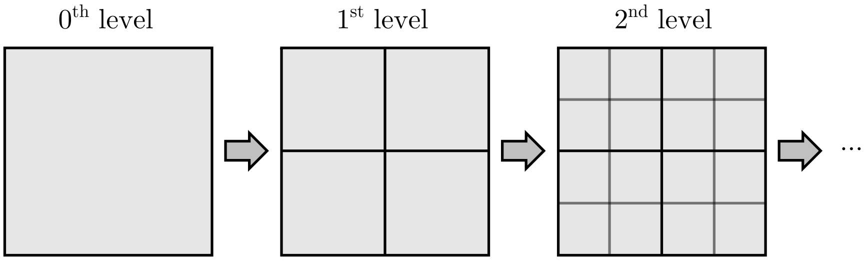

Figure 5.1: Refinement levels in OpenFOAM

- Boundary layer height: Some of the meshes used in this study are also distinguished by the thickness of the boundary layer region chosen to define the size of the boundary layer refinement zone.

The parameters described above that distinguish these meshes and their respective refinements are detailed in the following table: 5.1.

Zone	Parameter	Mesh 1	Mesh 2	Mesh 3+AMR
Entire Domain	Base size	50μm	60μm	60μm
Channels	Refinement level	4	4	4
	BL refinement level	5	5	5
	BL width	10μm	15μm	15μm
Swirl chamber	Refinement level	4	4	4
	BL refinement level	5	5	5
	BL width	20μm	25μm	25μm
External flow region	Inner cone	2	2	$1 \leq f \leq 4$
	Hollow cone	4	4	$3 \leq f \leq 4$
	Merging disk	4	4	$3 \leq f \leq 4$
Total Number of Cells		46.11M	26.07M	14 M

Table 5.1: Refinement parameters in each zone of each mesh used in the mesh sensitivity study

1. **Mesh 1**: This mesh is characterized by having the smallest base size of all, which has a value of 50 μm. This mesh does not implement dynamic meshing (AMR). It refines in certain zones up to level 5 of refinement.

2. **Mesh 2**: It has a base size of 60 μm and increases the height of the boundary layer zone at the inlet ports. It also refines regions passing through different levels of refinement until reaching the fifth level of refinement in these boundary layer zones.

3. **Mesh 3+AMR**: It also has a base size of 60 μm and also passes through several levels of refinement in certain zones reaching level 5. It implements dynamic meshing AMR up to level 4, meaning that in certain areas of the mesh, it reaches level 4 of refinement based on the AMR method criterion established for this study. This criterion implies that based on the value of the liquid volumetric fraction, it refines up to level 4 in cells with values of $\epsilon \leq \alpha_i^{fuel} \leq 1 - \epsilon$ for a value of ϵ indicating cells containing the interface.

From here on, different qualitative and quantitative results of the simulations performed on the various meshes are described in order to compare the resolution with which each mesh captures the main physical phenomena associated with simplex atomization. Among these phenomena are: the formation of the conical film, its breakup into ligaments and droplets, the magnitude of characteristic lengths of the spray such as the diameter of the air core and the thickness of the film at the outlet, and finally, the quality of atomization according to the statistical study of the droplets captured by each mesh.

These results are obtained from data extracted at various instants of the numerical simulation solutions. The data is extracted from the numerical solution at the same frequency (1 μs) to obtain a temporal data window of the simulation (a total of 222 μs). This data is extracted once the atomization simulation has entered a steady state, i.e., once the spray has formed in the form of a conical sheet and once the air core has reached the lower wall of the swirl chamber cylinder.

5.1 Computational cost

The computational cost of atomization simulation with each of the different meshes can be seen in Table 5.2. This cost is expressed in terms of total calculation hours required for the simulation to advance one microsecond of simulated time.

	Mesh 1	Mesh 2	Mesh 3+AMR
CPUh/ms	148.6e3	155.8e3	201.3e3

Table 5.2: Computational cost demanded by each one of the meshes

The three meshing methodologies have a cost of the same order of calculation hours. The one with the highest cost, in terms of calculation time, is the mesh with adaptive refinement (AMR); however, due to its considerable difference in the number of cells (a 50% reduction in required cells) compared to the other methodologies, this mesh becomes the most appropriate by considerably saving computational storage resources and post-processing tasks.

5.2 Qualitative analysis

In this qualitative analysis, the visual appearance of several of the solution fields solved using the different meshes is described, emphasizing the ability of each mesh to capture the formation of the conical sheet, the air core, and the mesh quality based on the IQ_ν index and the parameter y^+.

5.2.1 Appearance of the spray

Simplex atomization, as detailed in section 2.4, occurs due to the conical sheet formed by the fuel when expelled as a rotating annular flow. This conical sheet breaks into ligaments and droplets due to fluctuations in its free surface caused by flow oscillations and contact with air. The formation of the conical sheet, along with a wide spectrum of oscillations and deformations, is largely captured by the computational model in this study and can be observed in Figure 5.2, where visualizations of the fuel-air interface are represented as the isosurface where the volume fraction field has an iso value of 0.5 at a specific instant for each mesh.

In Figure 5.2, a frontal view (plane yz) and a top view (plane xy) of these isosurfaces representing the liquid-air interface are shown. In these isosurfaces, the formation of the air core and the conical sheet that breaks into ligaments and droplets in the external flow region can

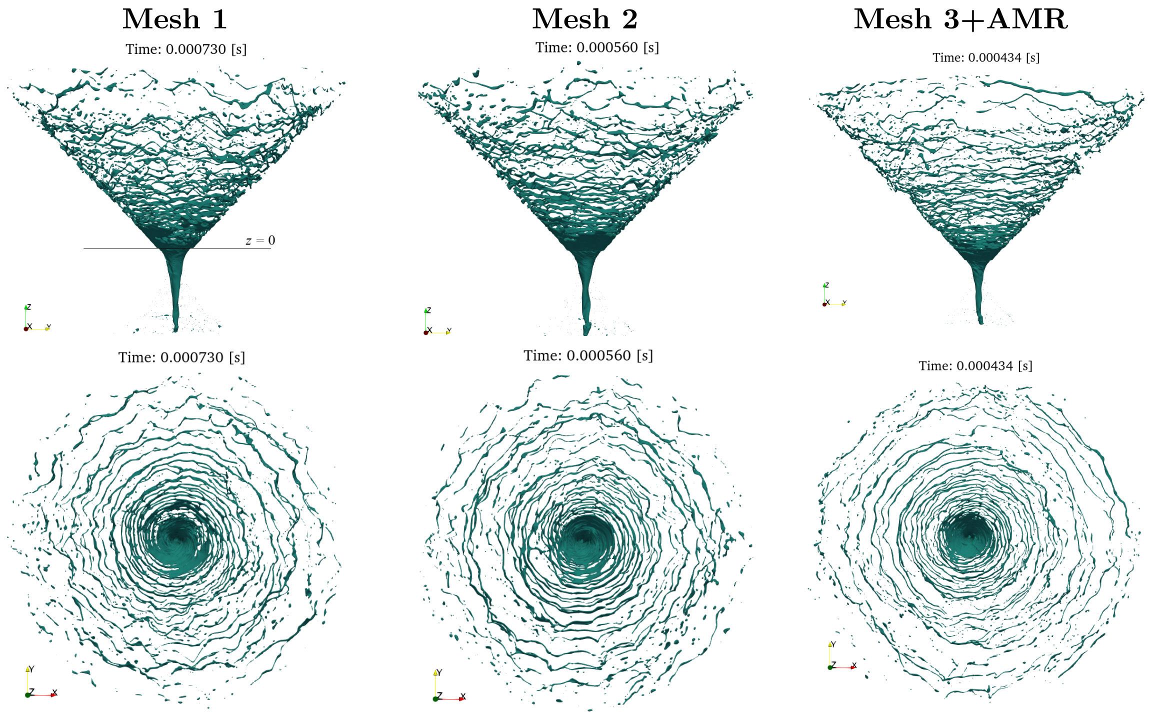

Figure 5.2: Instantaneous isosurfaces $\alpha^{fuel} = 0.5$ obtained with the three different meshes

be observed. The three meshes coincide in that the conical sheet breaks and perforates a few micrometers (at a distance of the order of 10^2 μm) from the outlet orifice, and it has a leading edge from which ligaments detach in the form of spiral strings, which, as they progress, break into shorter segments and droplets. However, the mesh with adaptive meshing shows thinner and smoother ligaments.

Para observar y describir con más detalle la interacción de las dos fases capturada por cada una de las mallas, se muestran vistas de sección longitudinal del flujo en el plano medio $x = 0$, en la figura 5.3, y vistas de sección transversal del flujo en el plano del orificio de salida $z = 0$, en la figura 5.4. To observe and describe in more detail the interaction of the two phases captured by each of the meshes, longitudinal section views of the flow in the mid-plane $x = 0$ are shown in Figure 5.3, and cross-sectional views of the flow in the outlet orifice plane $z = 0$ are shown in Figure 5.4.

In Figure 5.3, it can be observed that the three meshes capture the formation of the air core and agree that this air core has a maximum diameter in the area of the outlet orifice. This maximum diameter determines the thickness of the fuel film expelled into the external flow region. The three meshes agree that this air core progressively reduces its diameter in the negative axial direction and also becomes increasingly unstable as it approaches the bottom of the lower cylinder of the swirl chamber.

The detailed views of Figure 5.3 show how each mesh captures ligament and droplet breakup thanks to the smaller-sized cells with level 4 refinement. At first glance, it can be appreciated that all meshes capture a similar thickness of the film, which determines the size of the ligaments and thus of the droplets. However, it is evident that the AMR mesh achieves this level of resolution with a much smaller number of cells, as it only reaches the fourth level of refinement in the

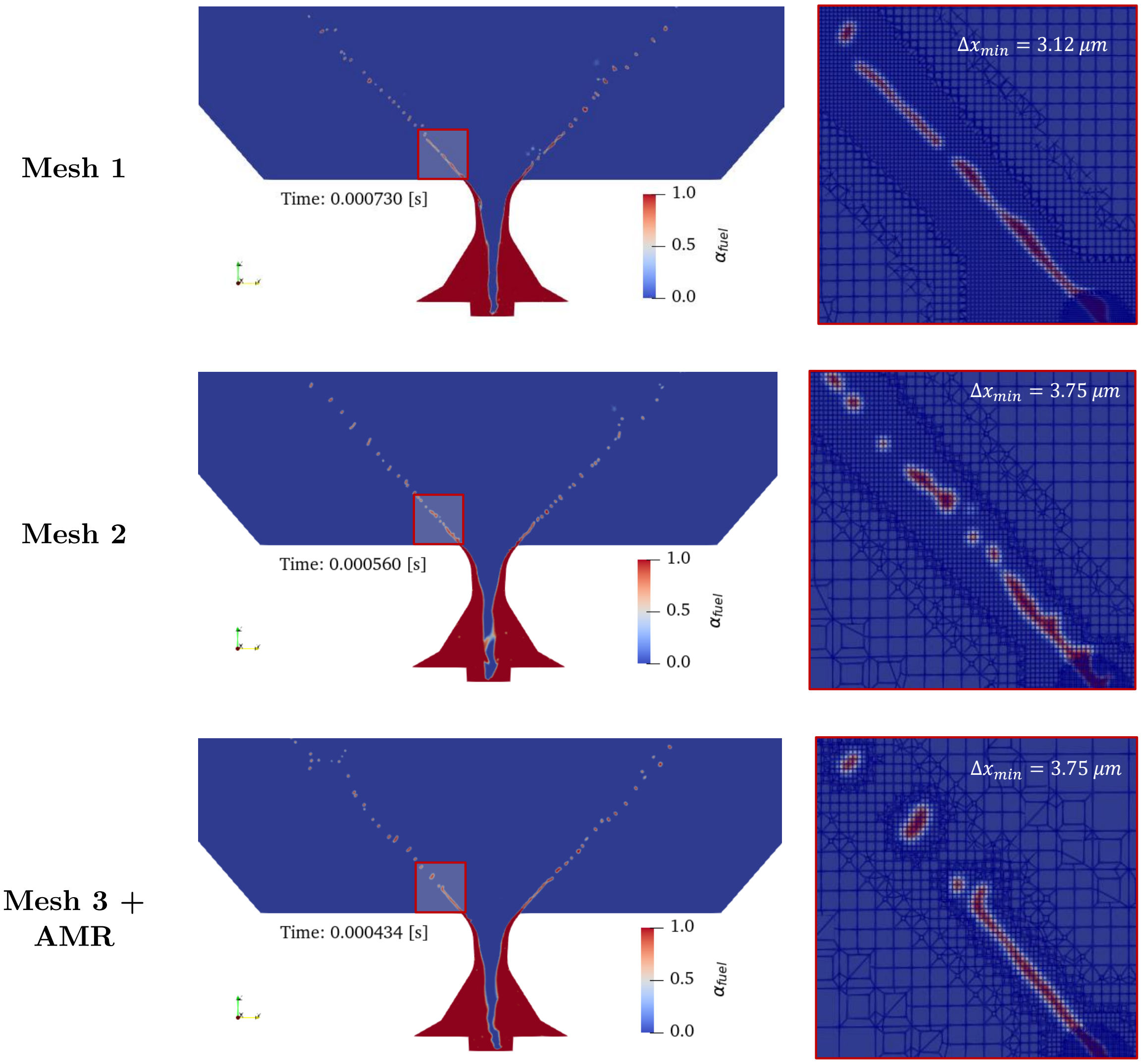

Figure 5.3: Section view on the yz plane of the Fuel volume fraction field and a detailed view of the cell sizes for each mesh

areas where the interface is located. This means that qualitatively, the reduction in the number of cells used in Mesh 3+AMR at least qualitatively does not lose any significant information regarding atomization compared to meshes with more elements, but rather captures the same mechanisms of fuel formation and disintegration.

In Figure 5.4, it can be observed from the instantaneous field α^{fuel} how each mesh captures differently the oscillations of the free surface of the annular flow just before it is expelled into the external flow region. The capture of these oscillations is relevant because they affect the stability of the fuel sheet surface and induce it to deform and break into ligaments. Mesh 2 presents higher diffusivity and greater oscillations in the interface due to the increased cell size compared to Mesh 1. On the other hand, Mesh 3 with AMR shows lower diffusivity both in the contours of the instantaneous field and in the average field, which indicates that this mesh, although using fewer cells, does not worsen the results compared to the finer mesh at the interface.

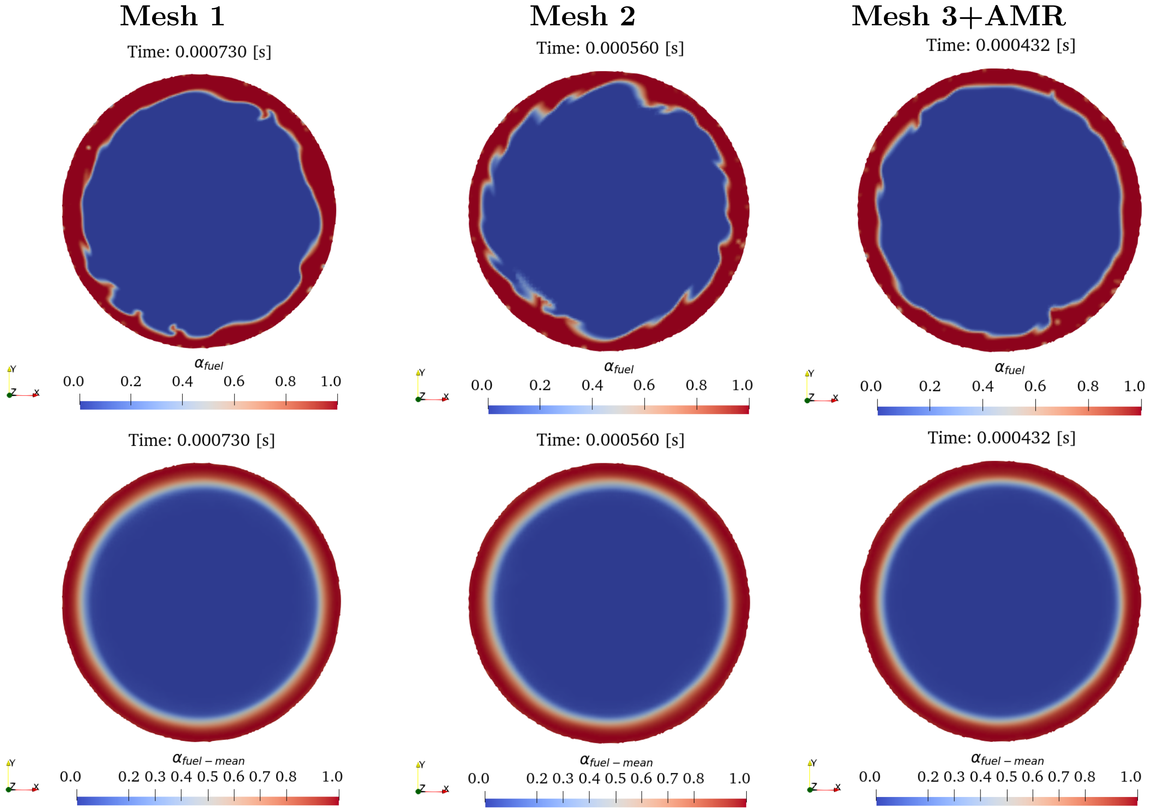

Figure 5.4: Fuel volumetric fraction α^{fuel} contours on the $z = 0$ plane for the three different meshes

5.2.2 Qualitative description of the velocity field

The qualitative description of the velocity field in these simplex atomization simulations allows identifying areas with higher mass flow rates as well as areas where the flow reverses or enters recirculation. In Figure 5.5, contours of instantaneous and averaged velocity magnitude and axial component U_z fields can be observed.

In each image of Figure 5.5, taking advantage of the symmetry of the mid-plane section view ($x = 0$), the instantaneous velocity magnitude field is shown on the left and the time-averaged velocity magnitude field is shown on the right. The contour of the instantaneous velocity magnitude shows how high fuel flow velocities are captured in the region behind the throat of the swirl chamber where the flow reaches its maximum velocity. Note that it is not at the throat height (the point where the injector diameter is narrowest) where the zone of highest internal flow velocity is located, but rather this occurs at the point where the fuel film is minimum. At this point, it is downstream of the throat because the cross-sectional area of the flow is maximally reduced where the fuel film is minimum, and thus to conserve mass, the annular fuel flow acquires higher velocity where it has a smaller cross-sectional area.

In the internal flow region, the velocity can be seen to increase from zero at the walls and in the recirculation zones to velocities of up to 50 m/s in the annular flow zone before being expelled. These high velocities are what maintain and provide the momentum necessary to form the conical sheet and to create the depression zone that sucks in the air core. Recirculation zones can also be seen in the cylinder zone inside the swirl chamber.

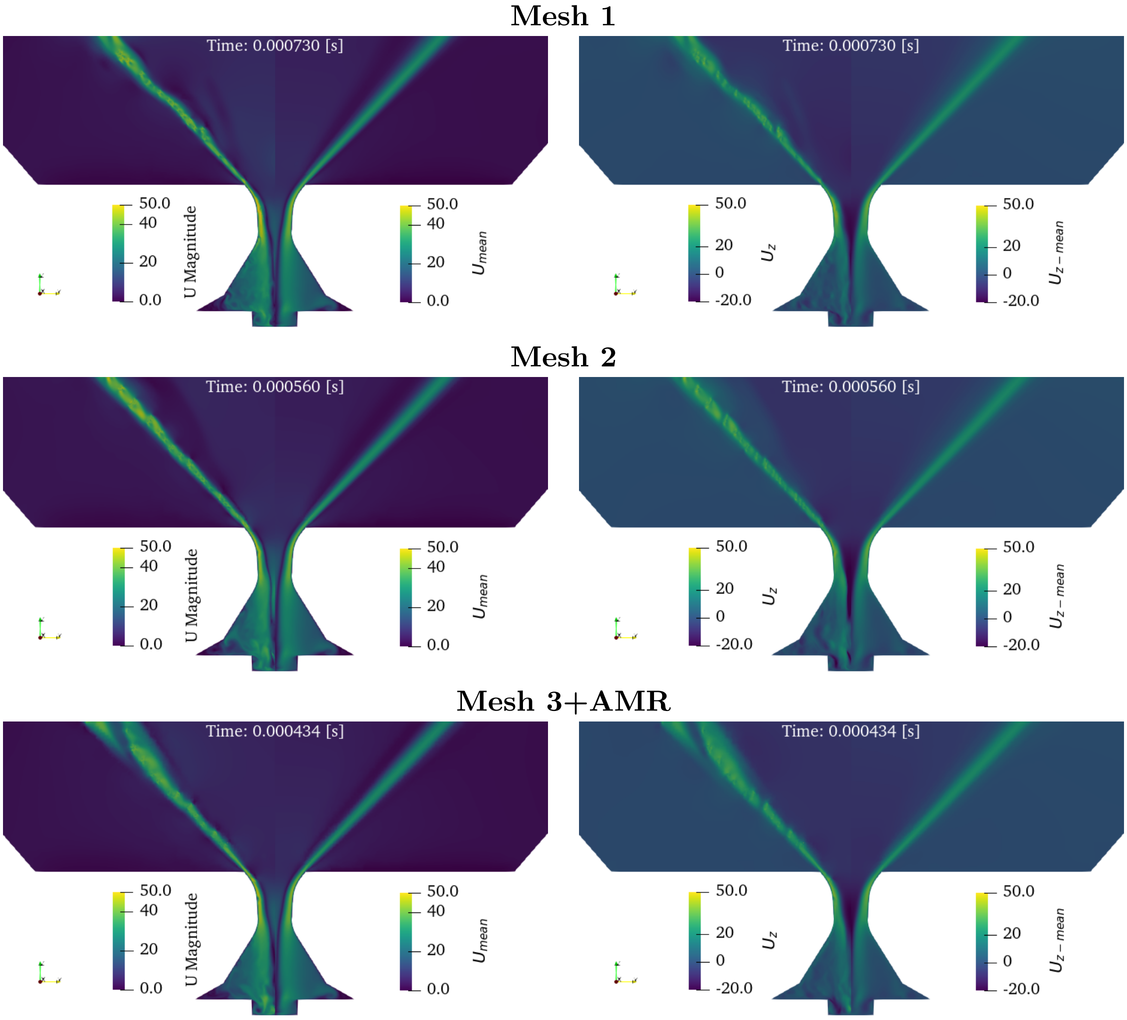

Figure 5.5: Section view on the yz plane of the mean and instantaneous velocity field, its magnitude U and its axial component U_z

It can also be seen that in the throat region and in the annular fuel flow downstream of the throat, there is a high velocity gradient normal to the walls of the atomizer. This velocity gradient indicates that there is a boundary layer flow in the annular fuel flow. Velocity gradients in the boundary layer flow will generate strong turbulent flow fluctuations that will be transported and propagate in the flow, destabilizing the conical sheet expelled through the outlet orifice. It is noticeable that although all meshes capture a similar distribution of the velocity field, the color scale shows that mesh 1 captures higher velocity magnitudes in the boundary layer annular fuel flow region. This may be because this mesh, being finer, more faithfully captures the turbulent fluctuations that distribute turbulent kinetic energy and generate a flow with greater momentum transport and therefore higher velocity magnitudes.

Another velocity gradient can also be seen in the region of the air flow that enters and forms the air core inside the injector. It can be observed that in the direction normal to the walls of the atomizer, after the liquid boundary layer, there is again a decrease in velocities to zero in the contact zone between the liquid and the air, and it increases again as we move in this direction towards the center of the injector. This shows that there is another boundary layer flow for the air entering the injector.

The average velocity magnitude field captured by the different meshes shows that the interface zone, both in the internal and external flow, is diffuse. This explains that the interface has oscillations already from the internal flow which propagate and eventually fragment the fuel sheet. The same can be observed in the external flow zone where the flow is completely unstable and the free surface of the fuel is very unstable and breaks up to form ligaments and droplets. These oscillations in the free surface of the annular flow are what force dimensions of the air core and fuel film thickness to be calculated as averaged quantities.

In Figure 5.5, the contours of the axial velocity U_z show that this component has a distribution similar to the velocity magnitude, although it is slightly more uniform. It can be observed that the axial velocities are close to zero in the swirl chamber and in the spin chamber, where the main velocity components are tangential and, instead, the axial velocity is low. However, downstream, towards the region behind the throat, the axial component of the liquid zone progressively increases. Like the velocity magnitude, the axial component reaches its maximum point in the area of the smallest cross-sectional area at some point downstream of the throat. Note that the color bar allows appreciation of both positive and negative axial velocities. Negative values of this component can be observed in the air core region, where the airflow is directed opposite to the axial advancement of atomization, meaning that the air is being sucked in.

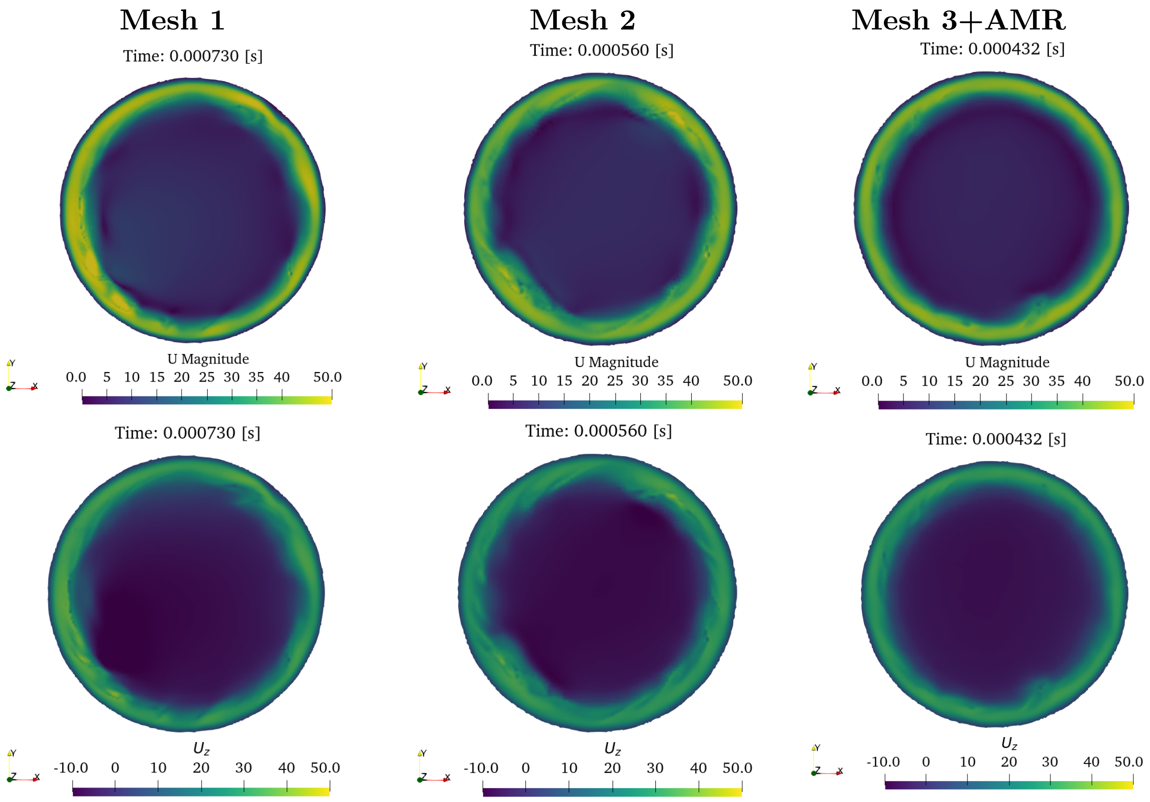

Figure 5.6: Instantaneous velocity magnitude and axial component contours on the $z = 0$ plane for the three different meshes

In Figure 5.6, it can be observed that in the plane of the cross-sectional section of the outlet orifice, the areas where the velocity magnitude is high coincide with the areas where the axial component is high, showing that at this point of the flow, the main flow component is axial.

5.2.3 Mesh quality indices in LES simulations

As explained in section3.4.4, the LES approach simulations in this work must ensure that their mesh quality indices are within reliable intervals, ensuring that the largest turbulent scales are being resolved. Contours of these mesh quality indices calculated according to equations 3.65 are shown in figures x, y, z. This mesh quality indicator quantifies the fraction of resolved turbulent viscosity compared to the total turbulent viscosity, i.e., the resulting plus that introduced by the SGS model.

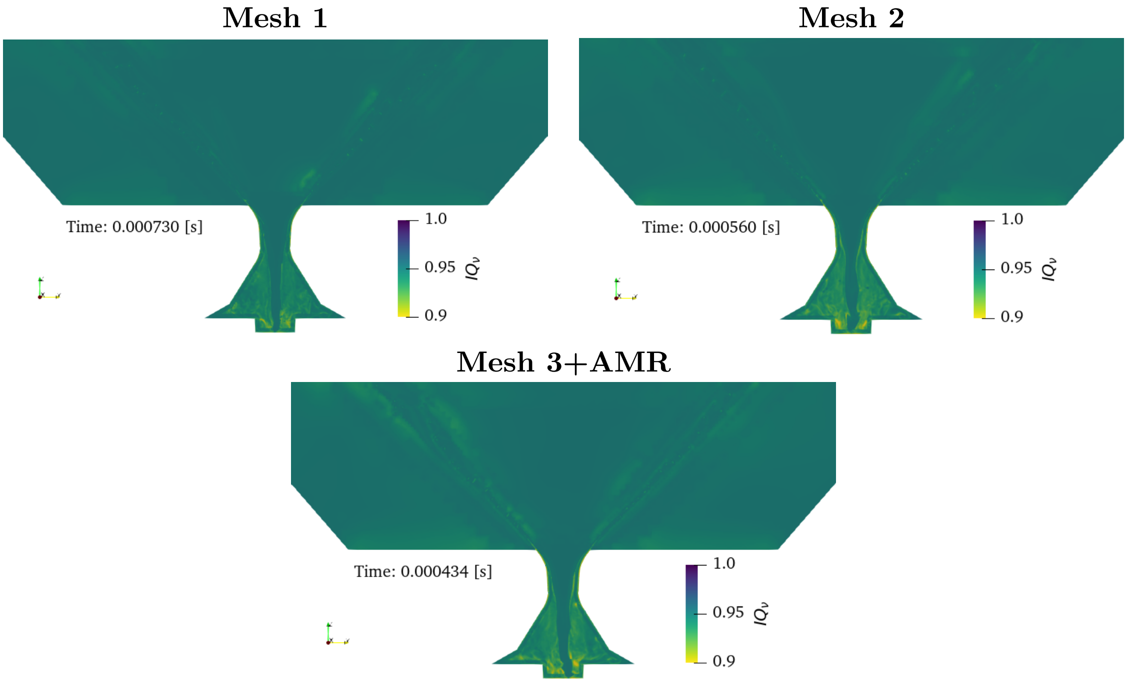

Table 5.3: Section view on the yz plane of the IQ_ν index for a specific instant of the simulation of each mesh

From figure 5.3 several observations can be made:

- It can be seen that all meshes have appropriate IQ_v values to be considered LES approach simulations, i.e., values close to or greater than 0.9, indicating that turbulent viscosity is resolved in most of the domain, which is characteristic of an LES approach.
- It can be observed that all meshes tend to lose quality in the same areas:
  - In the internal flow region at the lowest part of the air core. In this area, the air core is unstable and generates turbulent scales that are difficult to capture by the mesh. Therefore, in these areas, the SGS subgrid model will need to simulate fluctuations at these scales.
  - In the region near the wall in the throat and upstream. It can be seen that although the mesh is refined to the maximum level used, the high velocities of the incident flow

on this wall cause turbulent scales to form that also escape the mesh resolution and therefore need to be filtered and modeled.

- It can be noticed that in the internal flow region, for Mesh 2, the IQ_ν index is reduced, indicating that turbulence models introduce a greater amount of turbulent viscosity. This may be because, by increasing the mesh size compared to Mesh 1, fewer turbulent scales are captured than with the smaller mesh size. However, these values rise again for the mesh with dynamic meshing compared to Mesh 2. Although it should also be noted that the mesh with AMR has the highest values of IQ_ν in the external flow region.

5.2.4 Wall units contours

When comparing the contours of the y^+ value in the centroids of the cells adjacent to the atomizer walls, it can be seen that this value remains below 5. It is known that the wall law described in section 3.4.5 can be applied to a flow adjacent to a solid wall as long as this flow is represented by a fully developed turbulent flow along a straight wall. In this study, the inlet ports and the inflow region are well represented by this type of flow. Therefore, the y^+ values obtained, which are below 5, show that the mesh size is refined enough to accurately capture the velocity gradients. Furthermore, considering that in all three meshes, the mesh size is uniform near the walls, the use of wall laws can be omitted, as any of the three captures the development of the turbulent boundary layer and each of its stages.

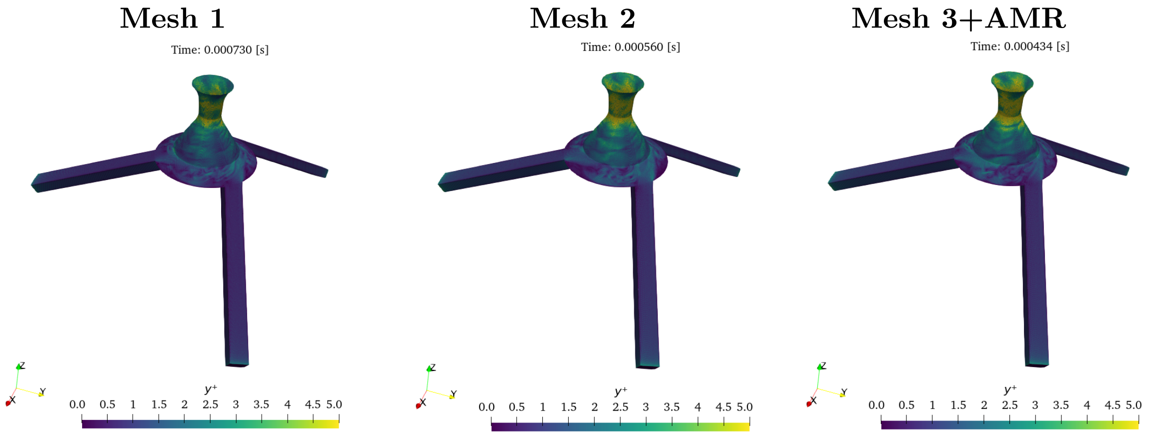
Mesh 1 **Mesh 2** **Mesh 3+AMR**

Figure 5.7: Contours of the wall units of the centroids of the cells attached to the wall in each mesh for the three different meshes

5.3 Quantitative analysis

In this section, some simulation results are quantitatively compared in order to compare with greater precision the quality of the atomization results of each mesh. The magnitudes of the velocities in each flow direction are also recorded and their influence on the statistical study of the drops formed is described.

5.3.1 Swirl number

As explained in section 2.4.1, the swirl number S allows calculating the ratio of the axial transport of tangential momentum to the axial transport of axial momentum at an axial position

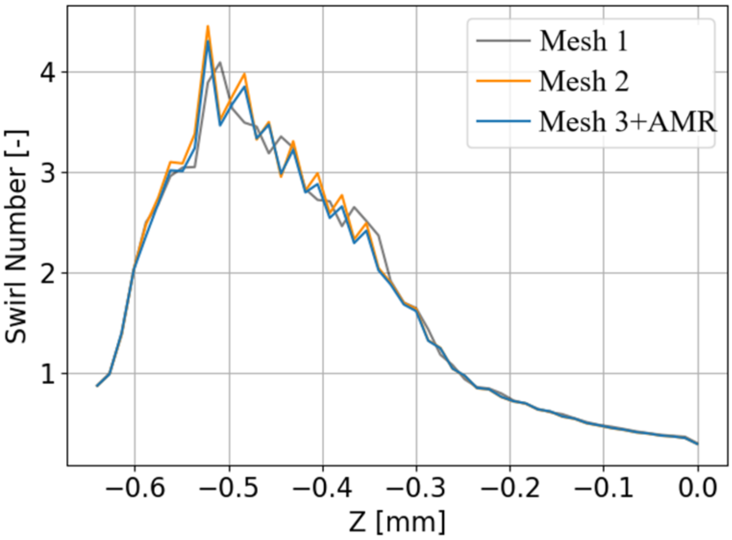

Figure 5.8: Swirl number computed along the axial axis for each mesh

of the atomizer. These two transports are represented by the tangential velocities and axial velocities of the flow at that axial position. For the three meshes in this sensitivity study, the swirl number is calculated using equation 2.3, and the resulting curves are shown in figure 5.8.

The three meshes capture the same trend of the swirl number along the axial direction within the atomizer. This number reaches maximum values near the positions $z = -0.5$ mm because this area has the largest diameter in the swirl chamber, where the flow is primarily rotational with little advancement in the axial direction. As we approach the exit orifice at $z = 0$, the swirl number decreases because, as the cross-sectional area reduces, the flow accelerates in the axial direction and gains higher axial velocity. This causes the axial flow transport to become prominent compared to the tangential momentum.

The evolution of the swirl number is captured in a very similar way in Mesh 1 and Mesh 2. However, in the area of higher swirl, Mesh 1 differs from the others. It is therefore seen that a change in the base mesh size affects the capture of the tangential mainly due to the higher resolution of Mesh 1 in the region of the annular fuel flow with boundary layer.

5.3.2 Variation of axial velocity in the radial direction

Figure 5.9 shows the variation of the average axial velocity over time along the radial direction at two different axial positions.

At the outlet orifice plane $z = 0$, it can be seen that the axial velocity starts at zero at the wall ($r = -150\mu m$) and then increases sharply due to the presence of the annular flow adhered to the wall, reaching values of up to around $\sim 25m/s$; these velocities provide enough momentum in the liquid to form a conical sheet that breaks into ligaments and droplets. Therefore, this value serves as a reference for subsequent simulations. As we move closer to the axial axis ($r = 0$), this velocity decreases again and even reaches negative values due to the suction of air from the air core. Also, at the throat position of the atomizer ($z = -240\mu m$), the presence of the air core can be seen due to the high negative values of this velocity. Comparing the two axial positions, it can be observed that these suction velocities are higher (in absolute value) in the throat than the velocities at the inlet orifice. This is because the air core reduces its cross-sectional area

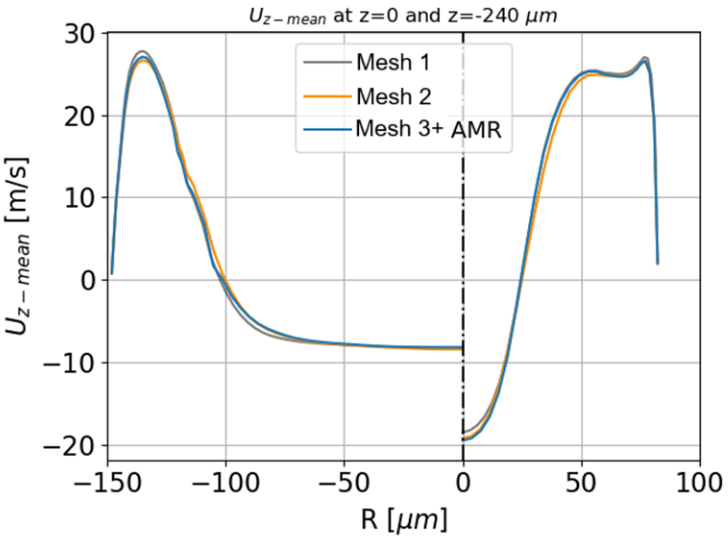

Figure 5.9: Mean axial velocity variation along the radial direction at two axial positions: the atomizer throat ($z = -240\mu m$) and the exit oriffice ($z = 0\mu m$).

as it enters the atomizer, thus increasing its velocity. On the other hand, there is a noticeable peak in $U_{z-\text{mean}}$ before it returns to zero at the wall. This is due to the simultaneous capture of the liquid boundary layer adhered to the wall and the air boundary layer adhered to the liquid.

In this case, the three meshes present very similar results in which it is difficult to distinguish any difference. Therefore, this is an example that the axial flow is captured in a very similar way between the three meshes and that the meshing parameters did not affect the results in this case.

5.3.3 Aircore size and fuel film thickness

The velocities described in the previous section are necessary for the formation of the annular flow and the air core that characterize this type of atomization. To quantify the dimensions of these flow characteristics and compare them with the proportions of the atomizer, average values of these two characteristic lengths are estimated. On one hand, the average thickness of the fuel film is calculated right at the outlet orifice ($z = 0$). This thickness is proportional to the amount of liquid being delivered by the atomizer and also quantifies the inertia of the conical sheet that is expelled towards the external region. On the other hand, the average size of the air core measured at the throat quantifies the mesh's ability to capture the formation of the air core due to the air suction caused by the depression in the center of the hollow cone. These parameters can be seen in figures 5.10a and 5.10b.

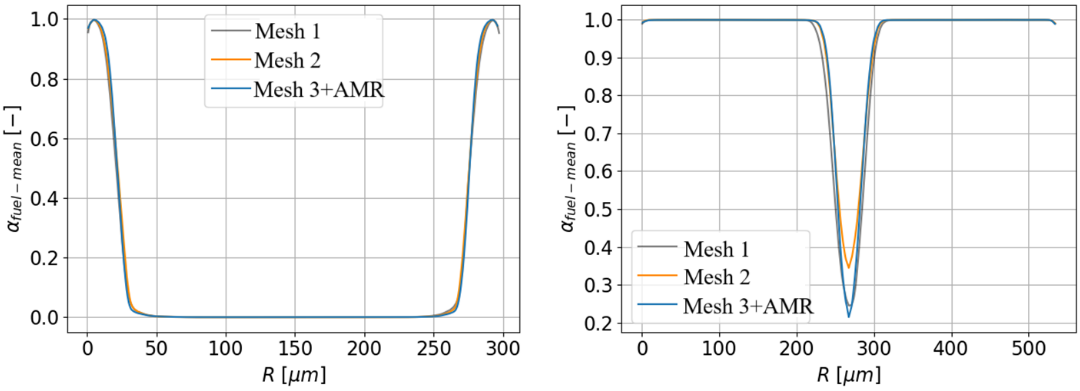

(a) (b)

Figure 5.10: Time-averaged α^{fuel} field profiles obtained in the radial direction at two different axial positions to calculate (a) the fuel film thickness at $z = 0$ and (b) the aircore diameter at $z = -240\mu m$

From the profiles in figures 5.10a and 5.10b, the sizes of the fuel film and the aircore are calculated for the value of $\alpha_{fuel-mean} = 0.5$ and these values can be seen in table 5.4.

	Mesh 1	Mesh 2	Mesh 3 + AMR
Film thickness [$\boldsymbol{\mu m}$]	17.73	23.24	22.79
$\boldsymbol{\sigma}$	2.74	0.77	0.70
Air core thickness [$\boldsymbol{\mu m}$]	46	24.61	28.35
$\boldsymbol{\sigma}$	5.49	1.29	0.73

Table 5.4: Comparison of film and air core thicknesses captured by each mesh.

The radial thickness of the fuel film at the atomizer exit is measured as the radial distance between the point in the plane $z = 0$ that has a $\alpha_{fuel-mean} = 0.5$ and the atomizer wall. The three meshes have different values for this thickness, although within the same order of magnitude, as can be seen in table 5.4, where Mesh 1 has the lowest fuel film thickness value and the highest standard deviation of the spatial average. That is, Mesh 1 captures a larger but at the same time more unstable air core. It can be observed both in figure 5.10a and in figure 5.10b, that the mesh with AMR has the lowest standard deviation of this average value, which indicates that it captures a more stable air core. In Mesh 1 there are greater deviations because greater oscillations of the free surface are captured, which are the cause of the destabilisation of the sheet and its disintegration into ligaments and drops.

The aircore diameter at the throat is measured as the radial distance between two diametrically opposite points where $\alpha_{fuel-mean} = 0.5$ is obtained. For this value, as for the fuel film thickness, Mesh 1 has a different value than the other two meshes and a greater standard deviation.

5.3.4 Study of the cloud of droplets

In this mesh sensitivity study, the droplet detection algorithm described in section 4.4 is used with a threshold value of $\gamma = 0.05$. This means that at a given instant t, all cells that satisfy $\alpha^i_{fuel} \geq 0.05$ become part of a structure, which can be either a droplet or a ligament.

Using the equations from section 4.4, the size and velocities of the droplets formed in the atomization are calculated for each instant within the averaging window. The PDF of sizes shows the probability distribution function f of volumetric diameters using probability bins of 3.56 μm. These bins indicate the likelihood of finding a droplet of size D_V within the values corresponding to bin j, i.e., $D^j_{V,\min} \leq D_V \leq D^j_{V,\max}$. The value of f is averaged over all the times within the averaging window. For each instant, there is a number of droplets that belong to each bin j, but the droplets from the same bin are summed across all times and then divided by the total number of times. This results in a time-averaged value from all the instants.

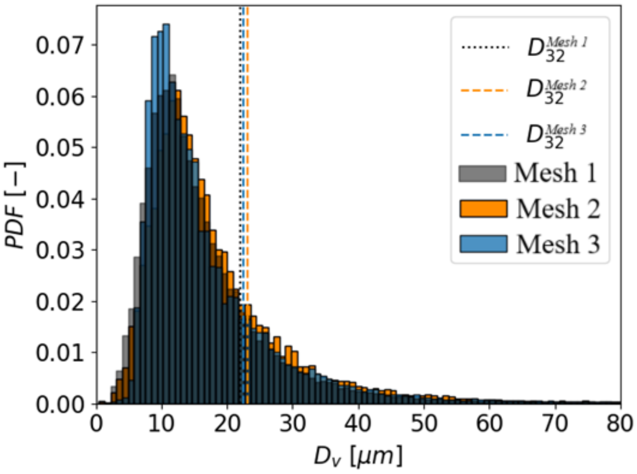

Figure 5.11: Drop sizes probability distribution computed as the volumetric diameter D_V for the entire external flow region captured with each mesh

In figure 5.11, the size distribution for each mesh is shown, representing all the droplet sizes produced on average by the atomization. It can be observed that the most probable volumetric diameters are between 10 and 15 μm. The mesh with AMR stands out as it captures a size of 10 μm as the most common size. This indicates that the AMR mesh predicts that the atomization process will produce smaller droplet sizes. All the meshes have a distribution with a Log-normal statistical distribution shape, indicating that the most probable droplet sizes are concentrated within a narrow range of values. These results demonstrate that the simplex atomization is efficient as it tends to produce a cloud of droplets with relatively uniform size.

The Surface Mean Diameter (SMD), denoted as D_{32}, is also calculated for all meshes and recorded in table 5.5. This diameter represents the droplet size that has the same ratio between volume and surface area as the entire atomized liquid, i.e., the same volume-to-surface ratio as all the liquid in all the droplets. It can be observed that all meshes have very similar values, indicating again that all meshes produce droplets of a similar average size.

	Mesh 1	**Mesh 2**	**Mesh 3**
$\mathbf{D_{32}}$ [μ**m**]	22.5	23.5	23

Table 5.5: D_{32} values for different meshes

Number of drops

In figure 5.12, the number of drops captured by each mesh over the 220 μs duration of the averaging window is shown. At each microsecond, tools were applied to determine the total number of drops at that instant. The value $nDrops$ is plotted as a function of the time advancement of the averaging window $t[\mu s]$. In this figure, it can be observed that during the initial microseconds of the simulation, Mesh 1 (the smallest base size mesh) and Mesh 3+ AMR capture more drops than Mesh 2, which has a larger base size. However, it is also seen that the mesh with AMR surpasses in number of drops captured by the other two meshes for the rest of the temporal averaging interval starting from 75 μs. Additionally, this mesh captures approximately 150% more drops than the mesh with the smallest base size, Mesh 1. This ability to capture drops by the mesh with AMR is due to the dynamic meshing algorithm, AMR, being able to break up drops into even smaller drops even in areas where there is no local refinement. In simulations with meshes that do not have AMR, if a drop exits the areas of local refinement, then due to the larger cell size, the drop will not be divided into smaller drops. However, in the mesh with AMR, there is refinement in areas where there is no local refinement, resulting in a greater number of captured drops.

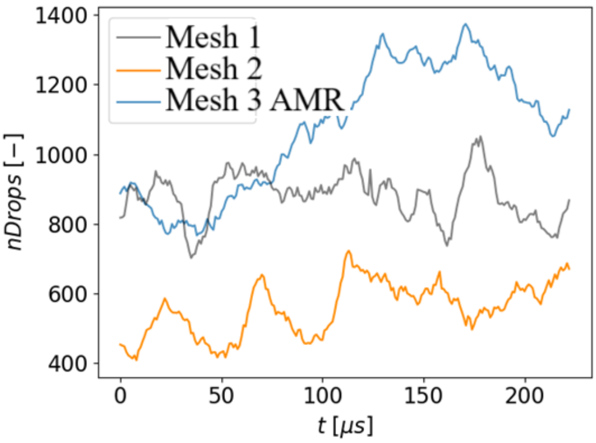

Figure 5.12: Number of drops in the entire domain counted for each instant by each mesh within the averaging window.

5.3.5 Statistical description of droplet velocities

Figure 5.13 shows the PDFs of the velocity components of each drop captured by the meshes. The PDFs of the axial velocity component U_z and tangential velocity U_θ show that Mesh 1 and Mesh 2 have similar distributions of these components and therefore overlap. In contrast, Mesh 3 + AMR tends to show more open distributions with a considerable probability distribution at low and zero values of these velocity components, indicating that several of the drops captured by this mesh are moving at low velocity or near rest. These results are likely due to the fact that simulations with AMR are implemented based on simulations without dynamic meshing. This means that when mapping the results from a simulation without dynamic meshing, data from drops that have exited the local refinement zone and have slowed down are mapped. Starting from this data, the mesh with AMR breaks down these drops into smaller drops, which increases the number of drops with low velocity.

The low speed drops captured by the AMR mesh are defective results and it is interesting to discard them from the study of the drop cloud because they are drops that, in addition to

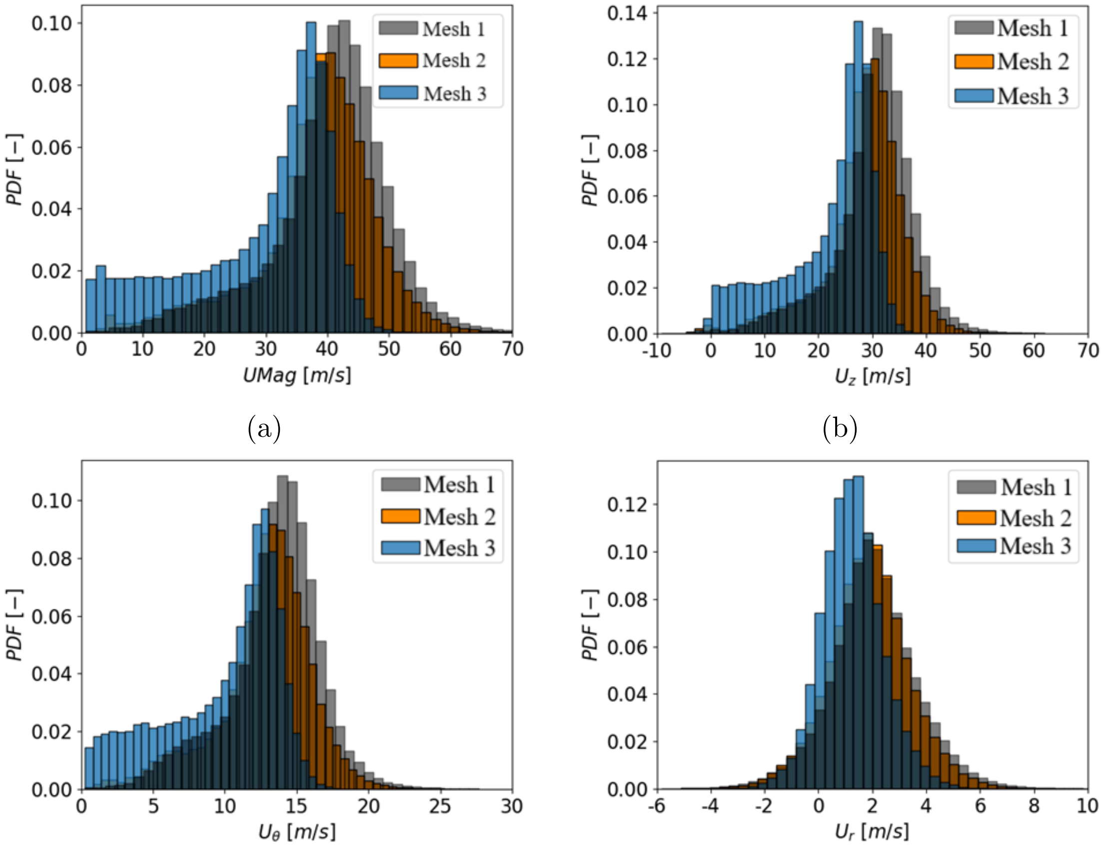

(a) (b)

(c) (d)

Figure 5.13: PDF of the velocity components of all the droplets forming in the entire domain of the outer region (a) Velocity magnitude (b) Axial component (c) Tangential component (d) Radial component

being slowed down by the mesh and not by a physical reason of the flow, are located in areas that are not of interest for the study, such as in areas close to the exit boundary where there are more drops that leave the local refinement region and are slowed down. This conclusion can be corroborated by looking at the probability distributions of the velocity components in axial planes in which the drops and their velocities are recorded during the entire averaging window. These PDFs are shown in figure 5.14. And in this same figure it can be seen that in these axial positions there is no such distribution of drops with low axial and tangential velocity, but rather these drops correspond to areas that are not of interest, that is, areas close to the boundaries.

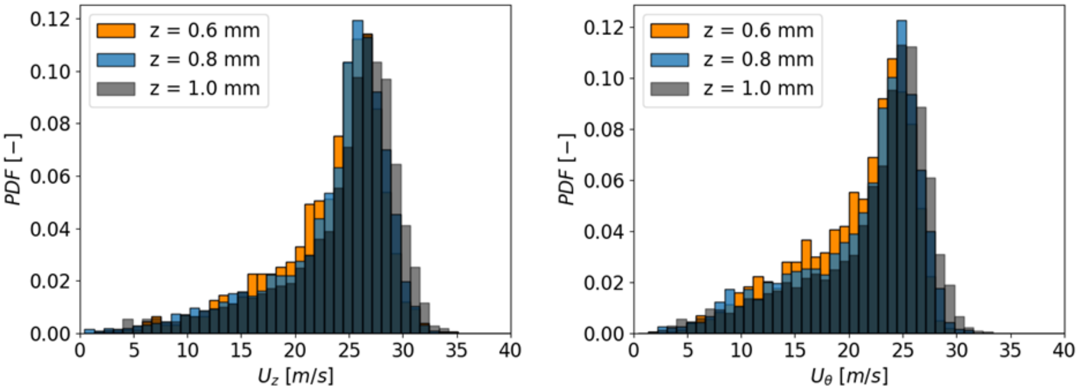

(a)

(b)

Figure 5.14: PDF of the axial (a) and tangential (b) velocity components of the drops passing through planes at axial positions during the simulation with Mesh 3+AMR

5.4 Selecting the meshing strategy

After performing the qualitative and quantitative comparison of the three meshes studied, it can be seen that the mesh with AMR type dynamic mesh, although it has much fewer cells, achieves the same or better performance in terms of capturing the disaggregation of the spray into ligaments and drops. In fact, it is the mesh that captured the most drops in the averaging window. Although with respect to the other meshes, the computational cost in h/ms is higher in the AMR mesh, this mesh remains in the same order of magnitude of cost as the other meshes. In addition, by having a considerably smaller number of cells compared to the other meshes, this mesh saves computational costs of memory storage and post-processing since it generates lighter results due to having many fewer cells. Thanks to AMR meshing, the results of this mesh describe the interface phenomena and surface oscillations with the same resolution as the other meshes, but by having fewer cells in areas where these types of phenomena do not occur, the data is much lighter to store and process.

Chapter 6

Parametric study

Parametric StudyIn this chapter, the results obtained from four simulations are described. Each one corresponds to the atomization of a given fuel. For the four simulations, all the physics of the problem: type of flow, initial and boundary conditions, turbulence modeling and all the numerical configuration, corresponds to the configuration already described in chapter 4, in the description of the reference case. What distinguishes each simulation in this study chapter, is the combination of physical properties of the liquid fuel used in each one of them. Each combination corresponds to the properties of a specific fuel. One of these four fuels corresponds to a SAF fuel type HEFA-SPK.

The physical properties that distinguish the four fuels are: the liquid density ρ, the dynamic viscosity ν and the surface tension σ. The value of these properties for each of the four fuels can be seen in table 6.1. The first fuel corresponds to the theoretical monocomponent fuel n-heptane, which has already been described in chapter 4 and has also been used in the mesh sensitivity study. Its properties correspond to the theoretical properties of the fuel at room temperature (298 K). The second fuel also corresponds to n-heptane, but its properties correspond to the theoretical properties of this fuel at high temperature (350 K). The simulation with this fuel is implemented to verify that the computational model is sensitive to changes in the physical properties of the fuel. Once it was verified that the model is sensitive to changes in physical properties, simulations were carried out for the following two fuels: kerosene and SAF. The third fuel is conventional kerosene, a sample was taken and its properties were obtained through the laboratory services of the Intertek company [32] as part of the project mentioned in chapter 1: 'Modelling of sustainable aviation fuel for low emissions. Atomization' (SAFLOW-BREAK). The fourth and last fuel is the SAF type. This fuel corresponds to the SAF family Hydro Processed Esters and Fatty Acids Synthetic Paraffinic Kerosene, (SAF HEFA SPK), and has been described in chapter 1. Its properties, as for kerosene, were measured at Intertek.

Property	n-Heptano	n-Heptano HT	Kerosene	SAF
ρ [kg/m^3]	681.7	634.3	797.55	758.31
ν [m^2/s]	$5.671 \cdot 10^{-7}$	$3.67 \cdot 10^{-7}$	$1.477 \cdot 10^{-6}$	$2.145 \cdot 10^{-6}$
σ [N/m]	0.0197	0.0145	0.0283	0.02485

Table 6.1: Physical properties of each of the four fuels

The dimensionless numbers Reynolds, Weber, and Ohnesorge are fundamental in the study of atomization processes. These numbers provide insights into the flow characteristics and behavior of fluids.

The Reynolds number (Re) is a measure of the ratio of inertial forces to viscous forces within a fluid. It is calculated as:

$$\mathrm{Re} = \frac{\rho v D}{\mu} \tag{6.1}$$

- ρ: Density of the fluid (kg/m^3)
- v: Velocity of the fluid (m/s)
- D: Characteristic diameter (m)
- μ: Dynamic viscosity of the fluid (Pa·s)

The Weber number (We) quantifies the ratio of inertial forces to surface tension forces and is expressed as:

$$\mathrm{We} = \frac{\rho v^2 D}{\sigma} \tag{6.2}$$

- ρ: Density of the fluid (kg/m^3)
- v: Velocity of the fluid (m/s)
- D: Characteristic diameter (m)
- σ: Surface tension of the fluid (N/m)

The Ohnesorge number (Oh) is a measure of the ratio of viscous forces to the combined inertial and surface tension forces, and is calculated as:

$$\mathrm{Oh} = \frac{\mu}{\sqrt{\rho \sigma D}} \tag{6.3}$$

- μ: Dynamic viscosity of the fluid (Pa·s)
- ρ: Density of the fluid (kg/m^3)
- σ: Surface tension of the fluid (N/m)
- D: Characteristic diameter (m)

In this study, the physical properties in table 4.2 together with a reference velocity (v) of 10 m/s and a reference diameter (D) of 0.0003 m, were used for calculations of a first estimation o these dimentionless goups and their values are shown in table 6.2

Fuel	Re	We	Oh
n-Heptane	5290.07	1038.12	0.0061
n-Heptane HT	8174.39	1312.34	0.0044
Kerosene	2031.14	845.46	0.0143
SAF	1398.60	915.46	0.0216

Table 6.2: Dimensionless numbers of the fuels

The results described in this chapter are obtained from data extracted at various times from each of the solutions of the numerical simulations. Data are extracted from each numerical solution with the same frequency ($1\mu s$) to obtain a temporal data window of the simulation (a total of $140\mu s$). The extraction of these data begins once the atomization simulation has entered a stable state, that is, once the spray has formed in the form of a conical sheet and the drops have reached the exit boundary which is at 3.3 mm and once the air core has stopped penetrating in the downward axial direction.

6.1 Qualitative analysis

6.1.1 Appereance of the spray

In this section, we compare how each simulation of each fuel captures the formation of the conical sheet and how it disintegrates into ligaments and droplets. To do this, we first use visualizations of the isosurface of the volumetric fraction field $\alpha_{fuel} = 0.5$. The three-dimensional representation of these isosurfaces is obtained for an instant of the simulation in which a steady state has been reached, that is, for one of the final instants of the averaging window.

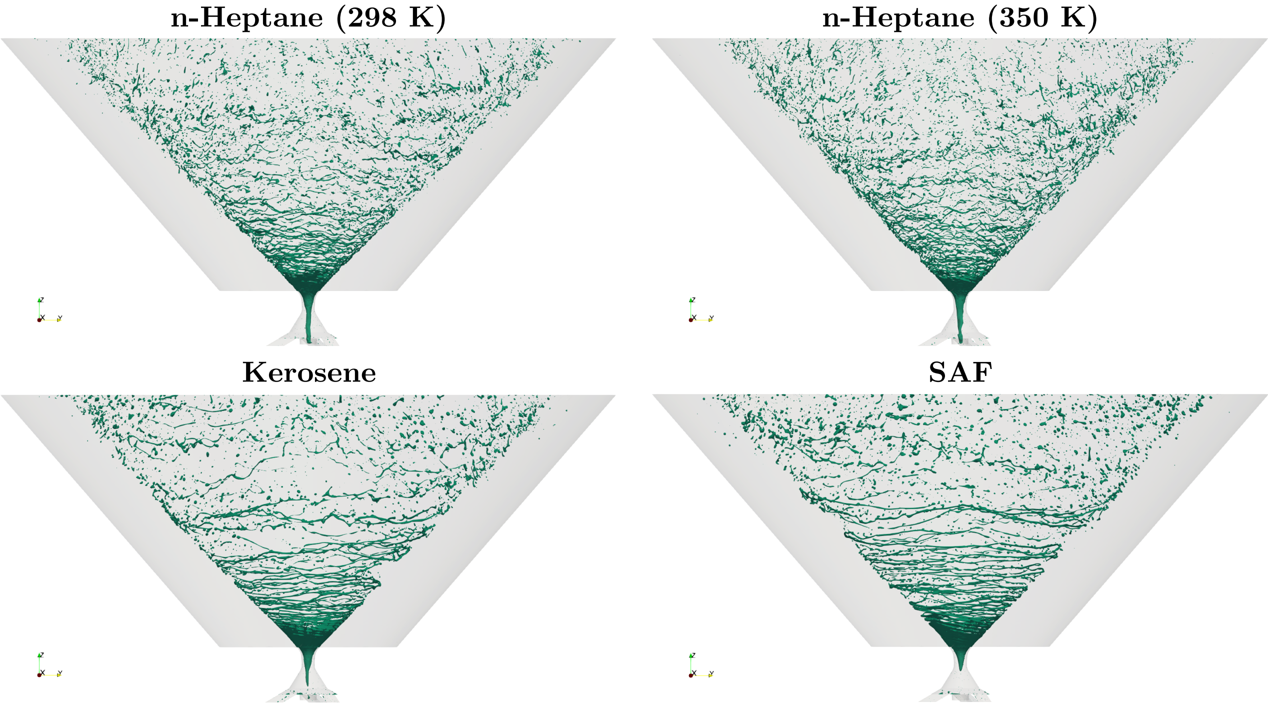

n-Heptane (298 K)

n-Heptane (350 K)

Kerosene

SAF

Figure 6.1: Visual representation of the instantaneous atomization interface obtained from the isosurface $\alpha_{fuel} = 0.5$

At first glance, in Figure 6.1, heptane at room temperature and heptane at high temperature are very similar. However, when comparing the results of this theoretical fuel with real fuels (kerosene and SAF), several notable differences can be seen. As shown in Figure 6.1, kerosene and SAF form a conical sheet with greater penetration length and at the same time disintegrate into thicker ligaments that have greater reach (compared to heptane at both temperatures). These ligaments also travel and remain intact over longer distances than the ligaments formed in the atomization of heptane. This means that, in kerosene and SAF fuels, the fragmentation of ligaments into droplets occurs at a much farther axial distance than seen in heptane at both temperatures. This formation and behavior of ligaments in kerosene and SAF fuels also cause their droplet clouds to have visually fewer and larger droplets compared to those formed in the atomization of the single-component fuel n-heptane. This implies that the atomization of these latter two fuels is worse than that of heptane at both temperatures. This is due to their low Re as viscous forces prevent inertial forces from disintegrating the fuel sheet. Also, due to their low We, the effects of inertial forces are not as high relative to the effects of their surface tension forces as is the case with heptane at both temperatures.

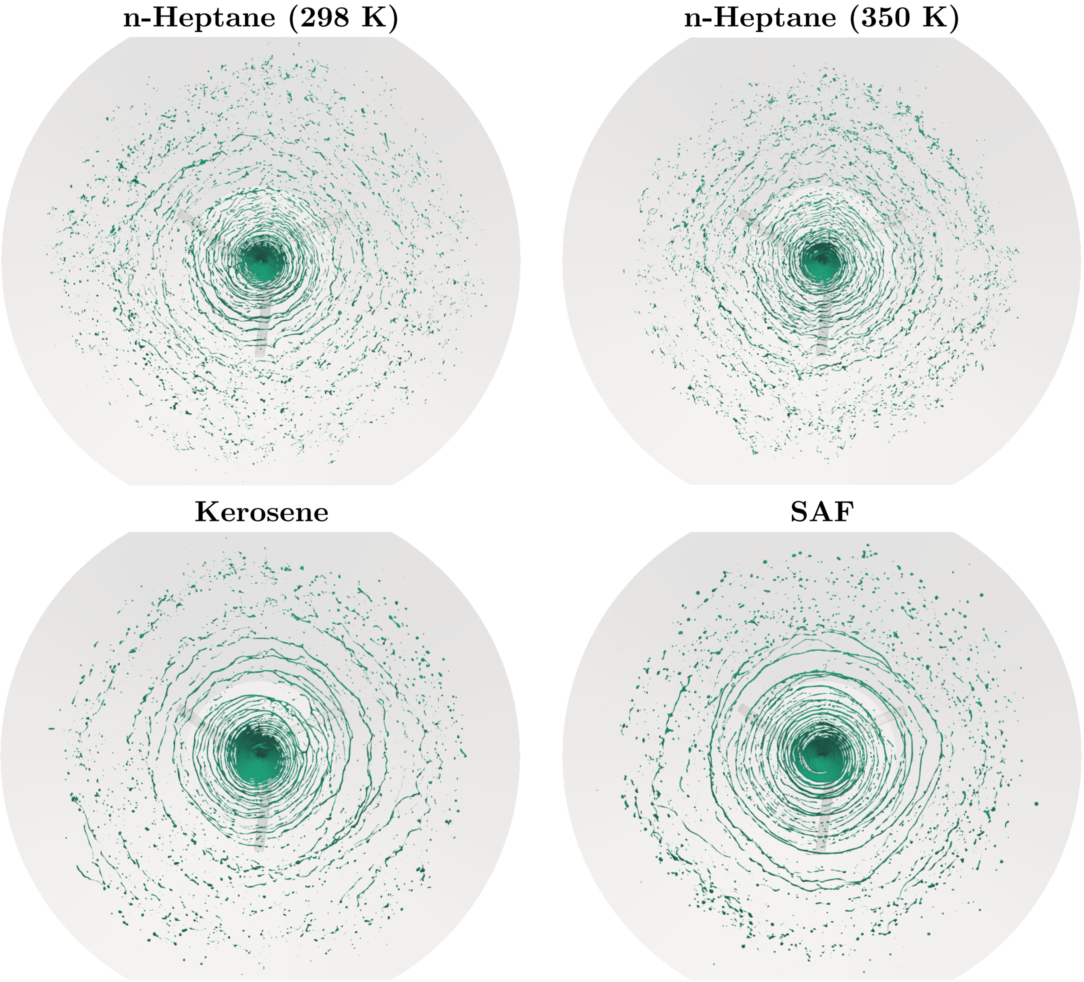

Figure 6.2: Visual representation of the instantaneous atomization interface obtained from the isosurface $\alpha_{fuel} = 0.5$

Another observation that can be made at first glance from the isosurfaces in Figure 6.1 is the penetration of the air core obtained in each fuel. For both cases of heptane (at 298 K and 350 K), it can be seen that the air core penetrates as far down as possible into the injector. And, in these two same cases, the deeper the air core penetration, the more irregular the surface becomes, indicating increasing instability. In contrast, in the case of kerosene, the air core does not reach the bottom of the injector cylinder but collapses a little earlier and, in fact, has an abrupt reduction in diameter in the area near the throat. In the case of SAF, the air core also does not penetrate to the bottom of the injector but collapses a little below the throat. This behavior of the air core for kerosene and SAF can be explained by the mass flow boundary condition at the inlet boundary of the input ports. Since the same mass flow is defined for all four simulations, the velocity at which the flow enters changes for each fuel because each has a specific density. Each fuel adapts its injection velocity based on its density to meet the mass flow rate of the inlet boundary condition. The higher density of kerosene and SAF compared to the densities of heptane results in a lower injection velocity for these two fuels. A lower injection velocity at the inlet generates less swirl and therefore less centrifugal inertia of the flow in the swirl chamber, which hinders the formation of the air core, increases the thickness of the fuel film, and thus results in poorer atomization.

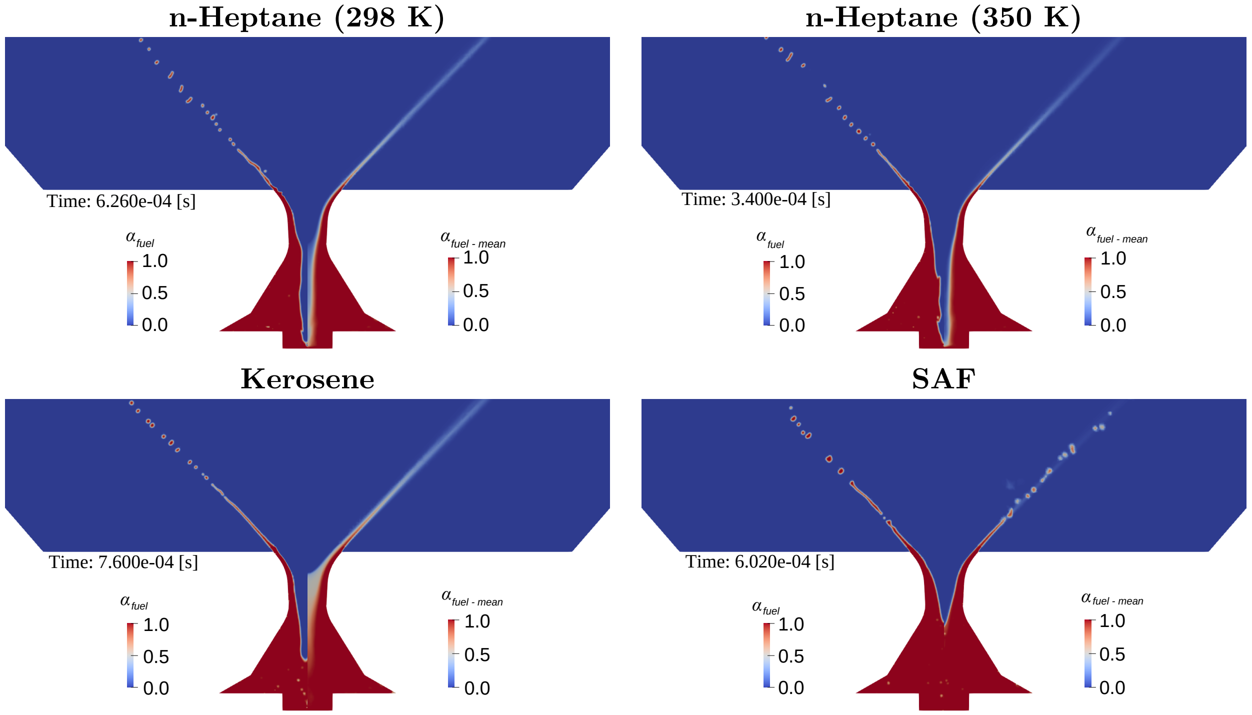

Figure 6.3: Section view over the yz plane of the fuel volume fraction field both instantaneous and time averaged fields. Within each subfigure: en la mitad de la izquierda el campo instantáneo y en la mitad de la derecha el campo promediado en el tiempo

In Figure 6.3, a sectional view of the liquid volumetric fraction field can be seen. This sectional view shows in detail the internal flow within the spin and swirl chambers so that the formation of the air core, the formation of the annular flow, and the conical sheet that disintegrates into ligaments and droplets can be appreciated. For the cases of n-heptane at 298 K and 350 K, it can be seen that the time-averaged field in the air core area is not very diffuse because its oscillations have not been very strong during the averaging window of 140μs, meaning that the air core has remained stable. In the kerosene figure, it can be seen that the instantaneous field and the averaged field do not share much symmetry in the air core area, which indicates that in this fuel the air core oscillates quite a bit relative to its average value. This can also be seen in the averaged field $\alpha_{fuel-mean}$ of Figure 6.4, where it is shown that the annular flow has a radius that has changed. These kerosene results may also be due to the fact that the values of the $\alpha_{fuel-mean}$ field have not only been calculated in the averaging window but also include the values from the initiation simulation of air core formation.

In Figures 6.3 and 6.4, the instantaneous fields α_{fuel} of Kerosene and SAF show that both have an annular flow at the outlet orifice with much greater thickness than the heptane simulations. Additionally, both Kerosene and SAF have much less pronounced oscillations on the free

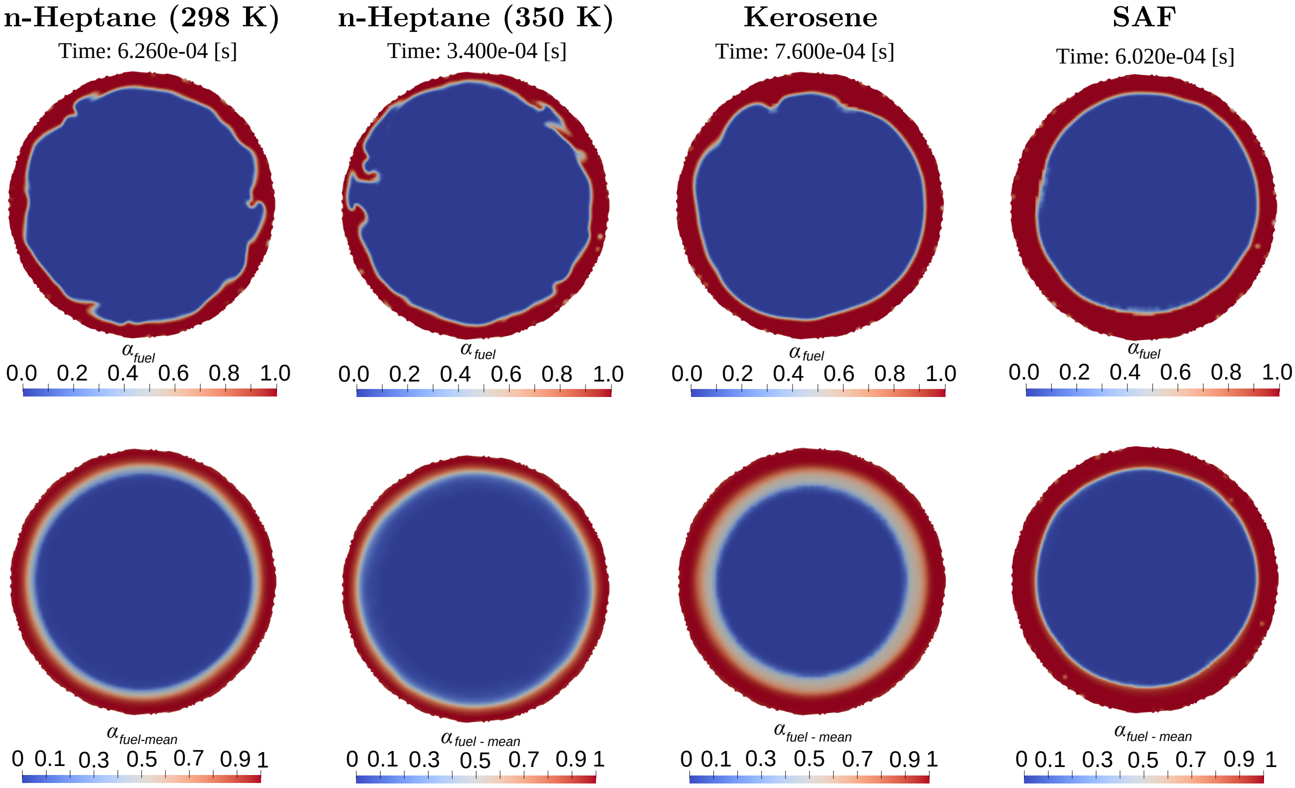

Figure 6.4: Instantaneous and time averaged fuel volumetric fraction α^{fuel} contours on the $z = 0$ plane for the different fuels

surface compared to heptane. These results show how fuels with higher density and viscosity dissipate free surface oscillations more intensely and tend to keep it cohesive. At the same time, these fuels, kerosene and SAF, have higher surface tension, which also explains why much thicker and longer ligaments form, traveling greater distances without breaking compared to heptane. These low oscillations on the surface of kerosene and SAF also show why the conical sheet forms ligaments that remain cohesive over much larger circumferential sectors than in heptane.

6.1.2 Qualitative description of the velocity field

In figure 6.5, the instantaneous and time-averaged scalar fields of the velocity magnitude can be seen. The color scale of the figures shows at a glance that higher velocity magnitudes are obtained in the simulations of the monocomponent fuel, n-heptane at high temperature. As mentioned before, this result is due to the higher density of kerosene and SAF fuels, which reduce the injection velocity at the inlet of the inlet ports to maintain the value of the mass flow imposed in the boundary condition. As in the mesh sensitivity study, it can be seen that the highest velocity magnitudes are reached in the annular flow after the injector throat, where the flow reduces its cross-sectional area to the maximum and, being an incompressible flow, increases its velocity to the maximum.

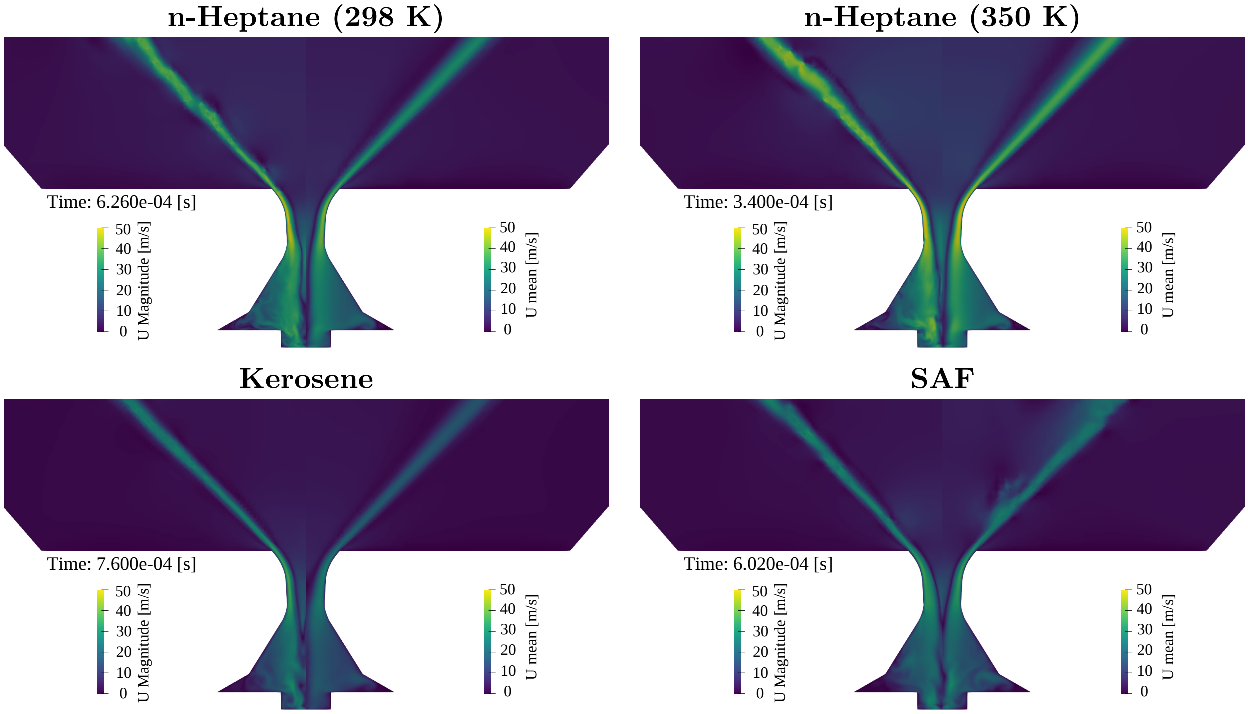

Figure 6.5: Section view over the yz plane of the velocity magnitude, both instantaneous and time averaged fields. Each subfigure represents one of the fuels (see subfigures titles).

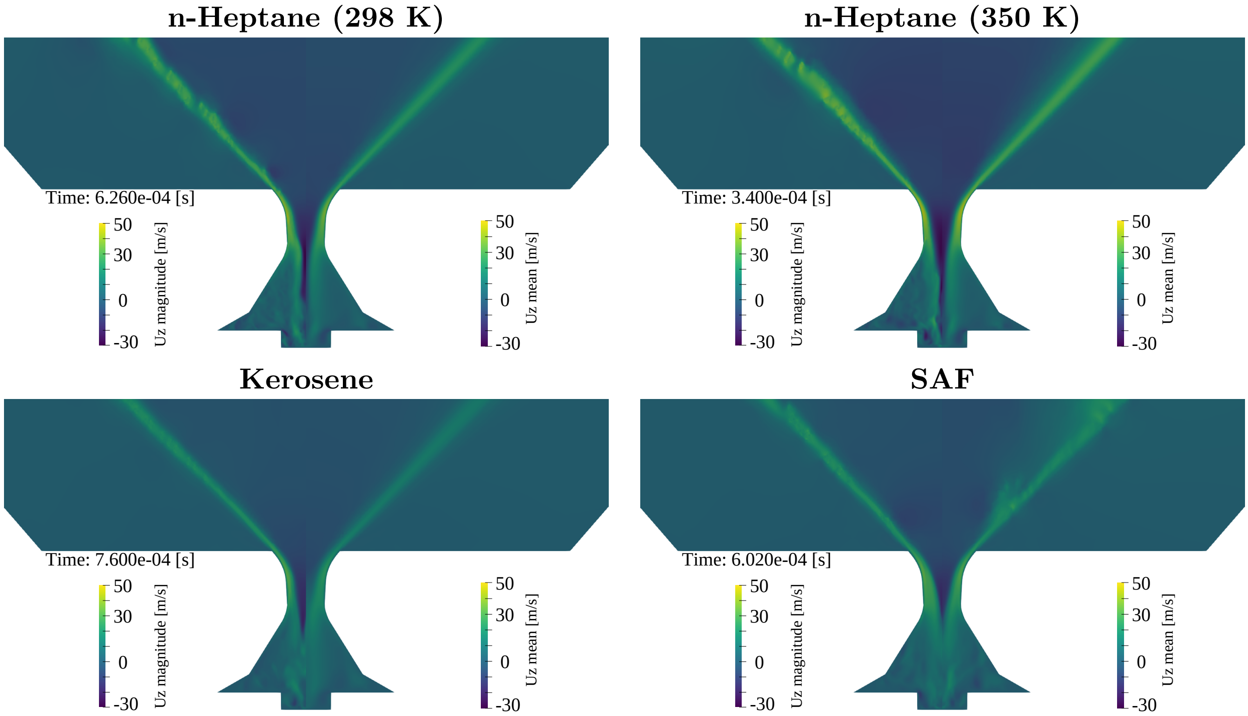

Figure 6.6: Section view over the yz plane of the axial velocity, both instantaneous and time averaged fields. Each subfigure represents one of the fuels (see subfigures titles).

It can be seen that the maximum velocities in heptane reach 50 m/s, while the maximum velocities of kerosene or SAF barely reach 40 m/s. High values of the velocity magnitude can be seen in the cylinder area, i.e. in the lowest part of the injector, around the lowest part of the air core. In order to check which velocity components cause the magnitude to increase in this area, each component must be analyzed separately as is done in the quantitative analysis section below. In figure 6.6 the fields of the instantaneous and average axial component U_z can be seen. It can be seen that this component is the one that has the greatest contribution to the maximum flow velocities in the annular flow area before the exit orifice.

In figure 6.6, it can also be seen how the axial component is close to zero in the area of highest swirl; inside the swirl chamber before the throat, where the velocity is mainly tangential and radial. On the other hand, in the aircore area, the sucked air flow causes this component to have high negative values. Because each fuel has a different aircore penetration length, then it can be seen that the negative heats of the axial component are proportional to this aircore penetration length.

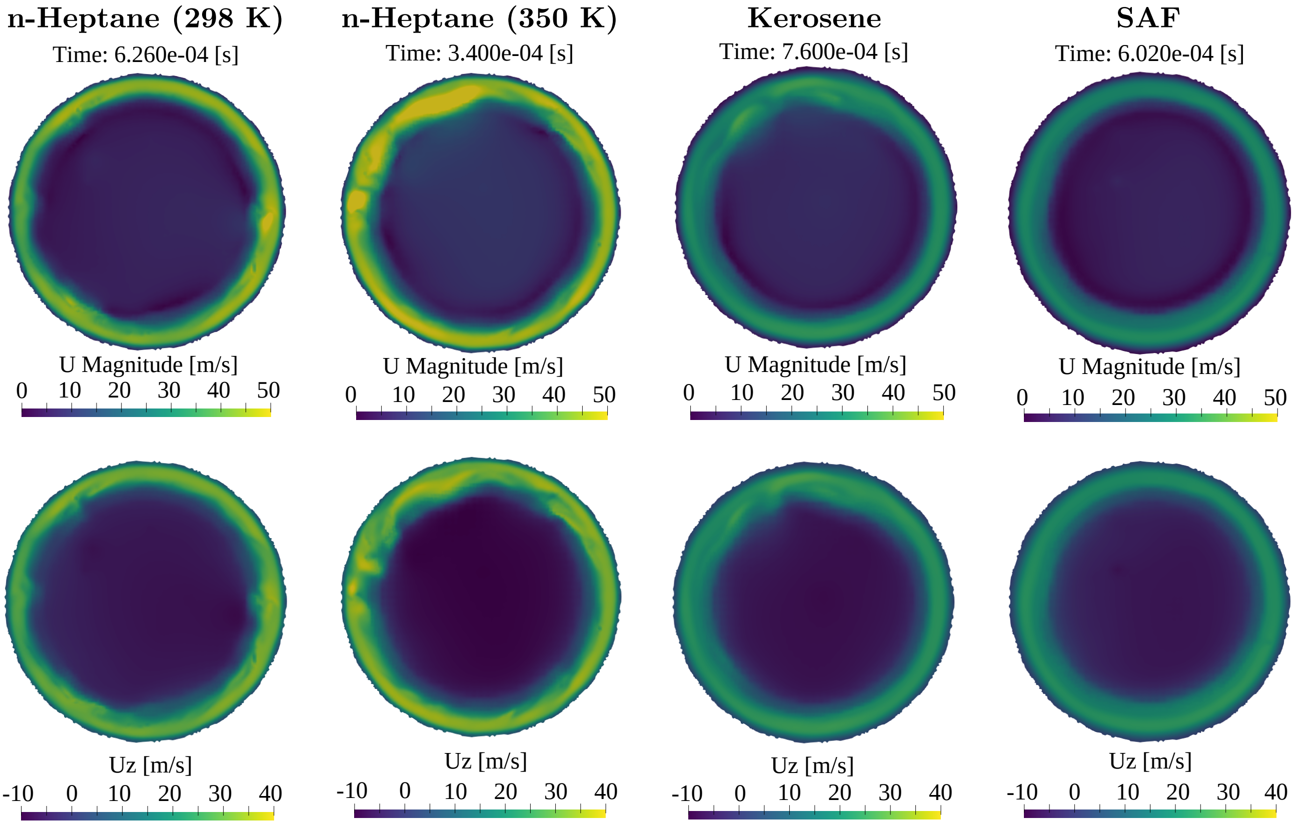

Figure 6.7: Instantaneous velocity and axial component magnitudes contours on the $z = 0$ plane for the different fuels

In Figure 6.7, it can be seen that, in the region of the outlet orifice, the component that contributes the most to the magnitude of the velocity is the axial component U_z. In this figure, once again, thanks to the color scale, it can be appreciated how kerosene and SAF fuels reach significantly lower axial velocities than the axial velocities of the single-component fuel. It can be observed that, since heptane at high temperature has the lowest density of all fuels, it is the fuel that reaches higher velocities when expelled through the outlet orifice. SAF, on the other hand, despite having lower density than kerosene, shows lower axial velocities. To determine which fuel generates greater axial momentum flow, the behavior of the swirl number described later must be observed.

6.2 Quantitative analysis

6.2.1 Swirl number

Para describir para cada combustible el desempeño del atomizador en función del número de swirl S, (definido en la ecuación 2.3), se comparan aquí las curvas de evolución de S vs posición axial. Cada curva muestra cuánto swirl se imparte al flujo en cada posición axial respecto al momentum axial disponible en esa misma posición axial. La figura 6.8 muestra este ratio calculado a partir del campo de velocidad promediada en el tiempo durante la ventana de 140μs y de sus componentes axial U_z y tangencial U_θ.

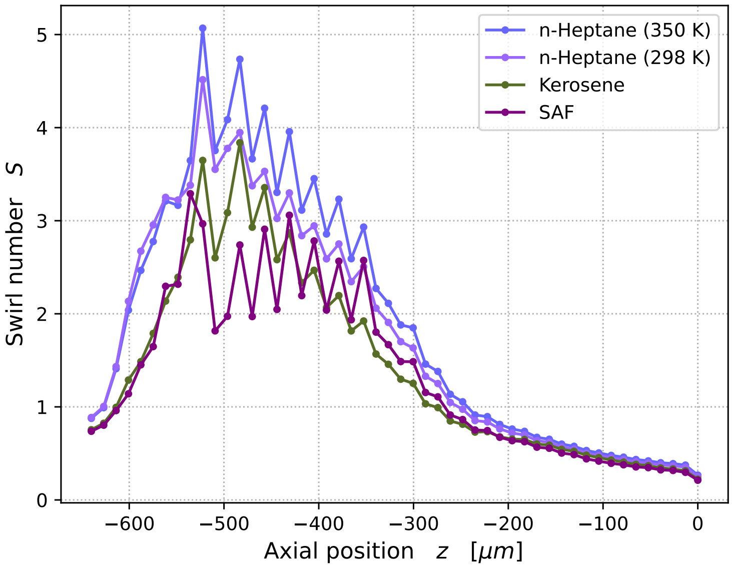

Figure 6.8: Swirl number evolution along the axial position for each fuel

Since all four fuels are being injected into the same atomizer with the same geometry and dimensions, and also with similar injection rates, then all four fuels exhibit the same trend in swirl number along the axial direction within the atomizer. This trend was also described in the mesh sensitivity study, and shows that the swirl imparted to the flow is greater where there are larger diameters in the swirl chamber and is lower as the flow acquires higher axial velocity as it approaches the exit orifice.

When comparing the four fuels, it can be observed that high temperature heptane is the fuel that generates the highest swirl numbers in the injector. This is mainly due to the higher injection rates obtained for this less dense fuel, as can be seen in figure 6.5. These injection rates at the inlet are determined by the density of the fuel and by the value of mass flow imposed in the boundary condition.

The fact that the swirl number increases for higher injection velocities indicates that the atomizer favors tangential transport. This is understood because the swirl number, S, being a ratio between tangential and axial momentum, intuitively one might believe that an increase in injection velocity would not affect this relationship, but instead, it is observed that increasing the injection velocity increases the swirl numbers. This implies that an increase in injection velocity does not equally favor axial and tangential transport but rather favors tangential transport to a greater extent. This suggests that at higher injection velocities, the flow within the swirl chamber will have greater swirl, thus predominantly favoring the formation of the air core, which has already been qualitatively observed and will be quantitatively verified later.

Now, besides injection velocities, the properties of each fuel also influence the swirl number. In the case of SAF, due to its lower injection velocities, it will have lower axial velocities, which increases the swirl number. However, being a more viscous fluid than the other fuels, it will have lower tangential velocities because the flow will resist rotation more strongly due to the shear stresses produced by viscosity.

The oscillations of this parameter in the axial positions between -550 μm and -350 μm are probably due to the flow fluctuations in the air core zone.

6.2.2 Average axial velocity

In the simplex atomization of this study, the liquid velocity is determined by two components: the tangential component, which allows the liquid to acquire centrifugal inertia to form a hollow cone, and the axial component, which determines the reach and penetration of the spray. In this section, the time-averaged value of the axial component U_{z-mean} along the radial direction is studied in two axial planes of the atomizer, which can be seen in Figure 6.9 and are described below.

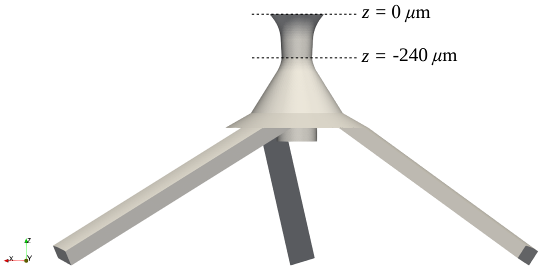

Figure 6.9: Axial planes over wich the mean axial velocity component U_{z-mean} is studied along the radial direction r.

- Outlet orifice plane: corresponds to the position $z = 0$ μm. In this plane, the fuel is already in an annular flow and from here, it will be expelled as a conical sheet towards the external flow region.
- Atomizer throat plane: $z = -240$ μm. This plane corresponds to the narrowest section of the atomizer. In this zone, there is also annular flow for all fuels due to the air core that axially penetrates into the internal flow region.

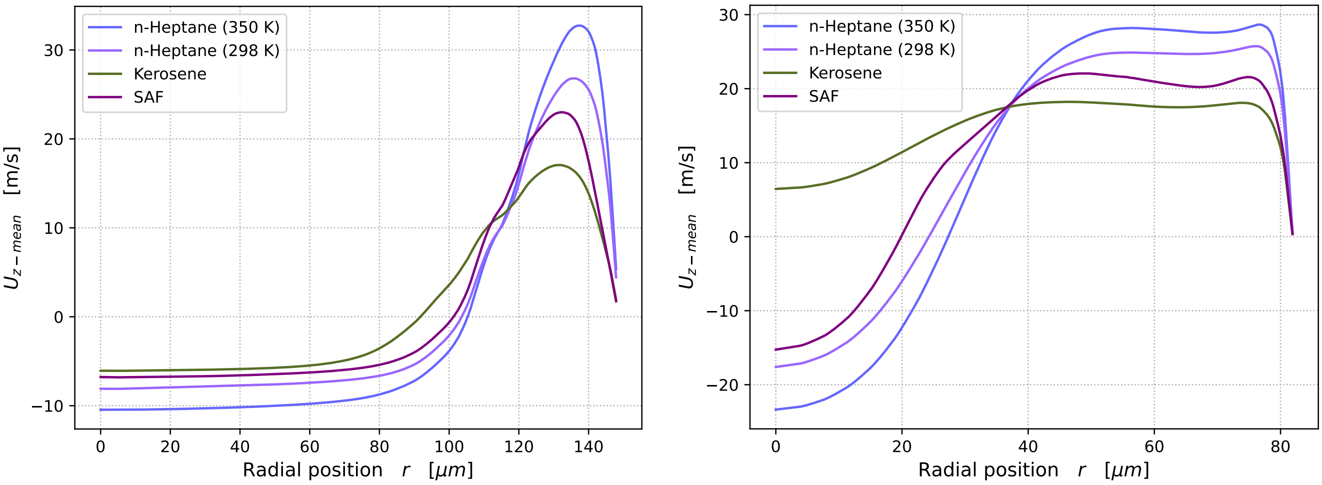

(a) Plane $z = 0$ μm

(b) Plane $z = -240$ μm

Figure 6.10: Evolution of the spatial average (over the azimutal coordinate) of the aircore radius along the z axis for different instants.

As seen in Figure 6.10a, in the outlet orifice plane ($z = 0$ μm), the profile of the axial component U_{z-mean} along the radius of the orifice has the same evolution shape for all four fuels. It can be observed that this component has both positive and negative magnitudes, which is due to capturing the velocities of the flow exiting towards the external region ($U_{z-mean} > 0$), as well as the negative velocities ($U_{z-mean} < 0$) of the air flow penetrating into the internal flow region, forming the air core. At $r = 0$, velocities are negative due to the air core, gradually increasing in magnitude until becoming positive. For the case of high-temperature heptane, axial velocities reach up to ($U_{z-mean} > 30$) m/s.

Just as air enters the atomizer due to the negative components of velocity, it can be verified that air also exits the atomizer. The positive values of this component not only correspond to liquid flow but also indicate outward airflow with positive components from the atomizer. This is confirmed by later observations showing that the average radius of the air core at the outlet orifice reaches values of approximately ~ 130 μm. Additionally, in Figure 6.10a, it can be seen that for all fuels, there are positive values of this axial component for radial positions $r < 130$ μm, demonstrating that air enters the atomizer at positions close to $r = 0$ μm but exits the atomizer attached to the liquid flow at radial positions $r > 110$ μm.

In Figure 6.10a, it can be observed that as we approach the edge of the outlet orifice ($r = 150$ μm), after reaching the peak of the curves, the axial velocity drops back towards zero. This decrease in velocity illustrates the velocity profile of the boundary layer of the liquid fuel flow that adheres to the atomizer wall until just before being expelled into the external flow region. On the other hand, Figure 6.10b also shows the velocity profile of the liquid boundary layer in all fuels for radial positions $r > 70$ μm and for radial positions $r < 70$ μm. Additionally, the airflow adhered to the liquid flow can be observed with positive values $U_{z-mean} > 0$, and with negative values $U_{z-mean} < 0$ in radial positions $r < 20$ μm approximately, due to the airflow entering the atomizer.

These graphs show that for both the airflow entering and exiting the atomizer and the liquid flow exiting the atomizer, the least dense fuel exhibits higher absolute values in the magnitudes of this axial component, namely, high-temperature heptane. And in terms of densities, from the least dense to the most dense fuel, these curves of the axial component are positioned accordingly, aligning with the previously discussed analysis related to the injection velocity determined by the boundary condition.

It is interesting to note in Figure 6.10b how the curves of the four fuels converge at a single point to reverse the order of the axial component magnitudes. This indicates that at the throat, regardless of the fuel properties, there exists a radial position where the denser fuel starts to have higher axial velocities and the less dense one has lower magnitudes of this component.

6.2.3 Air core radius

Here, the behavior of the air core formed in the internal flow region of the injector is described. This is done by analyzing the evolution of its size along the axial direction z. To do this, the data processing explained in section 4.4 is applied. Through this averaging method, the points of the curve representing the evolution of the average radius of the air core at different axial positions are obtained. In figure 6.11, for certain instances of the time window (t_1, t_2, …, t_7), the curves representing the evolution of the spatial averages of this radius, $\overline{R}^{p,k}$ from equation 4.8, are plotted against the axial position. Through these curves, the average value of the air core radius at each axial position and at different instances during the simulation can be observed and quantified. In these curves, as they represent average values, the standard deviation of the average is simultaneously shown by a shaded area above and below the curve, which is proportional to the value of this deviation.

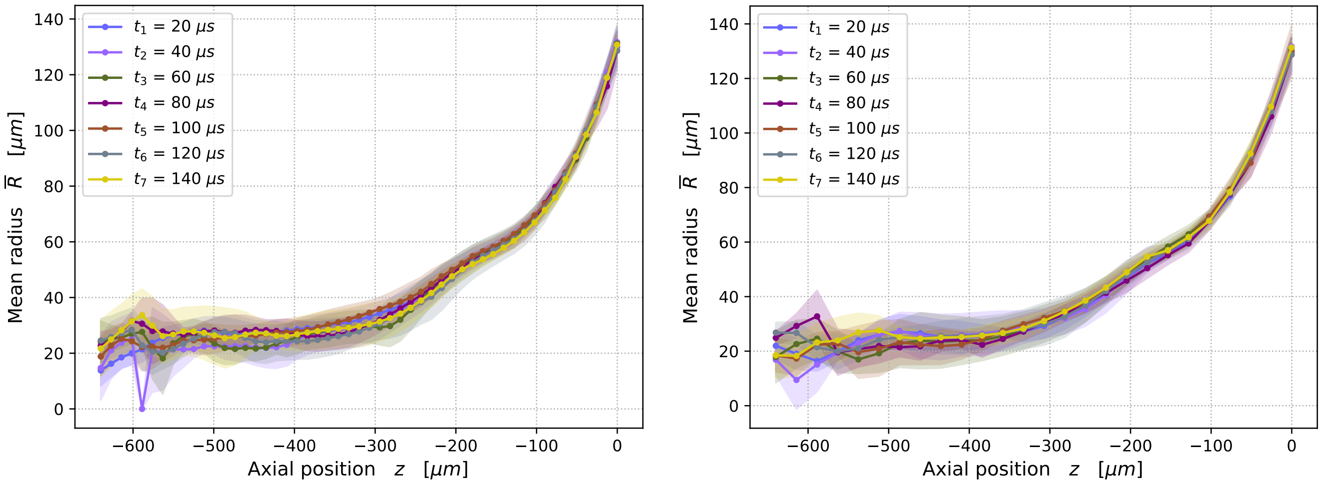

(a) n-Heptane (298 K)

(b) n-Heptane (350 K)

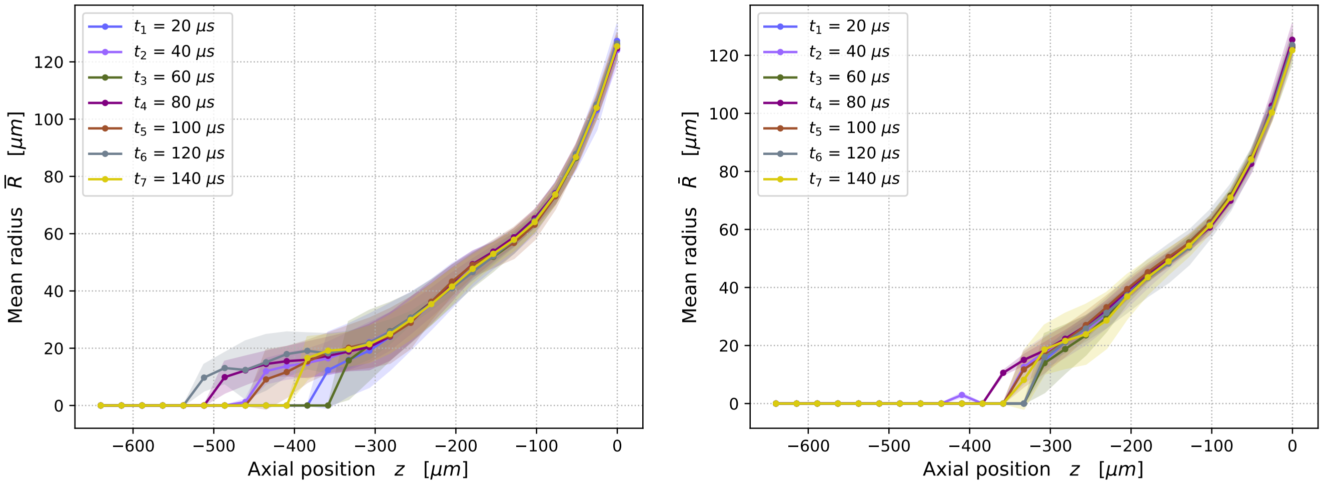

(c) Kerosene

(d) SAF

Figure 6.11: Evolution of the spatial average (over the azimutal coordinate) of the aircore radius ($\overline{R}^{p,k}$ in eq. 4.8) along the z axis for different instants. The shaded area above and below each curve represents the standard deviation ($\sigma_R^{p,k}$ in eq. 4.9) of the calculated averages.

The curves of spatial averages for the instances $t_1, t_2, \ldots, t_7$ in figure 6.11 show how similar the spatial averages are for the same fuel across different instances of the temporal averaging window. For all fuels, it can be observed that these curves overlap with each other, at least for the majority of the z axis. This indicates that during the temporal window, the air core radii have remained stable or oscillating around an axial position. This, in turn, justifies studying a single curve of temporal averages ($\overline{\overline{R}}^{k}$ from equation 4.10), which results from averaging all the curves of spatial averages from all instances of the averaging window, as shown in figure 6.12. Thanks to these curves, it can be seen that for all fuels, the lower part of the air core is much more unstable, and its radius fluctuates sharply compared to the axial positions closer to the outlet orifice ($z = 0$).

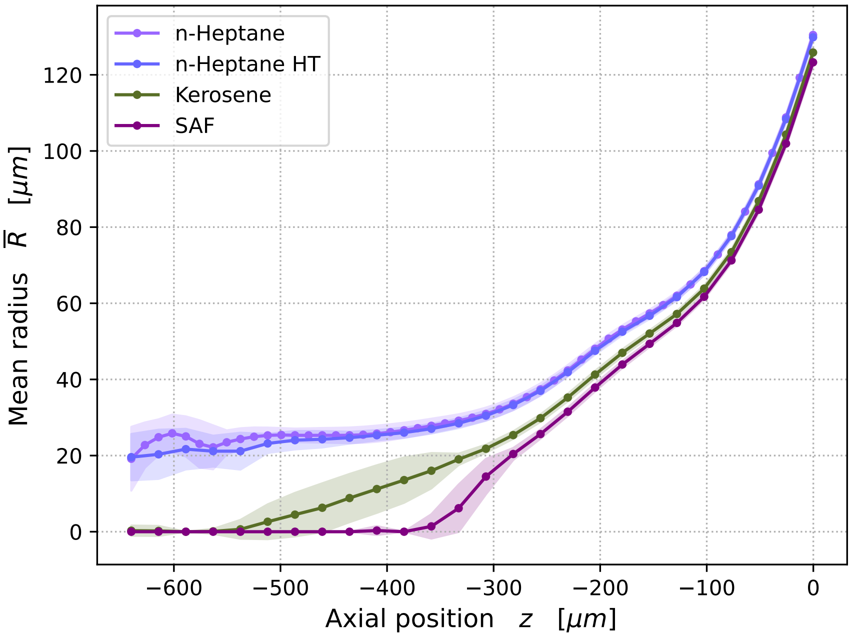

Figure 6.12: Evolution of the temporal average of the aircore radius ($\overline{\overline{R}}^k$ in eq. 4.10) along the z axis. The shaded area above and below each curve represents the standard deviation (σ_R^k in eq. 4.11) of the calculated averages.

En las curvas de la figura 6.12 se puede ver para cada combustible, la evolución del valor promediado temporal y espacialmente del radio del núcleo de aire en la dirección axial. Se puede ver que para todos los combustibles, este valor pormedio del radio es máximo en el orificio de salida ($z = 0$) y que apartir de ese máximo, a medida que se avanza en la dirección negativa axial (hacia adentro del inyector),el valor promedio desciende con muy baja desviación hasta llegar a la zona donde aumenta la desviación (el area sombreada arriba y abajo de la curva) y finalmente llega a un valor mínimo.

In the curves of figure 6.12, one can observe, for each fuel, the temporal and spatially averaged evolution of the air core radius in the axial direction. It is noticeable that for all fuels, this averaged radius value is maximum at the outlet orifice ($z = 0$), and from this maximum, as one progresses in the negative axial direction (inside the injector), the averaged value decreases with very low deviation until reaching the region where the deviation increases (the shaded area above and below the curve), and finally reaches a minimum value.

Instead, in the same figure 6.12, it can be observed that for kerosene and for SAF, deviations from the average values only suddenly appear at a certain axial position and remain approximately within the same range before decreasing when the air core has collapsed and its radius is null. This indicates that the lower part of the air core in these real fuels does not allow such a stable air core to form, probably because they are denser, more viscous, and have a higher surface tension. In these two fuels, the swirl of the flow is lower, which can be seen in the curves of figure 6.8. The depth of air core penetration is closely related to the Reynolds number of the flow at the inlet of the tangential ports. The Re is calculated at the inlet of the tangential ports, and its values can be seen in table 6.3.

	n-Heptane	n-Heptane HT	Kerosene	SAF
Re	2194.78	3644.88	720.29	521.64
u [m/s]	12.16	13.07	10.39	10.93

Table 6.3: Reynolds numbers (Re) and uniform average velocities (u) of the fuels at the tangential ports inlets

Reynolds numbers at the entrance of the tangential ports corresponds to the length of maximum penetration achieved by each fuel. The higher the Reynolds number, the greater the penetration of the air core. It is therefore seen that it is important that the force of the flow be greater than the flow resistance in order to form a flow with sufficient swirl to suck and form a stable air core.

As can be seen in figure 6.11, kerosene is the fuel with the largest differences between the spatial average curves, which indicates that between the different instants of the averaging window, the air core of this fuel was not as stable as expected. Although a part of the air core remains without many variations, it can be seen that from a certain axial position, the average value of the radius begins to have strong deviations and even becomes zero in different axial positions. This shows that the air core in this fuel had an oscillating depth that was captured within the averaging window, which was not something that was expected.

SAF is the fuel with the lowest aircore penetration, and this can be understood due to its combination of properties, it is not the most dense fuel but it is the most viscous of the four and also the one with the highest surface tension force. This is consistent with its low swirl number values in figure 6.8.

6.2.4 Fuel film thickness

In figure 6.13, the evolution of the liquid film thickness constructed from spatial averages $\bar{t}^{p,k}$ for different axial positions can be observed at various instants: $\bar{t}$ vs z. It is noticeable that these plots are vertically divided into two sub-windows to distinguish axial positions corresponding to the internal flow zone ($z < 0$) and axial positions corresponding to the external flow zone ($z > 0$). This figure shows that, similar to the air core, the spatial average curves overlap with each other, and therefore, it is convenient to plot a single curve of temporal averages from the spatial average curves.

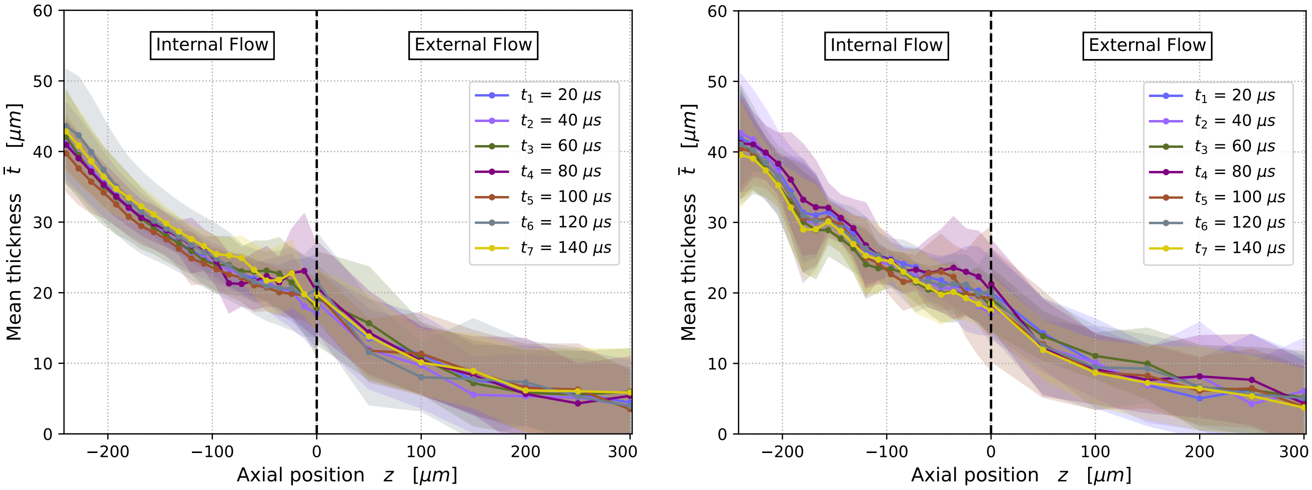

(a) n-Heptane (298 K)

(b) n-Heptane (350 K)

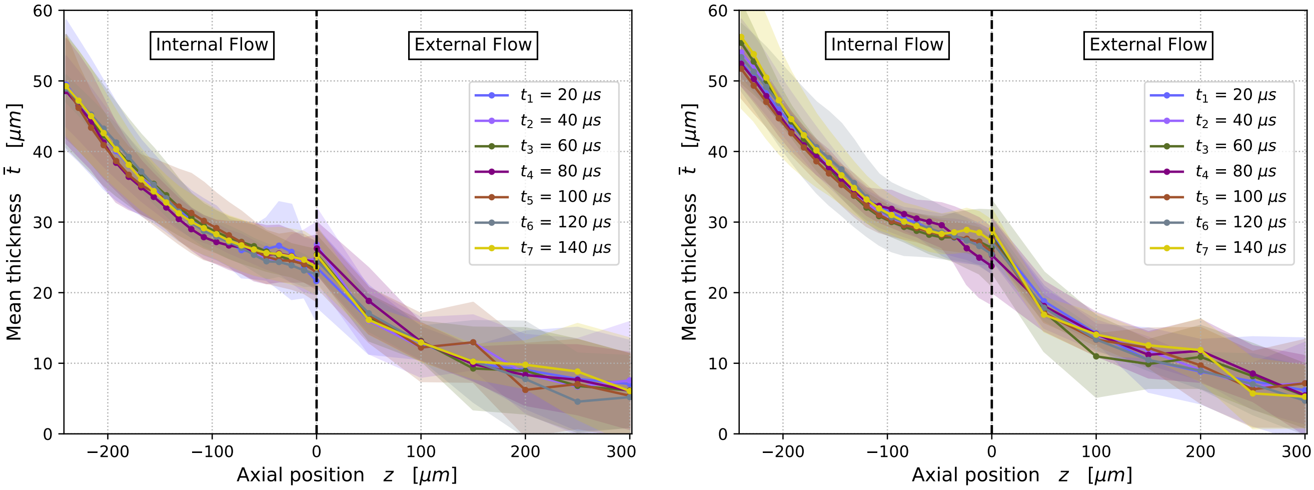

(c) Kerosene

(d) SAF

Figure 6.13: Evolution of the spatial average (over the azimutal coordinate) of the fuel film thickness ($\bar{t}^{p,k}$ in eq. 4.8) along the z axis for different instants. The shaded area above and below each curve represents the standard deviation ($\sigma_t^{p,k}$ in eq. 4.9) of the calculated averages.

On the other hand, in figure 6.14, we can see the time-averaged curves $\bar{\bar{t}}$ versus z, obtained from all the spatial average curves $\bar{t}$ vs z for the 140 instants of the averaging window.

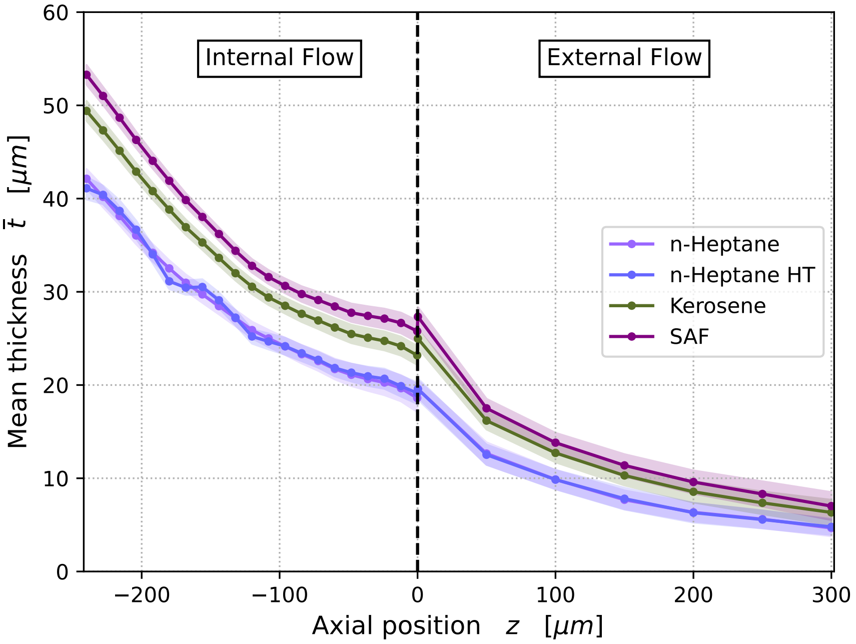

Figure 6.14: Evolution of the temporal average of the fuel film thickness ($\bar{\bar{t}}^k$ in eq. 4.10) along the z axis. The shaded area above and below each curve represents the standard deviation (σ_t^k in eq. 4.11) of the calculated averages.

When comparing the four curves of temporal averages in figure 6.14, at the lowest axial position $z = -240$ μm, it can be observed that for the heptane simulations at both temperatures, similar fuel film thicknesses are obtained, slightly above 40 μm. In contrast, kerosene has a value of 50 μm and SAF a higher value, close to 55 μm. These thickness values correspond to the behavior of the air core described earlier in this section: for the single-component fuel, larger air core radii result in greater fuel film thickness, whereas for kerosene and SAF, narrower air cores are observed, resulting in thicker fuel films. This is due to the lower injection velocities in the kerosene and SAF simulations due to their higher density. By examining the curves of the axial mean velocity component U_{z-mean}, it can be verified that greater magnitudes of this component in the liquid result in smaller fuel film thicknesses $\bar{\bar{t}}$.

In both the spatial average plots $\bar{t}$ vs z (figures 6.13) and the temporal average plots $\bar{\bar{t}}$ vs z (figures 6.14), it can be observed that deviations from the average values are greater in the external flow region. This is because once the fuel film leaves the injector, it becomes much more unstable as it is influenced by aerodynamic oscillations of the air on both sides of its free surface. Additionally, at certain axial positions in the external flow region, there is already sheet cavitation, which causes the average thickness values to be affected by null values that disperse the averaged values $\bar{t}$.

The figures 6.14 once again demonstrate that the fuel film thickness of the single-component fuels at the outlet orifice ($z = 0$) is much lower. The fuel film thicknesses are summarized in table 6.4. These differences in fuel film thickness explain the disparity in ligament sizes observed in the qualitative analysis figures 6.1. In the case of kerosene and SAF, the high thickness of the conical sheet is the cause of the thickness and size of the ligaments detached from the conical sheet, thus affecting the number, size, and velocities of the droplets.

	n-Heptane RT	n-Heptane HT	Kerosene	SAF
$\bar{\bar{t}}^k$ [μm]	19.58	19.13	23.18	25.77
σ_t^k [μm]	0.90	1.19	1.05	1.04

Table 6.4: Temporal average fuel film thickness ($\bar{\bar{t}}^k$ in eq. 4.10) and standard deviation (σ_t^k in eq. 4.11) for the fuels.

As observed in the qualitative analysis, ligaments formed from kerosene or SAF are not only thicker and larger in size but also travel longer distances before breaking up into droplets compared to ligaments formed during heptane atomization. This can be explained by examining the temporal average fuel film profiles of heptane:: 6.13a and 6.13a, which begin to exhibit strong oscillations before reaching the outlet orifice ($z = 0$). In contrast, for kerosene: 6.13c or SAF 6.13d, the fuel film displays fewer oscillations before reaching $z = 0$.

It is easy to observe in the temporal average profiles shown in Fig. 6.14 that all four fuels exhibit a similar descending behavior in their fuel film thickness in the external flow region $0\ \mu\text{m} \leq z \leq 300\ \mu\text{m}$. However, as expected, at the position $z = 300\ \mu$m, simulations of heptane are identified with the thinnest fuel film thickness, while kerosene shows a thicker film and SAF demonstrates an even greater thickness.

6.2.5 Statistical study of the droplet cloud

In this section, the quality of atomization for each fuel is compared more thoroughly based on the droplet cloud produced by primary atomization. To characterize this droplet cloud, probability distribution functions (PDFs) are calculated for various variables describing the behavior of droplets and ligaments in the external flow region, such as sizes, velocities, positions, etc.

A probability density function (PDF) of a variable describing droplet behavior shows how frequently that variable takes a specific value. In other words, a PDF indicates the likelihood of finding a droplet with a particular size, velocity, or any other variable value. This probability value is obtained by averaging all recorded values for all droplets at each recorded time instant (every microsecond) throughout the entire temporal study window (140 microseconds). Therefore, these probability values are bounded by the values obtained during this temporal window for each of the simulations.

Unlike the mesh sensitivity study where a threshold of $\gamma = 0.5$ was used, in the study of this chapter, a cell is considered part of a droplet structure if $\alpha^i_{fuel} \geq \gamma$ with $\gamma = 0.04$. In other words, a cell contributes to an individual structure if its α^i_{fuel} value is equal to or greater than 0.04.

Before analyzing any PDFs, the curve depicting the number of droplets recorded at each simulation time instant for each of the four fuels in this study is described. Figure 6.15 illustrates the evolution of the number of droplets recorded during each microsecond of the averaging window.

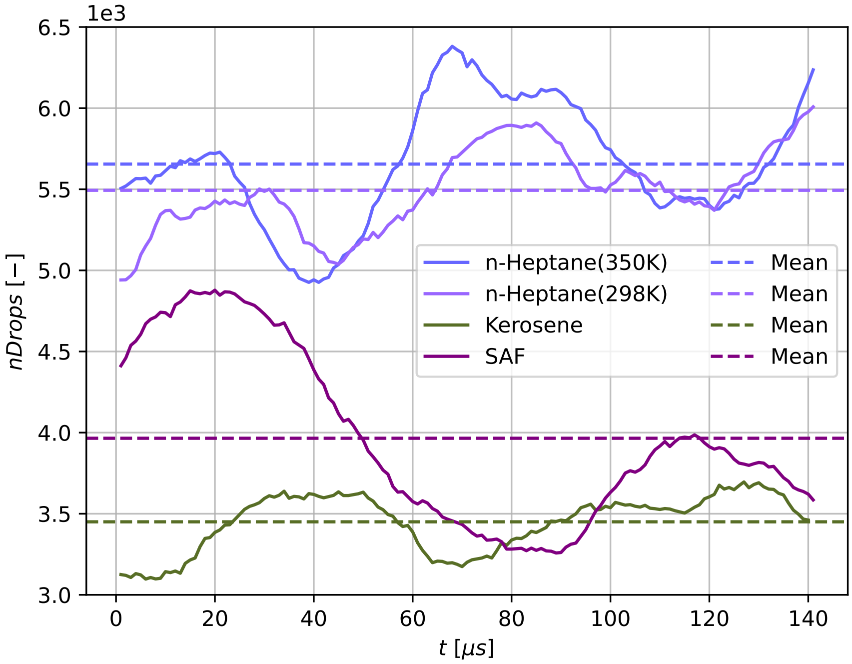

Figure 6.15: Number of registered drops inside the exeternal flow region for each fuel

It can be clearly distinguished that heptane at both temperatures produces a significantly greater number of droplets than SAF fuel or kerosene. It is also notable that the droplet number curve for SAF fuel exhibits a decrease after 50 μs of the averaging window; however, this is attributed to an error in the data collection process of the averaging window.[1]

The average number of droplets recorded for kerosene or SAF fuel is approximately 60% of the average number of droplets recorded in heptane atomization. This is partly due to lower injection velocities in SAF and kerosene. Lower injection velocities result in a thicker fuel film expelled that forms the hollow cone. This causes thicker and longer ligaments to detach, which are more stable and deform less compared to ligaments in heptane atomization. These ligaments travel longer distances within the domain before breaking into droplets, thereby reducing the number of droplets recorded in the simulated domain. Furthermore, for these fuels, lower velocity magnitudes in the external flow region reduce aerodynamic drag effects on the spray interface. As a result, there are fewer oscillations that disturb the ligaments and fuel film surface, decreasing interface deformations that induce the formation of new droplet generations.

---

[1] The simulation of SAF fuel exhibited a different behavior compared to the other simulations. In all simulations, the stabilization of the air core penetration length was taken as the criterion to begin recording data in the temporal study window. However, in the case of SAF fuel, although its air core reached a penetration position and oscillated around it, the large-sized atomization droplets from the initialization stage in first-order schemes (see Section 4.3) had not yet completely exited the domain due to numerical diffusion effects near the exit boundary. These droplets remained stalled near the upper region close to the exit boundary, thereby affecting the data recording within the 140 microsecond temporal study window. Consequently, the recorded number of droplets contained erroneous data from the simulation, despite capturing flow patterns with first-order error schemes. It can be observed how the number of droplets in this fuel decreases over time, indicating that these droplets gradually exited the domain, and proper atomization was only captured with second-order schemes starting from the 100th microsecond of the temporal study window. This behavior of the simulation was detected after data recording had already begun, and restarting data collection and processing was beyond the available time and computational resources for this study.

At high temperatures, heptane registers values of up to nearly 6.5×10^3 generated droplets across the entire external flow region, whereas SAF only reaches values around 4.0×10^3 in total number of droplets recorded at any given instant.

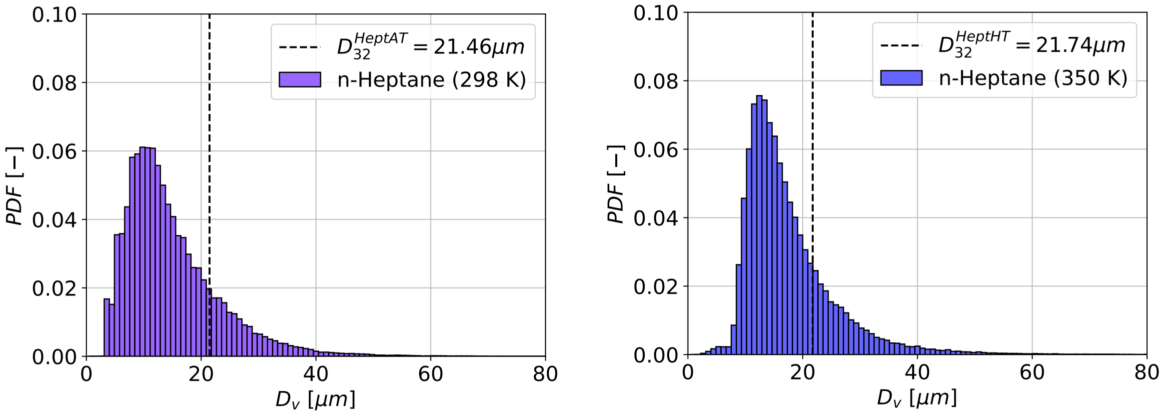

(a) n-Heptane (298 K)

(b) n-Heptane (350 K)

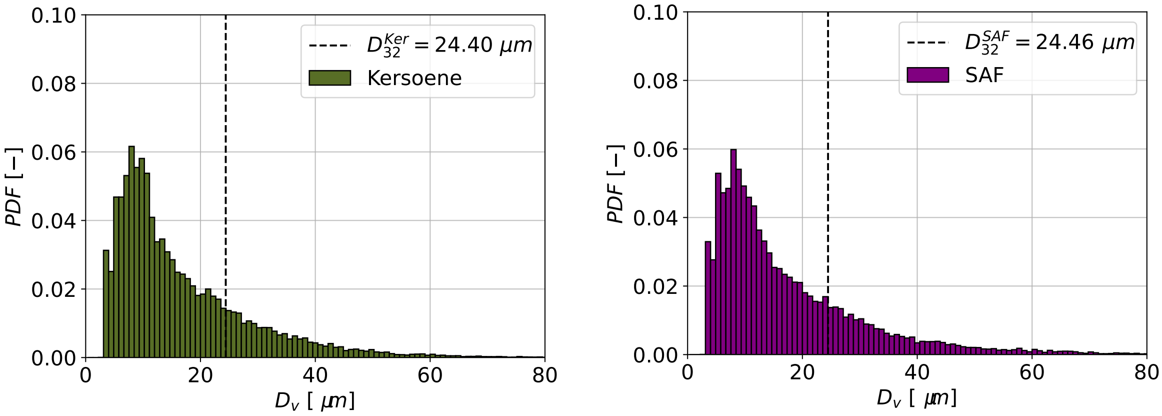

(c) Kerosene

(d) SAF

Figure 6.16: Probability density function of the volumetric diameter of the droptlets and ligaments registerded instantly in the whole computational domain during the temporal study window.

To compare the droplet sizes of each fuel, the probability density function (PDF) is calculated for each, and their graphs can be seen in Figure 6.16. From the graphs in this figure, it is evident that the probability of finding droplets smaller than 20 μm is highest in the high-temperature heptane simulations (Figur 6.16b), followed by room-temperature heptane (Figurea 6.16a), and then by kerosene and SAF (Figures 6.13c and 6.16d respectively).

The probability density functions (PDFs) of kerosene and SAF are lower and broader compared to those of heptane. This indicates that droplet sizes in heptane simulations are concentrated within a narrower range of volumetric diameters: $0\ \mu m \leq D_v \leq 40\ \mu m$. In contrast, simulations of kerosene and SAF exhibit much more varied droplet sizes, with droplets ranging up to 60 μm or 80 μm. Additionally, the bars forming the PDFs of heptane simulations succeed each other in increasing or decreasing order, meaning the probabilities of finding droplets of medium size increase until reaching the most frequent value, and then frequencies decline steadily for larger sizes. This pattern does not occur in SAF or kerosene simulations. In these fuels, the probabilities of finding droplets do not continuously increase to a most common value but are somewhat more random and do not maintain the traditional shape of a log-normal distribution. This suggests that denser fuels generate a less uniform and less consistent droplet pattern over time.

The volumetric mean diameter (SMD) has very similar values for both heptane simulations, approximately **SMD** ≈ 21.4 μm. On the other hand, the denser fuels, kerosene and SAF, have values of **SMD** ≈ 24.4 μm. This again indicates that the average droplet size of kerosene or SAF increases by approximately 15% compared to the droplet size of heptane. SAF exhibits the largest droplet size, although it is very close to kerosene despite the incorrectly recorded droplets.

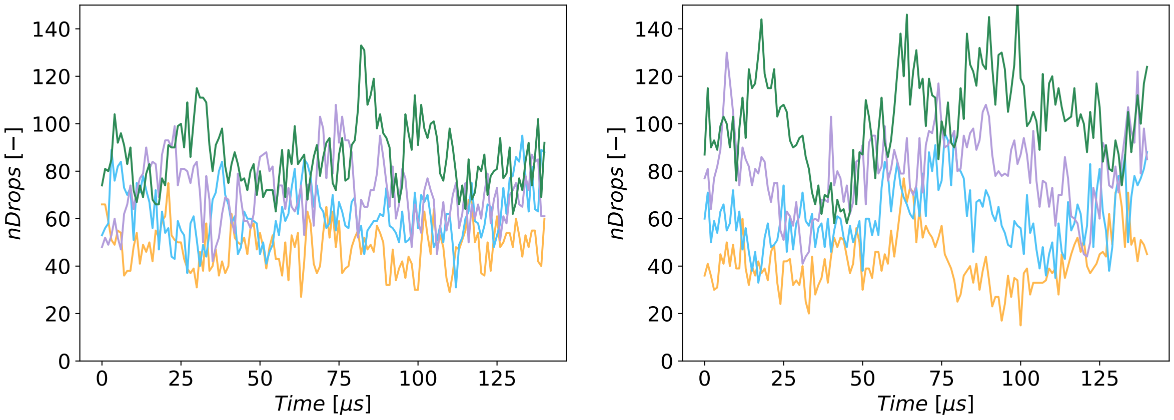

(a) n-Heptane (298 K)

(b) n-Heptane (350 K)

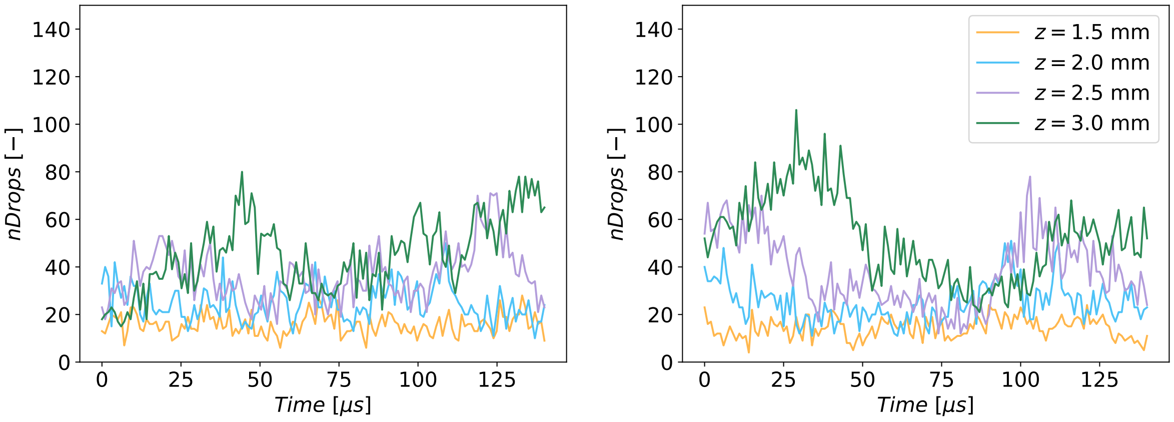

(c) Kerosene

(d) SAF

Figure 6.17: Number of droplets passing through diffrent z planes for each fuel during the temporal study window.

Figure 6.17 shows the curves of the number of drops that instantly cross four axial planes during the entire time interval of the temporal study window. It can be seen how this number of drops is greater for the plane furthest from the exit orifice, the plane $z = 3.0$ mm, followed by the second furthest plane $z = 2.5$ mm, and so on. This indicates that the further away from the exit orifice there are more drops in the simulations, which is due to the fact that the ligaments or drops break into smaller drops, which makes the number of individual structures recorded greater as we move away from the exit orifice.

In figure 6.17, it can also be seen how the atomization of heptane at high temperature exceeds the number of registered drops than the other three fuels. Furthermore, in the graph of this fuel 6.17b, it can be seen that its curves of the number of drops vs time for the different planes are more vertically separated than those of the other fuels. When figures 6.17a and 6.17b are compared, it can be seen that for the plane $z = 1.5$ mm, the two simulations of heptane register very similar numbers of drops. However, for planes further away from the exit orifice, such as $z = 2.5$ mm and $z = 3.0$ mm, heptane at high temperature, although it has similar droplet numbers to heptane, outperforms heptane at room temperature due to greater disaggregation of ligaments and large droplets into smaller droplets.

In the SAF, in figure 6.17d, it can be seen that the number of drops in the plane $z = 3.0$ mm is much higher than in the other planes during the first 50 microseconds of its simulation. These data are erroneous due to an anomalous and unexpected behavior of the simulation of this fuel that was explained in the previous footnote 1. The valid results for this simulation are considered from microsecond 110 of the time study window. From this instant, it can be seen that the SAF records numbers of drops similar to and slightly lower than those of kerosene in the plane $z = 3.0$ mm.

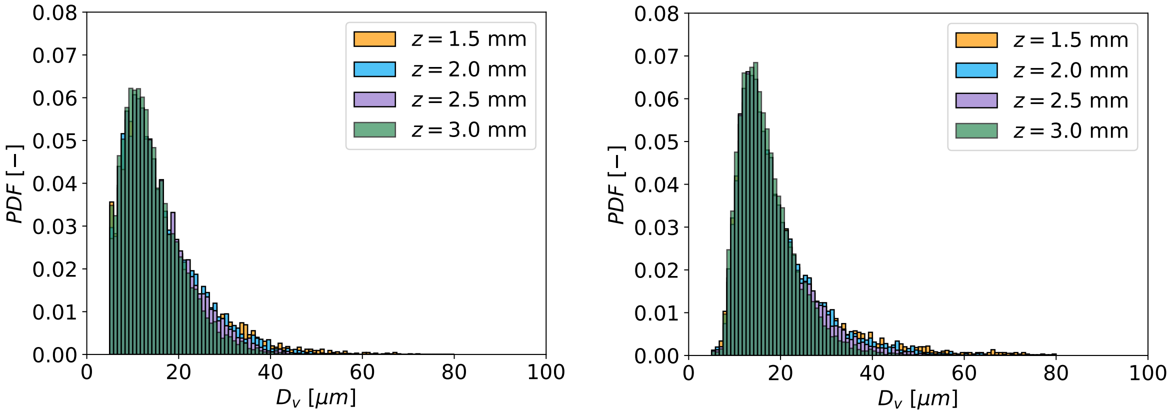

(a) n-Heptane (298 K)

(b) n-Heptane (350 K)

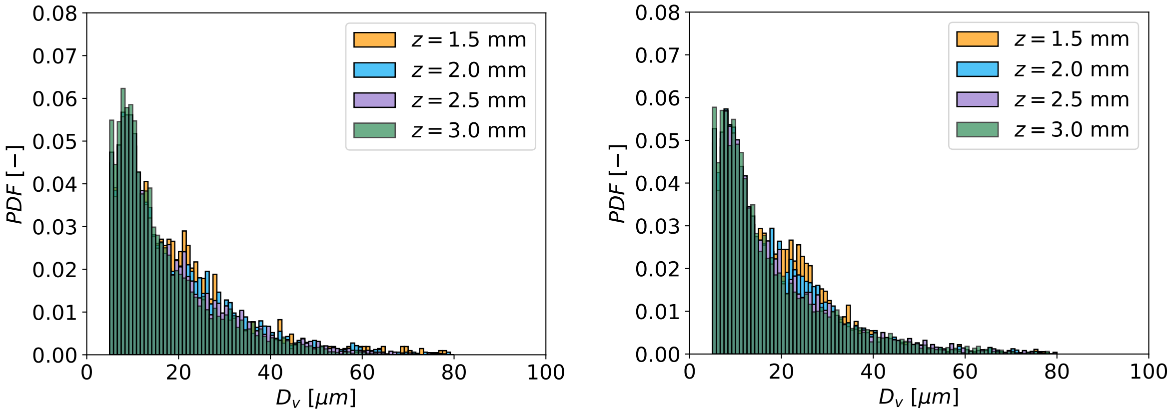

(c) Kerosene

(d) SAF

Figure 6.18: Probability density function of the volumetric diameter of the droplets passing through different z planes for ach fuel during the temporal study window.

In Figure 6.18, the PDFs of droplet sizes recorded at different axial planes are shown. It can be observed that the PDF at the axial plane $z = 3.0$ mm is the narrowest and most slender, indicating that droplet sizes become smaller and more uniform as we move away from the exit orifice. It is notable for both kerosene and SAF that the PDFs at planes closer to the exit orifice, specifically at $z = 0.0$ mm, are much more irregular compared to the plane at $z = 3.0$ mm. This suggests that near the exit orifice, droplet sizes are much more irregular and dispersed compared to regions further away from the exit orifice. This result can be explained by the fact that in these denser fuels, at planes like $z = 1.5$ mm and $z = 2.0$ mm, there are still large ligaments that have not fully broken apart, which are counted as large droplets. Additionally, in these planes, small droplets have detached from these same ligaments or from the intact cone sheet of the air core. This can be observed in Figure 6.1.In contrast, in regions far from the exit orifice, there is a more uniform distribution of predominantly small droplets ($D_v \leq 20$ μm).

For heptane at both temperatures, the PDFs of sizes in different axial planes are very similar because these PDFs converge to the same distribution as we move away from the exit orifice. This convergence occurs because at a certain distance from the exit orifice, the process of ligament breakdown or large droplets breaking into smaller droplets has already completed.

Therefore, in planes further from this position where droplet breakup has ended, the same PDF is observed because the same set of droplets travels in the axial direction. In contrast, for kerosene and SAF, there is significant variation between the PDFs at the selected axial planes. This is because in these fuels, due to properties that hinder atomization, the breakdown and formation of smaller droplets occurs at greater distances from the exit orifice.

Spatial distribution of droplets

In figure 6.19, cross-PDFs are used which show the probability of finding a droplet in both an axial and a radial coordinate simultaneously. Due to the hollow cone angle of the pressure swirl atomizer, ≈ 41°, then all four fuels show that the droplets are distributed in very similar coordinates in both directions, i.e. for the same z position more droplets are found in the same r position. However, as the axial position z increases, then there is a greater dispersion of droplets in the radial direction. This shows that the spray breaks up into droplets mainly in the axial direction, but also in the radial direction. In fact, kerosene and SAF show a greater dispersion of droplets in the radial direction, which is further verified by studying the PDFs of the velocity components.

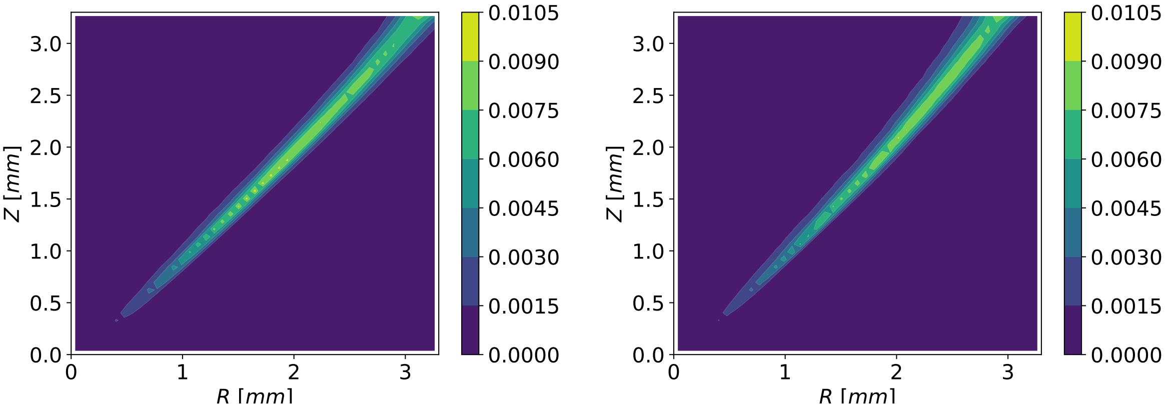

(a) n-Heptane (298 K)

(b) n-Heptane (350 K)

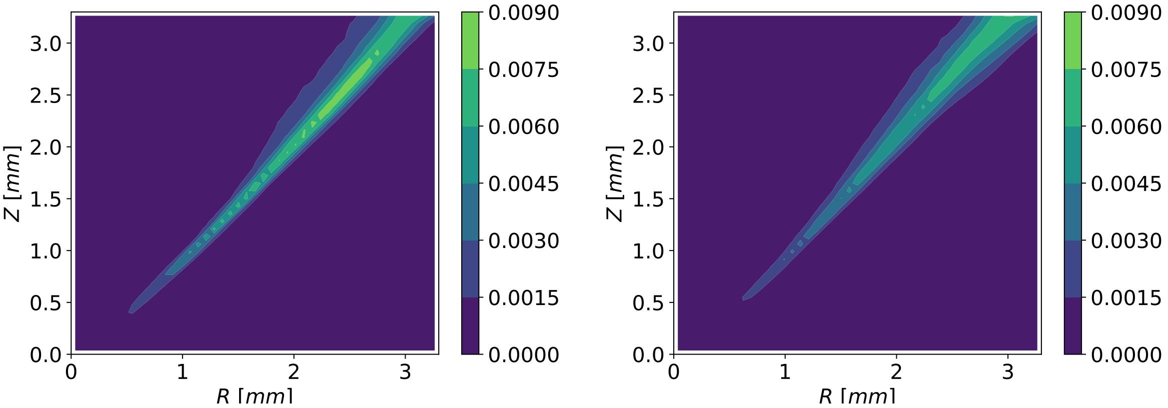

(c) Kerosene

(d) SAF

Figure 6.19: Probability density function of the axial (z) and radial (R) coordinates of the droplets positions

Droplet velocities

The velocity magnitude PDFs for the droplets of each fuel can be seen in Fig 6.20a. The difference in the highest frequencies between the simulations of heptane and the simulations of SAF and kerosene is noticeable. The most frequent velocity magnitudes (peak values of the PDFs) in the heptane droplets at both temperatures are considerably higher than those of the most frequent velocity magnitudes in the SAF or kerosene droplets. This result was expected due to the higher injection velocities and axial component for heptane, as seen in Figs 6.5 and 6.9.

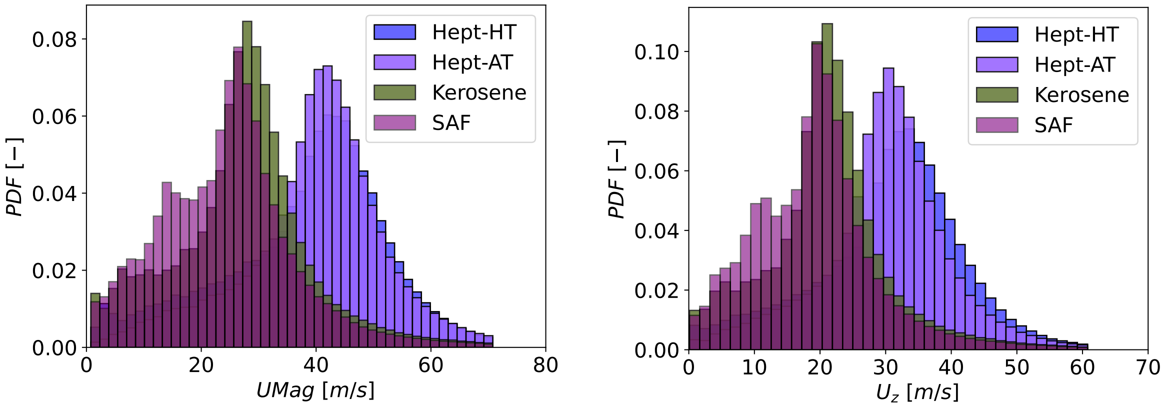

(a) Droplets velocity magnitude

(b) Droplets axial velocity

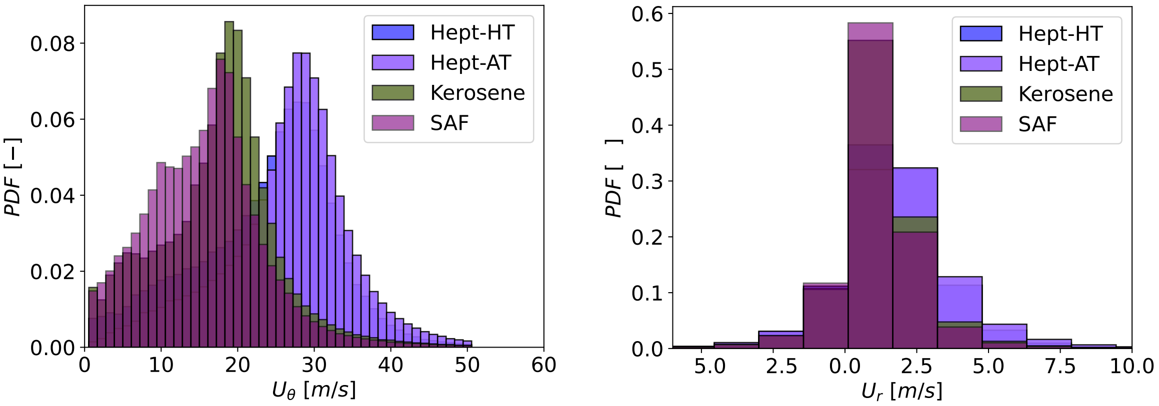

(c) Droplets tangential velocity

(d) Droplets radial velocity

Figure 6.20: Probability density functions of the velocity components of the droplets in all the domain

When comparing the two simulations of heptane, in figures 6.20b and 6.20c, it can be seen that the axial and tangential components of the velocities of the high-temperature heptane droplets have higher frequencies for lower velocities compared to the room-temperature heptane droplets. This is particularly noticeable in the tangential component, indicating that room-temperature heptane is the fuel with droplets having higher tangential velocities, meaning it retains more swirl in the flow of droplets.

When comparing SAF and kerosene, it is evident that droplets with lower velocities are more frequently found in SAF, as indicated by the PDFs of their velocity components concentrating in regions of low speeds. This is primarily due to first-order simulation droplets that halted before fully exiting the domain and were recorded within the temporal study window. This can be observed by examining the PDFs of droplets recorded at various axial planes in Figure 6.21. In this figure, it is apparent that SAF's PDFs display a more normal distribution for most planes, except for the $z = 3.0$ mm plane where first-order simulation droplets were captured. Beyond this, it is noticeable that the peak frequency value of SAF is lower than that of kerosene in both magnitude and all velocity components. This suggests that overall, SAF droplets travel more slowly in all directions compared to kerosene, despite exhibiting similar behaviors in other variables.

Upon observing the PDF in Figure 6.20d, it is noticeable that all fuels produce droplets whose most frequent radial velocity component is near zero. This indicates that the droplets travel at low speeds in this direction. The presence of both positive and negative values in this component suggests that the droplets are moving both towards the center and away from it in a balanced manner, aligned with the preferred direction of the film.

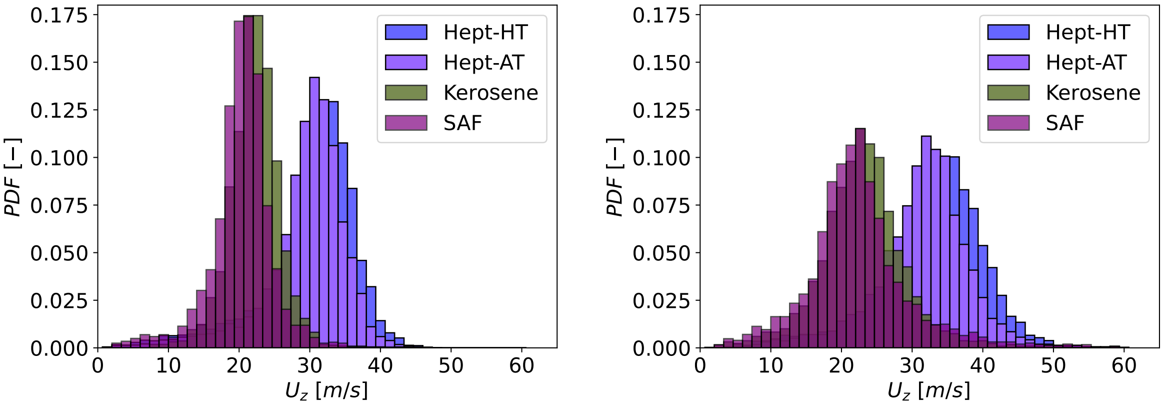

(a) Plane $z = 1.5$ mm

(b) Plane $z = 2.0$ mm

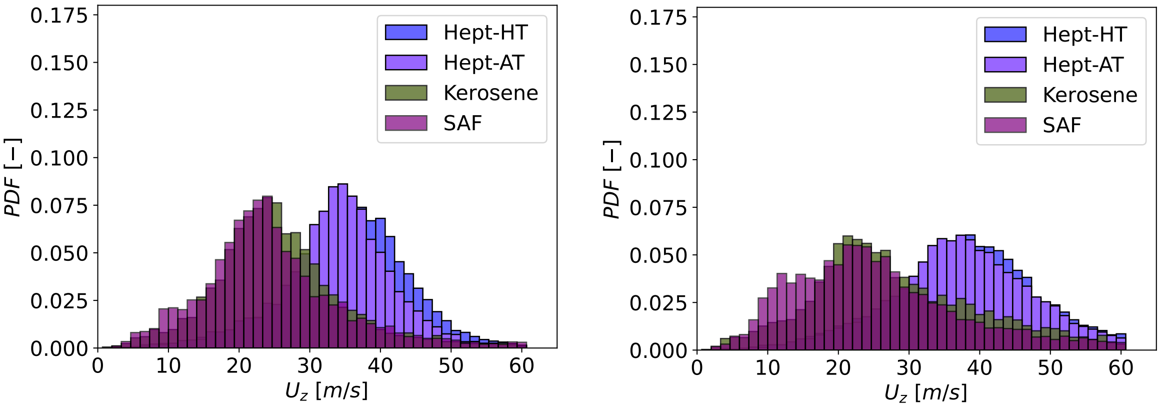

(c) Plane $z = 2.5$ mm

(d) Plane $z = 3.0$ mm

Figure 6.21: Probability density function of the axial (U_z) velocities of the droplets at different axial planes.

In order to make a more detailed analysis of the droplet cloud evolution in the axial direction, the PDFs of the droplets that passed through four axial planes are studied: $z = 1.5$ mm, $z = 2.0$ mm, $z = 2.5$ mm and $z = 3.0$ mm. In figure 6.21, each graph makes a comparison of the axial component of the velocity of the droplets of the four fuels in the same axial plane.

In figure 6.21a, the magnitudes of this velocity component can be seen in the $z = 1.5$ mm plane. Comparing the most frequent velocities of each fuel, it can be observed that, at this axial position, the high-temperature heptane simulation has the highest values among the four fuels, followed very closely by the most frequent velocities of heptane at room temperature and, further apart, the most frequent velocities of SAF and kerosene. Although the axial components of the heptane droplets are higher, at this axial position, the kerosene and SAF droplets have narrower PDFs, indicating that at this axial position, kerosene and SAF have droplets with more uniform velocities than the heptane droplets.

However, as we move further along the axial position away from the exit orifice, it is observed that the axial velocities of kerosene and SAF droplets become increasingly less uniform. Consequently, their PDFs become wider and flatter. The same trend is observed with heptane droplets, but they consistently maintain higher axial components compared to SAF or kerosene.

6.3 Computational cost

This parametric study was made possible by the cluster available at the CMT Institute, known as the CMT cluster. This cluster operates as a High Performance Computing (HPC) environment, using the Message Passing Interface (MPI) to enable parallel computing. The simulations of this parametric study were run in parallel, subdividing the computational domain into multiple processes.

In the simulations of heptane, different numbers of parallel processes were used at different stages (see section 4.3). In contrast, a total of 120 processes were always used in the simulations of kerosene and SAF. The computational costs of each simulation stage for each fuel are shown in tables 6.5 to 6.8.

Stage	Cores	CPUh	Computational time [days]
Initialization 1^{st} order	216	57.9e3	11.17
Initialization 2^{nd} order	216	133.1e3	28.17
Stable sim	432	113.1e3	10.91

Table 6.5: n-Heptane at ambient temperature (298 K) computational cost

Stage	Cores	CPUh	Computational time [days]
Initialization 1^{st} order	96	48.4e3	21
Initialization 2^{nd} order	216	624.7e3	12
Stabilized	120	74.3e3	25.8

Table 6.6: n-Heptane at high temperature (350 K) computational cost

Stage	Cores	Cost [CPUh/ms]	CPUh	Computational time [days]
No AMR	120	8.6e3	26.4e3	3.88
AMR 1^{st} order	120	99.2e3	34.8e3	11.88
AMR 2^{nd} order	120	300.3e3	80.6e3	28
Stabilized	120	377.0e3	53.9e3	18.7

Table 6.7: Kerosene computational cost

Stage	Cores	Cost [CPUh/ms]	CPUh	Computational time [days]
No AMR	120	8.3e3	36.5e3	12.7
AMR 1^{st} order	120	141.4e3	33.1e3	11.45
AMR 2^{nd} order	120	397.8e3	80.5e3	28
Stabilized	120	413.4e3	56.8e3	19.7

Table 6.8: SAF computational cost

When comparing the number of calculation hours required in the stabilized stage of the simulations of the four fuels, it can be seen how the computational cost of the simulations in the less dense fuels and therefore with the highest injection speeds increases. This is because, in order to maintain the stability condition of the simulations given by the Courant number, having higher speeds, the time step of the same must be reduced.

In tables 6.8 and 6.7, you can see an additional column: ‘Cost [CPUh/ms]’, which contains the costs in terms of computing hours required for the simulation to advance one millisecond of simulated time. For each of the simulation stages, you can see how as the error order of the schemes increases and the AMR meshing is included, then there is increasingly more computational cost. This shows how computational resources can be saved by simulating the initialization stages with less expensive schemes.

Chapter 7

Conclusions and future work

The simulations and post-processing carried out in this work allowed the successful completion of the comparative study of four different fuels, including the SAF fuel of the HEFA SPK family.

The computational model used in this study is sensitive to changes in the physical properties of the liquid phase used and therefore allowed the simulation and comparison of the two fuels of interest in this study: conventional kerosene versus SAF.

The simulations were maintained in a stable state using the selected second-order numerical schemes. These schemes captured the atomization of the four fuels in the parametric study in the mesh used. The stability of the simulations was maintained using the Courant number by adapting the time step size of the solution.

The strategy of using first-order spatial discretization schemes together with the URANS approach to model turbulence in the initialization phase of the simulations allowed to save significant computational costs before moving to second-order schemes and implementing the LES approach. This latter approach allowed to capture turbulent fluctuations of the two-phase flow at their largest scales, determined by the mesh size.

The IsoAdvector interface reconstruction scheme, together with Adaptive Mesh Refinement (AMR), allowed capturing a sharp interface in the two-phase flow of immiscible phases. This methodology for capturing and defining the interface allowed comparing the formation of the air core, the formation of the conical sheet, and the disintegration of the same into ligaments and droplets in the four fuels.

The SAF simulation showed a different behaviour from the simulations of the other three fuels from a numerical point of view. Although the same computational time was kept running as the other simulations, within this time the air core stabilized much faster, but its droplets captured with first-order schemes slowed down and took much longer to leave the domain. This affected the measured results for the droplet cloud, but fortunately, it was possible to distinguish that only the region closest to the exit boundary was the part of the simulation that was affected by these erroneous data. Thus, the validity of these data could be identified and excluded in the analyses performed.

Regarding the parametric study, it can be concluded that:

- The air core in both high-temperature and room-temperature heptane formed in such a way that it extended to the lowest part of the atomizer, although it was more stable in high-temperature heptane. This is because these fuels have high injection velocities, resulting in high Reynolds numbers and high swirl numbers, which increase the centrifugal inertia that separates the liquid at the center of the atomizer and forms the air core.
- Both kerosene and SAF, being denser fuels with higher viscosity and surface tension, were unable to form an air core as deep as that of heptane. However, despite SAF being less dense than kerosene and having higher axial velocities, it formed a much shallower air core than kerosene. This is because SAF is the most viscous fuel among the four, which significantly reduces the Reynolds number of the flow and decreases the tangential momentum flow in the internal flow of the atomizer, as indicated by the swirl number.
- The reduced size of the air core in the SAF is reflected in its greater fuel film thickness. This fuel, of the four, has the greatest film thickness at the exit orifice. This causes its ligaments that detach from the conical sheet to also be large, and this in turn was reflected in the PDFs of the sizes in the axial planes. It was observed that in the plane $z = 1.5$ mm the ligaments increased the frequencies of the large sizes, while in planes further from the exit orifice, these sizes were less frequent.
- SAF exhibits a droplet cloud very similar to that of kerosene, but both in the PDFs of the entire domain and in those of the axial planes, it can be observed that SAF forms larger droplets, which is not beneficial for combustion. For both fuels, their droplet cloud stabilizes at distances further from the exit orifice than the single-component fuels. In all four fuels, it was found that the droplet cloud loses uniformity in the individual velocities of the droplets as it moves away from the exit orifice. Despite these differences from heptane, it has been demonstrated that 100% SAF injection behaves very similarly to kerosene, showing that its use in aviation engines is feasible in this regard.

7.1 Future work

To further this study and obtain additional results that complement the analysis of this master's thesis, it could be beneficial, on one hand, to enhance the precision and accuracy of the numerical configuration used in this study, and on the other hand, to incorporate post-processing tasks that assist in better describing the atomization behavior.

- As a first suggestion to improve the numerical configuration of the computational model, if sufficient computational resources are available, simulations could be conducted with a larger domain in the axial direction. In other words, increasing the size of the external flow region in the axial direction of the injection, to capture how atomization occurs at a greater distance from the outlet orifice. This would enable the capture of the breakup into smaller droplets of fuels denser than heptane, such as kerosene or SAF, which form ligaments that travel greater axial distances before breaking apart.
- Another approach could involve conducting a parametric study comparing fuel injections with equal velocities at the inlet of the tangential ports. In this case, instead of imposing a maximum mass flow rate boundary condition for all fuels, a velocity boundary condition should be applied. This would allow for a comparison of atomization quality among fuels with the same injection velocity.

- To capture the interface and breakup in greater detail, as well as the advective transport of the interface, adding a level of refinement in adaptive meshing (AMR) could be considered. This entails increased computational cost and longer simulation times due to the higher Courant number, but it is justified as long as there is an increase in computational capability.

- To enhance the quality of measurements of the fuel film thickness in the external flow region, a post-processing tool could be implemented to calculate the thickness perpendicular to the cone angle formed during injection. This approach would provide a more realistic measurement by considering the direction in which the fuel film is injected.

- To describe the droplet cloud with higher quality and rigor, one could include within the droplet detection algorithm a subprocess that calculates the sphericity of each detected structure. This approach would enable classification between droplets and unbroken ligaments. Consequently, it would allow for distinguishing the axial positions where droplets of each size form and precisely where ligaments of each fuel break along the axial position.

Bibliography

[1] Eurostat. *Renewable energy statistics.* 2023. URL: `https://ec.europa.eu/eurostat/statistics-explained/index.php?title=Renewable_energy_statistics#Share_of_renewable_energy_more_than_doubled_between_2004_and_2022`.

[2] Ministerio para la Transición Ecológica y el Reto Demográfico (MITECO). *Emisiones de gases de efecto invernadero.* Inventario Nacional de Emisiones a la Atmósfera Serie 1990-2021. 2023.

[3] Ministerio para la Transición Ecológica y el Reto Demográfico (MITECO). *Marco Estratégico de Energía y Clima: una oportunidad para la modernización de la economía española y la creación de empleo.* 2020. URL: `https://www.miteco.gob.es/es/cambio-climatico/participacion-publica/marco-estrategico-energia-y-clima.html`.

[4] International Air Transport Association. IATA. *Net zero 2050: Sustainable Aviation Fuels.* 2023. URL: `https://www.iata.org/en/iata-repository/pressroom/fact-sheets/fact-sheet---alternative-fuels/`.

[5] Amer Eid Salem Eid Thafnan Alajmi et al. "Fuel atomization in gas turbines: A review of novel technology". In: *International Journal of Energy Research* 43.8 (2019), pp. 3166–3181. DOI: `https://doi.org/10.1002/er.4415`.

[6] Jie Yang et al. "An overview on performance characteristics of bio-jet fuels". In: *Fuel* 237 (Feb. 2019), pp. 916–936. ISSN: 0016-2361. DOI: `10.1016/j.fuel.2018.10.079`. URL: `https://www.sciencedirect.com/science/article/pii/S0016236118317927`.

[7] CMT. Clean Mobility and Thermofluids. *Injection Test Rigs.* 2020. URL: `https://www.cmt.upv.es/#/injectiontestrigs`.

[8] Alicia Muñoz Agulló. *Modelado CFD del Flujo Interno y la atomización de un inyector pressure-swirl de Uso Aeronáutico Mediante distintos Esquemas de Reconstrucción de interfase.* 2022. URL: `https://riunet.upv.es/handle/10251/187729`.

[9] Arthur H Lefebvre and Vincent G McDonell. *Atomization and Sprays.* CRC Press, 2017. DOI: `10.1201/9781315120911`. URL: `https://www.taylorfrancis.com/books/mono/10.1201/9781315120911/atomization-sprays-arthur-lefebvre-vincent-mcdonell`.

[10] L. P. Bayvel. *Liquid Atomization.* CRC Press, Aug. 1993. ISBN: 978-0-89116-959-8.

[11] *Pneumatic Air Atomizing Nozzles For Disinfection and Sterilization.* URL: `https://www.disinfectionnozzle.com` (visited on 02/12/2024).

[12] Reza Alidoost Dafsari et al. "Viscosity effect on the pressure swirl atomization of an alternative aviation fuel". In: *Fuel* 240 (2019), pp. 179–191. ISSN: 0016-2361. DOI: `https://doi.org/10.1016/j.fuel.2018.11.132`.

[13] Zhongtao Kang et al. "Review on pressure swirl injector in liquid rocket engine". In: *Acta Astronautica* 145 (2018), pp. 174–198. ISSN: 0094-5765. DOI: `https://doi.org/10.1016/j.actaastro.2017.12.038`.

[14] Suresh Menon and Reetesh Ranjan. "Spray Combustion in Swirling Flow". In: *Coarse Grained Simulation and Turbulent Mixing.* Ed. by Fernando F. Grinstein. Cambridge: Cambridge University Press, 2016, pp. 351–392. ISBN: 9781316575048. DOI: `10.1017/CBO9781316480243.014`. URL: `https://www.cambridge.org/core/books/coarse-grained-simulation-and-turbulent-mixing/spray-combustion-in-swirling-flow/EB5399A2E5F056509B988D9996E2284A` (visited on 04/15/2024).

[15] N.K. Rizk and A.H. Lefebvre. "Prediction of Velocity Coefficient and Spray Cone Angle for Simplex Swirl Atomizers". In: *International Journal of Turbo and Jet Engines* 4.1-2 (1987), pp. 65–74. DOI: `doi:10.1515/TJJ.1987.4.1-2.65`. URL: `https://doi.org/10.1515/TJJ.1987.4.1-2.65`.

[16] Bruce R. Munson, Alric P. Rothmayer, and Theodore H. Okiishi. *Fundamentals of Fluid Mechanics, 7th Edition.* Google-Books-ID: GQMcAAAAQBAJ. Wiley, 2012. ISBN: 978-1-118-21459-6.

[17] Joel H. Ferziger and Milovan Perić. "Finite Volume Methods". In: *Computational Methods for Fluid Dynamics.* Berlin, Heidelberg: Springer Berlin Heidelberg, 2002, pp. 71–89. ISBN: 978-3-642-56026-2. DOI: `10.1007/978-3-642-56026-2_4`. URL: `https://doi.org/10.1007/978-3-642-56026-2_4`.

[18] Stephen B. Pope. *Turbulent Flows.* Cambridge University Press, 2000.

[19] Chris Greenshields and Henry Weller. *Notes on computational fluid dynamics: General principles.* Jan. 2023. URL: `https://doc.cfd.direct/notes/cfd-general-principles/introduction-to-turbulence`.

[20] Steven L. Brunton. *Turbulence Closure Models: Reynolds Averaged Navier Stokes (RANS) & Large Eddy Simulations (LES).* Video. Apr. 23, 2021. DOI: `10.52843/cassyni.cjkr7f`. URL: `https://doi.org/10.52843/cassyni.cjkr7f` (visited on 04/02/2024).

[21] D. Kuzmin, O. Mierka, and S. Turek. *On the implementation of the $k-\varepsilon$ turbulence model in incompressible flow solvers based on a finite element discretisation.* Jan. 2008. URL: `https://www.inderscience.com/offers.php?id=16531`.

[22] David Barre. *Numerical simulation of ignition in Aeronautical Combustion Chambers.* 2014. URL: `https://theses.fr/2014INPT0004`.

[23] Stephen B Pope. "Ten questions concerning the large-eddy simulation of turbulent flows". In: *https://iopscience.iop.org/* (2003). URL: `https://iopscience.iop.org/article/10.1088/1367-2630/6/1/035`.

[24] I. B. Celik, Z. N. Cehreli, and I. Yavuz. "Index of Resolution Quality for Large Eddy Simulations". In: *Journal of Fluids Engineering* 127.5 (Sept. 2005), pp. 949–958. ISSN: 0098-2202. DOI: `10.1115/1.1990201`. URL: `https://doi.org/10.1115/1.1990201`.

[25] David S-K. Ting. *Basics of Engineering Turbulence.* 2016. URL: `https://www.sciencedirect.com/book/9780128039700/basics-of-engineering-turbulence`.

[26] Yunus Çengel and John Cimbala. *Fluid Mechanics: Fundamentals and Applications.* 3rd. McGraw-Hill Education, 2014.

[27] Guan Heng Yeoh and Jiyuan Tu. "Chapter 6 - Free Surface Flows". In: *Computational Techniques for Multiphase Flows (Second Edition).* Ed. by Guan Heng Yeoh and Jiyuan Tu. Second Edition. Butterworth-Heinemann, 2019, pp. 415–462. ISBN: 978-0-08-102453-9. DOI: `https://doi.org/10.1016/B978-0-08-102453-9.00006-4`. URL: `https://www.sciencedirect.com/science/article/pii/B9780081024539000064`.

[28] Johan Roenby, Henrik Bredmose, and Hrvoje Jasak. “A computational method for sharp interface advection”. In: *R. Soc. Open Sci.* 3.160405 (2016), p. 160405. DOI: `10.1098/rsos.160405`. URL: `http://doi.org/10.1098/rsos.160405`.

[29] URL: `https://www.openfoam.com/`.

[30] Benoit Fiorina and Constantin Nguyen Van. *Joined Comparative Study of the CORIA Rouen Spray Burner Simulation Instructions.* Safran Tech, 78772 Magny-les-Hameaux, France. 7th Workshop on Measurement and Computation of Turbulent Spray Combustion (TCS7). CORIA, CNRS, 76801 Saint-Etienne-du-Rouvray, France and Laboratoire EM2C, CNRS, CentraleSupélec, 91192 Gif-sur-Yvette, France, Apr. 2019.

[31] Christopher J. Greenshields. *OpenFOAM V11 user guide.* July 2023. URL: `https://doc.cfd.direct/openfoam/user-guide-v11/index`.

[32] © Intertek Group plc. *Análisis de Combustible.* URL: `https://www.intertek.es/combustibles-liquidos/analisis/` (visited on 05/20/2024).

Part II

Specification document

Chapter 1

Purpose of the specification document

The present specification document is a contractual document, meaning it defines the contract between both parties: the workers and the employers. This document establishes the obligations, rights, and conditions that must be respected and followed in the development of this master's thesis. In this case, the involved workers are primarily the student author of this master's thesis and then the supervising tutor. The employers are the Polytechnic University of Valencia and the CMT Institute, which provides facilities, bibliographic material, and computer equipment to carry out this study.

This master's thesis aims to computationally model the simplex atomization of various fuels, including a sustainable aviation fuel (SAF), using computational fluid dynamics. Through this computational model, the characteristics and quality of atomization are compared among different fuels. Therefore, this specification document consists of three parts: Firstly, the set of rights and obligations related to the job position that must be fulfilled by the involved workers. Secondly, the job conditions required by Spanish legislation that must be guaranteed to the involved workers. And thirdly, the specific technical conditions necessary to conduct the numerical research of this master's thesis.

Chapter 2

Obligations and rights of workers

2.1 Workers' obligations

The present master's thesis is carried out within a framework of obligations that the involved workers must fulfill to ensure that their effort is dedicated responsibly and efficiently, thereby achieving the objectives of this study. The obligations aimed at ensuring this compliance are compiled in the Workers' Statute Law of Spanish legislation, approved by Royal Legislative Decree 2/2015 of October 23, and published in the Official State Gazette (reference: BOE−A−2015−11430). The workers have the following basic duties:

1. Fulfill specific job obligations in accordance with the principles of good faith and diligence.
2. Observe the occupational risk prevention measures adopted.
3. Follow the orders and instructions of the employer in the regular exercise of their managerial powers.
4. Not engage in activities that compete with the company, as stipulated by this law.
5. Contribute to improving productivity.
6. Any obligations arising from their respective employment contracts.

To cooperate in the prevention of professional risks within the Company and maintain the highest hygiene standards therein (reference BOE−A−1971−380), workers are also obliged to:

1. Receive training on Safety and Hygiene, as well as on rescue and first aid, in the workplaces provided by the Company or in National Plan Institutions.
2. Properly use personal protective equipment and ensure its perfect condition and maintenance.
3. Immediately report to their superiors any breakdowns and deficiencies that may cause hazards in any workplace or position.
4. Maintain personal hygiene to prevent contagious diseases or inconvenience to their coworkers.
5. Undergo compulsory medical check-ups and vaccinations or immunizations ordered by the competent Health Authorities or by the Company's Medical Service.

6. Not bring unauthorized beverages or substances into the workplaces, nor present themselves or remain in them under the influence of alcohol or any other kind of intoxication.
7. Cooperate in extinguishing disasters and rescuing victims of workplace accidents under the conditions that are reasonably required in each case.

As regards the rights of workers that must be guaranteed by the respective employers in this master's thesis, both basic rights and rights related to the employment relationship are included here. Both types of rights are also included in the Official State Gazette (reference BOE−A−2015−11430).

2.2 Basic Rights

1. Work and free choice of profession or trade.
2. Freedom of association.
3. Collective bargaining.
4. Adoption of collective conflict measures.
5. Strike.
6. Assembly.
7. Information, consultation, and participation in the company.

2.3 Rights in the Employment Relationship

1. The right to effective occupation.
2. The right to promotion and professional training in the workplace, including training aimed at adapting to changes in the job, as well as the development of training plans and actions aimed at promoting greater employability.
3. The right not to be discriminated against directly or indirectly in employment or, once employed, on grounds of marital status, age within the limits set by this law, racial or ethnic origin, social status, religion or beliefs, political opinions, sexual orientation, sexual identity, gender expression, sexual characteristics, membership or non-membership in a trade union, on grounds of language within the Spanish State, disability, as well as on grounds of sex, including unfavorable treatment of women or men for exercising rights related to the reconciliation or shared responsibility of family and work life.
4. The right to physical integrity and to an adequate policy of occupational risk prevention.
5. The right to respect for their privacy and due consideration for their dignity, including protection against harassment on grounds of racial or ethnic origin, religion or beliefs, disability, age, or sexual orientation, and against sexual harassment and harassment on grounds of sex.
6. The right to timely payment of the agreed or legally established remuneration.
7. The right to individually exercise the actions derived from their employment contract.
8. Any other rights specifically derived from the employment contract.

Chapter 3

Workplace Conditions

The regulations that a workplace must comply with are compiled and detailed in the General Ordinance of Safety and Hygiene at Work, published in the Official State Gazette (reference BOE−A−1971−380). Additionally, due to the computational nature of the research and documentation in the present master's thesis, it is necessary to consider and ensure the requirements that the workplace of the involved workers must meet. These requirements are compiled and published in the Official State Gazette BOE−A−1997−8671, which determine the minimum dignified and acceptable conditions for work involving data display screens.

3.1 Workstation Ergonomics

BOE−A−1997−8671 in its ANNEX describes in detail the minimum provisions that both the chair, the work table, and the screen assigned to workers must comply with, and which the employer must ensure:

3.1.1 Work Table

The work table or surface should be non-reflective and of sufficient dimensions, allowing flexible placement of the screen, keyboard, documents, and accessories. The document holder should be stable and adjustable, placed to minimize uncomfortable movements of the head and eyes. Additionally, the space should be adequate to allow workers to maintain a comfortable position during work.

3.1.2 Work Chair

The work chair should be stable, providing the user with freedom of movement and ensuring a comfortable posture. The chair height should be adjustable to suit the individual needs of each user. The backrest should be reclining and its height adjustable, providing adequate support for the back. Additionally, a footrest should be provided for those who wish to use it, offering additional support for an optimal ergonomic posture.

3.1.3 Keyboard

The keyboard should be tiltable and separate from the screen, allowing the worker to adopt a comfortable posture that prevents fatigue in the arms and hands. There should be enough space in front of the keyboard for the user to rest their arms and hands, contributing to an adequate ergonomic posture. The keyboard surface should be matte to avoid reflections that could cause visual discomfort. Additionally, the layout of the keyboard and the characteristics of the keys should facilitate their use, ensuring that symbols on the keys stand out sufficiently and are legible from the normal working position.

3.1.4 Screen

The terminal screen must be stable, without flickering, flashes, or other forms of instability, to ensure a comfortable and safe visual experience. Additionally, the user should be able to easily adjust the brightness and contrast between characters and the background, adapting them to the environmental conditions to prevent visual fatigue. It is essential that the screen be adjustable in orientation and tilt, allowing the user to adjust it according to their ergonomic needs. For greater flexibility, an independent pedestal or adjustable table that supports the screen can be used. Furthermore, it is crucial that the screen does not have reflections or glare that could disturb the user, ensuring an optimal work environment free from visual distractions.

3.2 Workplace Environment Provisions

Regarding the environment and atmosphere of the workplace, certain aspects must be ensured:

3.2.1 Space

The workstation should have sufficient dimensions and be arranged in such a way that there is enough space to allow for changes in posture and work movements.

3.2.2 Lighting

General and task-specific lighting, such as task lamps, should ensure adequate lighting levels and appropriate luminance relationships between the screen and its surroundings, considering the type of work, the user's visual needs, and the type of screen used. The layout of the workplace and workstation, along with the technical characteristics of artificial light sources, should be coordinated to prevent glare and annoying reflections on the screen or other parts of the equipment.

3.2.3 Glare and Reflections

Workstations should be arranged so that light sources such as windows, transparent or translucent partitions, and light-colored equipment or partitions do not cause direct glare or generate annoying reflections on the screen. Windows should have suitable and adjustable covering devices to control the amount of natural light reaching the workstation, ensuring comfortable visual conditions for the users.

3.2.4 Noise

The noise generated by equipment installed in the workstation should be considered when designing it, especially to avoid disturbing concentration or speech.

3.2.5 Heat

Equipment installed in the workstation should not produce additional heat that could cause discomfort to the workers.

3.2.6 Emissions

Any radiation, except for the visible part of the electromagnetic spectrum, should be reduced to insignificant levels from the perspective of protecting the safety and health of workers.

3.2.7 Humidity

An acceptable level of humidity should be created and maintained in the workplace.

Chapter 4

Conditions in Technical Specifications

For the possible completion of this master's thesis, a set of academic resources and engineering research tools were required to conduct the computational numerical study that models the simplex atomization of various fuels. Since these are computational numerical simulations, initially, different computers with appropriate hardware and software specifications were necessary for the numerical simulation. Secondly, other academic resources and services such as a stable internet connection, acquired prior knowledge, and supervision from the thesis advisor were required.

All these required specifications were primarily provided by the university and the CMT research center, and are detailed below.

4.1 Computers

To utilize the specific software used for configuring and executing the preprocessing, calculation, and postprocessing of numerical simulations, three different types of computers with their respective hardware and software were required.

4.1.1 Hardware

1. Cluster. It is a supercomputer that allows subdividing the general problem and parallelizing the calculations performed. It consists of a rack-like structure composed of multiple nodes (computational unit consisting of two multi-core processors, high-capacity memory, and a storage disk or unit) interconnected through a network infrastructure and managed and controlled by a main node known as the front end, which has an interface for user management.

2. Workstation. This is a high-capacity desktop computer tower with input and output hardware (screen, mouse, and keyboard) designed for processing massive data and documentation.

3. Personal laptop. A personal portable computer for managing other computers and documenting the work performed.

4.1.2 Software

1. Operating Systems. All computers used for this study required an operating system capable of installing and managing the necessary software for performing tasks related to this master's thesis. Both the workstation and the cluster's front end utilized the Linux operating system. The personal laptop used the Windows operating system.

2. Modeling and Numerical Calculation Software. The cluster is equipped with OpenFOAM®, an open-source computational simulation tool with no license costs. The cluster's architecture allows distributing simulation tasks among nodes, leveraging parallel processing to accelerate computation time.

3. Post-processing Software. For analysis and visualization of results, ParaView 5.9® is installed on the workstation along with Python™ for more detailed data analysis.

4. Documentation Software. For the development and documentation of the master's thesis, a personal laptop equipped with Microsoft Office and LaTeX was used. Excel was used for data analysis and PowerPoint for creating presentations. LaTeX provided a highly flexible and professional typesetting environment for producing scientific and academic documents, offering precise control over the structure and formatting of the final document. The combination of these tools facilitated the creation of a well-documented thesis presented effectively.

4.2 Internet Access

For the completion of the master's thesis, access to the Internet was crucial for various tasks. A VPN connection provided by the university was used to securely access internal resources, including remote SSH connection to the cluster where numerical simulations were configured and launched, as well as to the workstation for processing generated data. Additionally, the required literature review to support the thesis was conducted using online resources.

4.3 Previous Knowledge

The student authoring this master's thesis needed a solid foundation of previous knowledge in fluid mechanics, computational numerical simulation of fluids, fluid dynamics, and multiphase flow modeling to theoretically navigate the tasks and study planning conducted. Furthermore, programming skills in both medium and high-level languages were essential to handle the software used and to perform post-processing and results analysis tasks.

4.4 Supervision

The professional guidance of a specialized research professor in numerical simulation of multiphase flows was required to oversee and supervise the tasks and progress made by the student authoring this master's thesis. Additionally, their knowledge and experience were crucial in resolving any doubts arising during the thesis development and in guiding and directing the student's initiatives aimed at improving the thesis.

Part III

Budget

Chapter 1

Introduction

This part of the document describes and details the monetary cost involved in carrying out the study and documentation of this master's thesis (TFM). As it is an engineering investigation using computer simulations, this work required human resources, basic services, real estate resources and computer resources. The monetary unit used to estimate the budget for this work is the Euro (€).

The total budget for this work can be subdivided into different budget items (i.e., partial budgets), which include the costs of the required resources described in the previous paragraph and also an amount to cover unforeseen expenses and an item corresponding to the profit of the industry.

- **Partial Budget for Human Resources**: Includes the cost of work hours for a university student who is the author of the thesis, the cost of work hours for a doctoral student who supervised and collaborated on the work, and the cost of an associate professor who acted as the advisor.
- **Partial Budget for Computational Resources**: Corresponds to the cost of using hardware and software from the CMT institute, as well as those owned by the student, to perform computational simulations, preprocessing, postprocessing, calculations, and documentation. This also includes electricity consumption, as high-performance computing environments have significantly higher electricity consumption compared to traditional office computational equipment.
- **Contingency Budget**: Amount set aside to cover any unforeseen expenses that may arise during the development of the work. It is calculated as 5% of the subtotal of the total resources.
- **Industry Benefit**: Represents the additional project cost in case an industry is interested in investing in it. It is attributed 6% of the total budget before applying VAT.

The prices assigned to the costs in the partial budgets are based on current legal rates, and in necessary cases, consistent estimations thereof are made. It is important to highlight that this Master's Thesis has been limited to a computational study, therefore a partial budget will be presented for the monetary cost of computational resources, along with a total budget for the entire work. Additionally, an extra percentage is added to the total budget to cover unforeseen expenses, and another percentage is included as industry profit. To this subtotal, a 21% VAT is added.

Chapter 2

Partial budget for human resources

In this partial budget, the costs associated with the professional work of the individuals involved in this project are included. These individuals dedicate hours of professional work to the planning, execution, and documentation of the project. The individuals involved are:

1. Master's student: A student from the Master's program in Computational Fluid Mechanics at the Universitat Politècnica de València, who dedicates their working hours to planning and conducting the computational study, as well as its documentation and presentation.
2. Ph.D. student: A doctoral researcher who dedicates part of their working hours to providing guidance and specifying tasks that help achieve the objectives of the computational study, and to resolving procedural doubts.
3. Associate Professor: An associate professor at the university, who holds a Ph.D. in aeronautical engineering, dedicates hours within their contract to supervise this Master's Thesis. This involves guiding the student in their tasks, resolving doubts, guiding proposals, and conducting periodic reviews and corrections of the progress of the work.

These individuals' professional contributions are essential for the successful completion of the project, and their respective roles are crucial in ensuring its academic and technical quality.

2.1 Unitary costs

To calculate the unit cost of the work for each individual involved, first calculate the hourly cost based on their annual gross salary.

1. Cost of work for the master's student: He has worked a total of 1125 hours on the project, at a rate of 37.5 hours per week for 30 weeks. This fulfills the 27 ECTS credits corresponding to the combined credits for company internships and the Master's Thesis. The cost per hour of work is calculated based on the university's annual gross salary set for a master's student on internship (2250€), divided by the total number of hours worked:

$$\text{Cost per work hour student} = \frac{\text{Annual Salary}}{\text{Annual work hours}} = \frac{2250\ €}{1125\ \text{h}} = 2\ €/\text{h}$$

2. Cost of work for the doctoral student: She has used part of her work hours from her researcher contract to guide and supervise the tasks performed by the student authoring

the thesis. The cost per hour of work is calculated based on the annual gross salary for a doctoral research student (17,737€), divided by the total number of work hours in a year:

$$\text{Cost per work hour student} = \frac{\text{Annual Salary}}{\text{Annual work hours}} = \frac{17,737\text{ €}}{60\text{ h}} = 10.28\text{ €/h}$$

3. Cost of work for the tutor professor: The unit cost per hour of the tutor's work is estimated based on his annual gross salary (37,791.04 €), which can be consulted in the table of REMUNERATION OF TEACHING STAFF IN ACCORDANCE WITH THE 2024 BUDGET LAW. The annual number of work hours required by his contract as a tenured professor, considering a total of 37.5 work hours per week for 46 weeks per year is 1725 hours:

$$\text{Cost per work hour tutor} = \frac{\text{Annual Salary}}{\text{Annual work hours}} = \frac{37,791.04\text{ €}}{1725\text{ h}} = 21.90\text{ €/h}$$

To calculate the total cost, multiply the number of hours dedicated to this project by the hourly rate for each individual in their respective roles. This breakdown is shown in Table 2.1, which displays the total cost of the partial budget for human resources.

Staff	Dedication [h]	Hourly rate [*e*/h]	Cost [*e*]
Student Intern	1125	2	2250
PhD student	60	10.28	616.8
University Professor	60	21.90	1314
		TOTAL	**4180.8**

Table 2.1: Cost breakdown by staff and hourly rate

The total cost of the partial budget for human resources is estimated at
FOUR THOUSAND ONE HUNDRED EIGHTY EUROS AND EIGHTY CENTS.

Chapter 3

Partial budget for computational resources

This chapter breaks down the unit cost of each of the required computing resources for the development of this work, which include: the cost of using necessary computers, the cost of simulations on the CMT cluster, licenses for commercial software used, and the unit cost of each hour of electrical consumption by the equipment used.

3.1 Costs related to personal computers

The computational equipment involved includes a personal laptop and an office workstation. To calculate the cost of their use and availability per hour, first calculate the annual depreciation cost of each equipment using the equation:

$$A = \frac{V_C - V_R}{n} \tag{3.1}$$

Where:

- A is the annual depreciation value of the equipment.
- V_C is the purchase value of the equipment. For the specific laptop, it is 1000 euros, and for the workstation, 5000 euros.
- V_R is the residual value of the equipment. For both the laptop and the workstation, it is estimated at 20% of the purchase value.
- n is the depreciation period. For the specific laptop, it is estimated at 5 years, and for the workstation, 4 years.

The value of A, given by the equation 3.1, is calculated for each computer and recorded in the table 3.1. If a year is considered to have 1750 working hours, then the cost of using and availability of the computers per hour of use can be estimated. In the table 3.1, the unit cost of using and availability of each computer is estimated based on the number of working hours performed on it.

Computer Equipment	A [€/year]	Hourly rate [€/h]	Working hours [h]	Cost [€]
Personal Laptop	272	0.16	450	70.96
Workstation	1000	0.58	350	260.87

Table 3.1: Cost breakdown by computer equipment and hourly rate

3.2 Electricity costs

The electricity consumption of the computer equipment used is calculated based on the total number of hours spent using it and an estimated energy consumption value of 0.09 kW.

$$\text{Power consumption} = \text{Consumption rate} * \text{Hours of use} = 0.09\text{ kW * }800\text{ h} = 72\text{ kWh}$$

So, the total cost taking into account that the cost of electricity service in Spain as of May 20, 2024 is 0.28, €/kWh is:

$$\text{Power consumption cost} = \text{Consumption} * \text{Cost per hour} = 72\text{ kWh * }0.28\text{ €/kWh} = 20.16\text{ €}$$

3.3 Costs related to running simulations in HPC environments

Using the CMT cluster involves a significant financial expense. As it is a high-performance device that has significant energy consumption, as well as requiring maintenance, updating and continuous cooling services, each hour of calculation on one of its processors has a monetary cost. Taking into account the capacities and expenses of the cluster, it is estimated that one hour of calculation on a processor is 0.01, €/h.

The simulations for this study involved a total of 1,454,100 computing hours, therefore the cost of the simulations is:

$$\text{Simulations cost} = \text{Total calcultaion hours} * \text{Cost per hour} = 1.45\text{e}6\text{ h * }0.01\text{ €/h} = 14,541\text{ €}$$

3.4 Costs related to software licenses

The only commercial software license required for this study was the Microsoft Office software package with cloud storage services provided by the University. This license costs 69 € per year. Considering that the project was planned within half a course, then the cost is 34.5 €.

3.5 Total Costs

After breaking down the cost of the equipment, simulations, power consumption and licenses, the total cost of the computer equipment used in this work is presented in Table 3.2.

Concept	Cost [€]
Personal Laptop	70.96
Workstation	260.87
Cost	14,541.0
Electricity Cost	20.16
Microsoft Office 365 License	34.50
TOTAL	**14 927.49**

Table 3.2: Detailed breakdown of the total cost of computer equipment

The total cost of the partial budget for the computing resources is estimated at **FOURTEEN THOUSAND NINE HUNDRED TWENTY-SEVEN EUROS AND FORTY NINE CENTS**

Chapter 4

Total Budget

When grouping and summing each of the partial budgets described in the previous sections—human resources costs, computing resources costs, contingencies, and industry benefits—the subtotal of the total budget for this master's thesis project is obtained. The total is calculated by adding the corresponding Value Added Tax (VAT) rate of 21%. The detailed breakdown of this total budget is shown in the table. 4.1.

Concept	Cost [€]
Costs related to human resources	4180.80
Costs related to computational resources	14,927.49
Resources subtotal	19,108.29
Contingency budget (5%)	955.41
Project subtotal	20,063.70
Industrial profit (6%)	1,203.82
Subtotal	21,267.52
IVA (21%)	4466.18
TOTAL	**25 733.70**

Table 4.1: Detailed breakdown of total costs

The total cost of the budget for this present work is estimated at **TWENTY-FIVE THOUSAND SEVEN HUNDRED THIRTY THREE AND SEVENTY CENTS**.